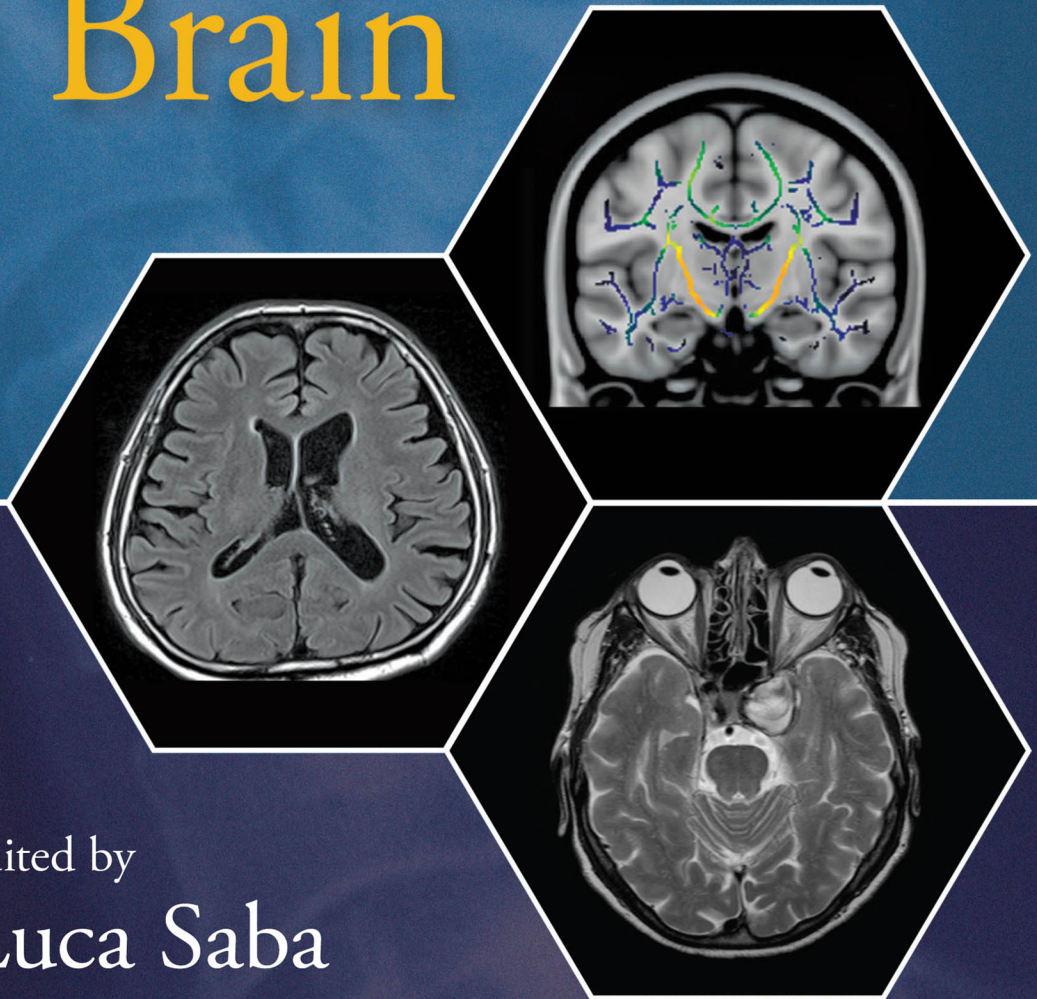


MAGNETIC RESONANCE IMAGING HANDBOOK

Image Principles, Neck, and the Brain



edited by
Luca Saba

MAGNETIC RESONANCE IMAGING HANDBOOK

Image Principles, Neck, and the Brain

Magnetic Resonance Imaging Handbook

Image Principles, Neck, and the Brain

Imaging of the Cardiovascular System, Thorax, and Abdomen

Imaging of the Pelvis, Musculoskeletal System, and Special Applications to CAD

MAGNETIC RESONANCE IMAGING HANDBOOK

Image Principles, Neck, and the Brain

edited by
Luca Saba



CRC Press

Taylor & Francis Group

Boca Raton London New York

CRC Press is an imprint of the
Taylor & Francis Group, an **informa** business

CRC Press
Taylor & Francis Group
6000 Broken Sound Parkway NW, Suite 300
Boca Raton, FL 33487-2742

© 2016 by Taylor & Francis Group, LLC
CRC Press is an imprint of Taylor & Francis Group, an Informa business

No claim to original U.S. Government works
Version Date: 20151119

International Standard Book Number-13: 978-1-4822-1620-2 (eBook - PDF)

This book contains information obtained from authentic and highly regarded sources. Reasonable efforts have been made to publish reliable data and information, but the author and publisher cannot assume responsibility for the validity of all materials or the consequences of their use. The authors and publishers have attempted to trace the copyright holders of all material reproduced in this publication and apologize to copyright holders if permission to publish in this form has not been obtained. If any copyright material has not been acknowledged please write and let us know so we may rectify in any future reprint.

Except as permitted under U.S. Copyright Law, no part of this book may be reprinted, reproduced, transmitted, or utilized in any form by any electronic, mechanical, or other means, now known or hereafter invented, including photocopying, microfilming, and recording, or in any information storage or retrieval system, without written permission from the publishers.

For permission to photocopy or use material electronically from this work, please access www.copyright.com (<http://www.copyright.com/>) or contact the Copyright Clearance Center, Inc. (CCC), 222 Rosewood Drive, Danvers, MA 01923, 978-750-8400. CCC is a not-for-profit organization that provides licenses and registration for a variety of users. For organizations that have been granted a photocopy license by the CCC, a separate system of payment has been arranged.

Trademark Notice: Product or corporate names may be trademarks or registered trademarks, and are used only for identification and explanation without intent to infringe.

Visit the Taylor & Francis Web site at
<http://www.taylorandfrancis.com>

and the CRC Press Web site at
<http://www.crcpress.com>

This book is dedicated to Giovanni Saba.

Thank you.

This page intentionally left blank

Start by doing what's necessary; then do what's possible; and suddenly you are doing the impossible.

Francis of Assisi (1181–1226)

The whole is more than the sum of its parts.

Aristotle, Greek philosopher (ca. 384–322 BC)

This page intentionally left blank

Contents

Preface.....	xi
Acknowledgments	xiii
Editor.....	xv
Contributors.....	xvii
1. History and Physical Principles of Magnetic Resonance Imaging	1
<i>Michael E. Hayden and Pierre-Jean Nacher</i>	
2. Introduction to the Basics of MRI to Introduce the Macroscopic Magnetization M.....	29
<i>Luigi Barberini</i>	
3. Contrast Agents for Magnetic Resonance Imaging.....	61
<i>Henrik S. Thomsen</i>	
4. Diffusion Imaging: Basic Principles	73
<i>Ioannis Tsougos</i>	
5. Arterial Spin-Labeled Perfusion Imaging	101
<i>Hongjian He and Jianhui Zhong</i>	
6. Kinetic Modeling for T_1-Weighted Dynamic Contrast-Enhanced Magnetic Resonance Imaging.....	119
<i>Kyunghyun Sung and John Carr</i>	
7. BOLD Functional Magnetic Resonance Imaging	135
<i>Chris J. Conklin, Devon M. Middleton, Scott H. Faro, and Feroze B. Mohamed</i>	
8. Magnetic Resonance Enterography and Colonography: Technical Considerations.....	153
<i>Jesica Makanyanga, Douglas Pendse, Rehana Hafeez, and Stuart A. Taylor</i>	
9. Artifacts in Magnetic Resonance Imaging	165
<i>Michael N. Hoff, Jalal B. Andre, and Brent K. Stewart</i>	
10. Risk of Magnetic Resonance: The Safety-Biological Effects.....	191
<i>Valentina Hartwig</i>	
11. 7 T Magnetic Resonance Imaging and Spectroscopy: Methods and Applications.....	213
<i>Simon Robinson, Roland Beisteiner, Wolfgang Bogner, Klaus Bohndorf, Marek Chmelík, Barbara Dymerska, Florian Fischmeister, Stephan Gruber, Gilbert Hangel, Vladimir Juras, Claudia Kronnerwetter, Eva Matt, Günther Grabner, Martin Krššák, Lenka Minarikova, Benjamin Schmitt, Bernhard Strasser, Štefan Zbýň, and Siegfried Trattng</i>	
12. Pathology of the Paranasal Sinuses (Infective–Neoplastic)	259
<i>Ellen Hoeffner</i>	
13. Magnetic Resonance Imaging of the Ear.....	287
<i>Ravi Kumar Lingam and Ram Vaidhyanath</i>	
14. Differential Diagnosis in Magnetic Resonance Imaging of the Ear	325
<i>Gabriele A. Krombach</i>	

15. Magnetic Resonance Imaging of the Salivary Gland	355
<i>Takashi Nakamura and Misa Sumi</i>	
16. Infective Pathology of the Neck	399
<i>Naoko Saito, Joan Cheng, Akifumi Fujita, Hiroyuki Fujii, and Osamu Sakai</i>	
17. Neoplastic Pathology of the Neck	425
<i>Ahmed Abdel Khalek Abdel Razek</i>	
18. Lymph Nodes of the Neck	453
<i>Fatih Alper, Irmak Durur-Subasi, and Adem Karaman</i>	
19. Magnetic Resonance Imaging of the Eye and Orbit	483
<i>Pradipta C. Hande</i>	
20. Brain Aging and Degenerative Diseases of the Brain	527
<i>Memi Watanabe, Joshua Thatcher, Yukio Kimura, Ivana Delalle, Samuel Frank, and Osamu Sakai</i>	
21. Congenital Brain Malformations	553
<i>Elzbieta Jurkiewicz and Katarzyna Nowak</i>	
22. Infectious Diseases of the Brain	611
<i>John H. Rees and James G. Smirniotopoulos</i>	
23. Ischemic and Hemorrhagic Stroke	661
<i>Shahmir Kamalian, Supada Prakkamakul, and Albert J. Yoo</i>	
24. Vascular Pathologies of the Brain (Vasculitis–Arteriovenous Malformation/Arteriovenous Fistula–Aneurysm)	691
<i>Karl-Olof Lövblad, Sven Haller, Vitor Mendes Pereira, and Maria Isabel Vargas</i>	
25. Neoplasms of the Brain and Pituitary Gland	713
<i>Sara E. Kingston, Daniel S. Treister, Willa Jin, Megha Nayyar, Benita Tamrazi, Francesco D'Amore, Bavrina Bigjahan, Alexander Lerner, Bruno A. Telles, Chia-Shang J. Liu, and Mark S. Shiroishi</i>	
26. Demyelinating and Metabolic Diseases of the Brain	745
<i>Antonia Ceccarelli, Eytan Raz, and Matilde Inglese</i>	
27. Traumatic Disease of the Brain and Skull	799
<i>Eytan Raz</i>	
Index	811

Preface

Magnetic resonance imaging (MRI) is a medical imaging technique used in radiology to visualize internal structures of the body in detail. The introduction of MRI resulted in a fundamental and far-reaching improvement of the diagnostic process because this technique provides an excellent contrast between the different soft tissues of the body, which makes it especially useful in imaging the brain, muscles, heart, and cancers compared with other medical imaging techniques such as computed tomography or X-rays.

In the past 20 years, MRI technology has further improved with the introduction of systems up to 7 T and with the development of numerous postprocessing algorithms such as diffusion tensor imaging (DTI), functional MRI (fMRI), and spectroscopic imaging.

From these developments, the diagnostic potentialities of MRI have impressively improved with exceptional spatial resolution and the possibility of analyzing the morphology and function of several kinds of pathology.

The purpose of this book is to cover engineering and clinical benefits in the diagnosis of human pathologies using MRI. It will cover the protocols and potentialities of advanced MRI scanners with very high-quality MR images. Given these exciting developments in the MRI field, I hope that this book will be a timely and complete addition to the growing body of literature on this topic.

Luca Saba

University of Cagliari, Italy

This page intentionally left blank

Acknowledgments

It is not possible to overstate my gratitude to the many individuals who helped to produce this book; their enthusiasm and dedication were unbelievable.

I express my appreciation to CRC Press/Taylor & Francis Group for their professionalism in handling this

project. Your help was wonderful and made producing this book an enjoyable and worthwhile experience.

Finally, I acknowledge Tiziana.

This page intentionally left blank

Editor

Professor Luca Saba earned his MD from the University of Cagliari, Italy, in 2002. Currently, he works at the Azienda Ospedaliero Universitaria of Cagliari. His research is focused on multidetector-row computed tomography, magnetic resonance, ultrasound, neuroradiology, and diagnostics in vascular sciences.

Professor Saba has published more than 180 papers in high-impact factor journals such as the *American Journal of Neuroradiology*, *Atherosclerosis*, *European Radiology*, *European Journal of Radiology*, *Acta Radiologica*, *Cardiovascular and Interventional Radiology*, *Journal of Computer Assisted Tomography*, *American Journal of Roentgenology*, *Neuroradiology*, *Clinical Radiology*, *Journal of Cardiovascular Surgery*, *Cerebrovascular Diseases*, *Brain Pathology*, *Medical Physics*, and *Atherosclerosis*. He is a

well-known speaker and has spoken over 45 times at national and international conferences.

Dr. Saba has won 15 scientific and extracurricular awards during his career, and has presented more than 500 papers and posters at national and international congress events (Radiological Society of North America [RSNA], ESGAR, ECR, ISR, AOCR, AINR, JRS, Italian Society of Radiology [SIRM], and AINR). He has written 21 book chapters and is the editor of 10 books in the fields of computed tomography, cardiovascular surgery, plastic surgery, gynecological imaging, and neurodegenerative imaging.

He is a member of the SIRM, European Society of Radiology, RSNA, American Roentgen Ray Society, and European Society of Neuroradiology, and serves as the reviewer of more than 40 scientific journals.

This page intentionally left blank

Contributors

Fatih Alper

Department of Radiology
Ataturk University
Erzurum, Turkey

Jalal B. Andre

Harborview Medical Center
University of Washington School
of Medicine
Seattle, Washington

Luigi Barberini

Department of Public Health
Clinical and Molecular Medicine
University of Cagliari
Cagliari, Italy
and

Department of Radiology
Cittadella Universitaria di
Monserrato
Monserrato, Italy

Roland Beisteiner

Department of Biomedical Imaging
and Image-Guided Therapy
High Field MR Centre
and
Department of Neurology
Study Group Clinical fMRI
Medical University of Vienna
Vienna, Austria

Bavrina Bigjahan

Division of Neuroradiology
Department of Radiology
Keck School of Medicine
University of Southern California
Los Angeles, California

Wolfgang Bogner

Department of Biomedical Imaging
and Image-Guided Therapy
High Field MR Centre
Medical University of Vienna
Vienna, Austria

Klaus Bohndorf

Department of Biomedical Imaging
and Image-Guided Therapy
High Field MR Centre
Medical University of Vienna
Vienna, Austria

John Carr

Department of Radiological
Sciences
University of California
Los Angeles, California

Antonia Ceccarelli

Department of Neurology
Icahn School of Medicine at
Mount Sinai
New York, New York

Joan Cheng

Department of Radiology
Boston Medical Center
Boston University School of
Medicine
Boston, Massachusetts

Marek Chmelík

Department of Biomedical Imaging
and Image-Guided Therapy
High Field MR Centre
Medical University of Vienna
Vienna, Austria

Chris J. Conklin

Magnetic Resonance Imaging
Physics Lab
Thomas Jefferson University
Philadelphia, Pennsylvania

Francesco D'Amore

Division of Neuroradiology
Department of Radiology
Keck School of Medicine
University of Southern California
Los Angeles, California

Ivana Delalle

Department of Pathology and
Laboratory Medicine
Boston Medical Center
Boston University School of
Medicine
Boston, Massachusetts

Irmak Durur-Subasi

Department of Radiology
Ataturk University
Erzurum, Turkey

Barbara Dymerska

Department of Biomedical Imaging
and Image-Guided Therapy
High Field MR Centre
Medical University of Vienna
Vienna, Austria

Scott H. Faro

Departments of Radiology,
Computer Engineering, and
Bioengineering
Temple University
Philadelphia, Pennsylvania

Florian Fischmeister

Department of Biomedical Imaging
and Image-Guided Therapy
High Field MR Centre
and
Department of Neurology
Study Group Clinical fMRI
Medical University of Vienna
Vienna, Austria

Samuel Frank

Department of Neurology
Boston Medical Center
Boston University School of
Medicine
Boston, Massachusetts

Hiroyuki Fujii

Department of Radiology
Jichi Medical University
Tochigi, Japan

Akifumi Fujita

Department of Radiology
Boston Medical Center
Boston University School of
Medicine
Boston, Massachusetts

and

Department of Radiology
Jichi Medical University School
of Medicine
Shimotsuke, Japan

Günther Grabner

Department of Biomedical Imaging
and Image-Guided Therapy
High Field MR Centre
Medical University of Vienna
Vienna, Austria

Stephan Gruber

Department of Biomedical Imaging
and Image-Guided Therapy
High Field MR Centre
Medical University of Vienna
Vienna, Austria

Rehana Hafeez

Department of Surgery
Princess Royal University Hospital
Kent, United Kingdom

Sven Haller

Division of Interventional and
Diagnostic Neuroradiology
Geneva University Hospitals
Geneva, Switzerland

Pradipta C. Hande

Department of Imaging
Breach Candy Hospital Trust
Mumbai, India

Gilbert Hangel

Department of Biomedical Imaging
and Image-Guided Therapy
High Field MR Centre
Medical University of Vienna
Vienna, Austria

Valentina Hartwig

Italian National Research Council
(CNR)
Institute of Clinical Physiology
(IFC)
San Cataldo (Pisa), Italy

Michael E. Hayden

Physics Department
Simon Fraser University
Burnaby, British Columbia, Canada

Hongjian He

Center for Brain Imaging Science
and Technology
Zhejiang University
Hangzhou, China

Ellen Hoeffner

Department of Radiology
University of Michigan Medical
School
Ann Arbor, Michigan

Michael N. Hoff

Department of Radiology
University of Washington School
of Medicine
Seattle, Washington

Matilde Inglese

Department of Neurology,
Radiology and Neuroscience
Neurology Imaging Laboratory
Icahn School of Medicine at Mount
Sinai
New York, New York

Willa Jin

Division of Neuroradiology
Department of Radiology
Keck School of Medicine
University of Southern California
Los Angeles, California

Vladimir Juras

Department of Biomedical Imaging
and Image-Guided Therapy
High Field MR Centre
Medical University of Vienna
Vienna, Austria

Elzbieta Jurkiewicz

Department of Diagnostic Imaging
The Children's Memorial Health
Institute
Warsaw, Poland

Shahmir Kamalian

Division of Neuroradiology
Department of Radiology
University of Massachusetts School
of Medicine
Worcester, Massachusetts

Adem Karaman

Department of Radiology
Ataturk University
Erzurum, Turkey

Yukio Kimura

Department of Radiology
Jichi Medical University
Tochigi, Japan

Sara E. Kingston

Division of Neuroradiology
Department of Radiology
Keck School of Medicine
University of Southern California
Los Angeles, California

Gabriele A. Krombach

Department of Diagnostic and
Interventional Radiology
University Hospital Giessen
Justus Liebig University Giessen
Giessen, Germany

Claudia Kronnerwetter

Department of Biomedical Imaging
and Image-Guided Therapy
High Field MR Centre
Medical University of Vienna
Vienna, Austria

Martin Krššák

Department of Biomedical Imaging
and Image-Guided Therapy
High Field MR Centre
Medical University of Vienna
Vienna, Austria

Alexander Lerner

Division of Neuroradiology
Department of Radiology
Keck School of Medicine
University of Southern California
Los Angeles, California

Ravi Kumar Lingam

Department of Radiology
Northwick Park and Central
Middlesex Hospitals
London North West Hospitals NHS
Trust
London, United Kingdom

Chia-Shang J. Liu

Division of Neuroradiology
Department of Radiology
Keck School of Medicine
University of Southern California
Los Angeles, California

Karl-Olof Lövblad

Division of Interventional and
Diagnostic Neuroradiology
Geneva University Hospitals
Geneva, Switzerland

Jesica Makanyanga

Centre for Medical Imaging
University College London
London, United Kingdom

Eva Matt

Department of Biomedical Imaging
and Image-Guided Therapy
High Field MR Centre
and
Department of Neurology
Study Group Clinical fMRI
Medical University of Vienna
Vienna, Austria

Devon M. Middleton

Department of Radiology
and
Department of Bioengineering
Temple University
Philadelphia, Pennsylvania

Lenka Minarikova

Department of Biomedical Imaging
and Image-Guided Therapy
High Field MR Centre
Medical University of Vienna
Vienna, Austria

Feroze B. Mohamed

Magnetic Resonance Imaging
Physics Lab
Thomas Jefferson University
Philadelphia, Pennsylvania

Pierre-Jean Nacher

Laboratoire Kastler Brossel
ENS-PSL Research University
CNRS, UPMC-Sorbonne
Universités
Collège de France
Paris, France

Takashi Nakamura

Department of Radiology and
Cancer Biology
Nagasaki University School of
Dentistry
Nagasaki, Japan

Megha Nayyar

Division of Neuroradiology
Department of Radiology
Keck School of Medicine
University of Southern California
Los Angeles, California

Katarzyna Nowak

Department of Diagnostic Imaging
The Children's Memorial Health
Institute
Warsaw, Poland

Douglas Pendse

Centre for Medical Imaging
University College London
London, United Kingdom

Vitor Mendes Pereira

Division of Interventional and
Diagnostic Neuroradiology
Geneva University Hospitals
Geneva, Switzerland

Supada Prakkamakul

Department of Radiology
King Chulalongkorn Memorial
Hospital
The Thai Red Cross Society
Bangkok, Thailand

Eytan Raz

Department of Radiology
NYU Langone Medical Center
New York, New York

Ahmed Abdel Khalek Abdel Razek

Department of Diagnostic
Radiology
Mansoura University
Mansoura, Egypt

John H. Rees

Department of Radiology
Partners Imaging Center
Sarasota, Florida
and

Department of Radiology
Georgetown University
Washington, DC

Simon Robinson

Department of Biomedical Imaging
and Image-Guided Therapy
High Field MR Centre
Medical University of Vienna
Vienna, Austria

Naoko Saito

Department of Radiology
Saitama International Medical
Center
Saitama Medical University
Saitama, Japan

Osamu Sakai

Departments of Radiology,
Otolaryngology, Head and Neck
Surgery, and Radiation Oncology
Boston Medical Center
Boston University School of
Medicine
Boston, Massachusetts

Benjamin Schmitt

Healthcare Sector
Siemens Australia
New South Wales, Australia

Mark S. Shiroishi

Division of Neuroradiology
Department of Radiology
Keck School of Medicine
University of Southern California
Los Angeles, California

James G. Smirniotopoulos

MedPix®
National Library of Medicine
National Institutes of Health
Bethesda, Maryland

Brent K. Stewart

Department of Radiology
University of Washington School
of Medicine
Seattle, Washington

Bernhard Strasser

Department of Biomedical Imaging
and Image-Guided Therapy
High Field MR Centre
Medical University of Vienna
Vienna, Austria

Misa Sumi

Department of Radiology
and Cancer Biology
Nagasaki University School
of Dentistry
Nagasaki, Japan

Kyunghyun Sung

Department of Radiological
Sciences
University of California
Los Angeles, California

Benita Tamrazi

Division of Neuroradiology
Department of Radiology
Keck School of Medicine
University of Southern California
Los Angeles, California

Stuart A. Taylor

Centre for Medical Imaging
University College London
London, United Kingdom

Bruno A. Telles

Division of Neuroradiology
Department of Radiology
Keck School of Medicine
University of Southern California
Los Angeles, California

Joshua Thatcher

Department of Radiology
Boston Medical Center
Boston University School of
Medicine
Boston, Massachusetts

Henrik S. Thomsen

Department of Diagnostic
Radiology
Copenhagen University Hospital
Herlev
Herlev, Denmark

Siegfried Trattig

Department of Biomedical Imaging
and Image-Guided Therapy
High Field MR Centre
Medical University of Vienna
Vienna, Austria

Daniel S. Treister

Division of Neuroradiology
Department of Radiology
Keck School of Medicine
University of Southern California
Los Angeles, California

Ioannis Tsougos

Department of Medicine
University of Thessaly
Larissa, Greece

Ram Vaidhyanath

Department of Radiology
University of Leicester
Leicester, United Kingdom

Maria Isabel Vargas

Division of Interventional and
Diagnostic Neuroradiology
Geneva University Hospitals
Geneva, Switzerland

Memi Watanabe

Department of Radiology
Boston Medical Center
Boston University School of
Medicine
Boston, Massachusetts

Albert J. Yoo

Division of Neurointervention
Texas Stroke Institute
Plano, Texas

Štefan Zbýň

Department of Biomedical Imaging
and Image-Guided Therapy
High Field MR Centre
Medical University of Vienna
Vienna, Austria

Jianhui Zhong

Center for Brain Imaging Science
and Technology
Zhejiang University
Hangzhou, China

and

Department of Imaging Sciences
University of Rochester
Rochester, New York

1

History and Physical Principles of Magnetic Resonance Imaging

Michael E. Hayden and Pierre-Jean Nacher

CONTENTS

1.1	History.....	2
1.2	Fundamentals of NMR	5
1.2.1	Bloch Equations and NMR Dynamics.....	5
1.2.1.1	Spin: A Quantum Property	5
1.2.1.2	Classical Magnetization Dynamics.....	7
1.2.1.3	Irreversibility: The Bloch Equations.....	10
1.2.2	Electrodynamics of NMR.....	12
1.2.2.1	Ampère’s Law: Currents, Coils, and Fields	12
1.2.2.2	Faraday’s Law: NMR Detection	16
1.2.2.3	Signal Amplitude Considerations	16
1.2.2.4	Health Safety Considerations.....	17
1.3	Fundamentals of MRI	18
1.3.1	Effect of a Field Gradient: 1D Imaging	18
1.3.2	2D and 3D Imaging Methods.....	21
1.3.3	Contrast	24
	References.....	25

Magnetic resonance imaging (MRI) was broadly introduced to the scientific community in 1973, when Paul C. Lauterbur published images representing the nuclear magnetic resonance (NMR) response of hydrogen nuclei in a pair of water-filled glass capillaries [1]. One-dimensional (1D) projections of this response were first obtained through a procedure that involved applying static magnetic field gradients to the sample, mapping NMR frequency onto the source position. A series of 1D projections, acquired along different gradient directions, were then combined to reconstruct a two-dimensional (2D) image, as illustrated in Figure 1.1.

A NEW WORD FOR A NEW WAY OF SEEING

Lauterbur coined the term *zeugmatogram* to describe his NMR images. This word is derived from the Greek ζευγμα (“zeugma”), meaning “that which is used for joining,” in reference to the manner in which static magnetic field gradients were employed to localize the sample response to oscillating magnetic fields. Similar 1D NMR imaging methods had already been demonstrated as early as 1952 [2] and were employed in the 1956 discovery of phase

separation in liquid ^3He – ^4He mixtures at low temperatures [3]. However, it was Lauterbur who extended the method to two dimensions and recognized its potential for soft tissue imaging. Perhaps the most well-known 1D NMR images predating Lauterbur’s 1973 paper were published just one year earlier, in connection with a Cornell University study of another low-temperature-phase transition, this time in pure liquid ^3He [4]. Three of the four authors of that report were awarded the 1996 Nobel Prize in Physics for the discovery of superfluidity in ^3He .

The term *Zeugmatography* remains obscure, but *MRI*—the field that emerged—is anything but.

Lauterbur’s simple but insightful demonstration launched a flurry of scientific, industrial, and clinical activity that has since profoundly influenced the practice and delivery of medicine in industrialized countries. Sophisticated extensions of his work are now fueling revolutions in neuroscience and our understanding of cognition.

This chapter starts by tracing the history of MRI from its roots in the field of NMR through to the present.

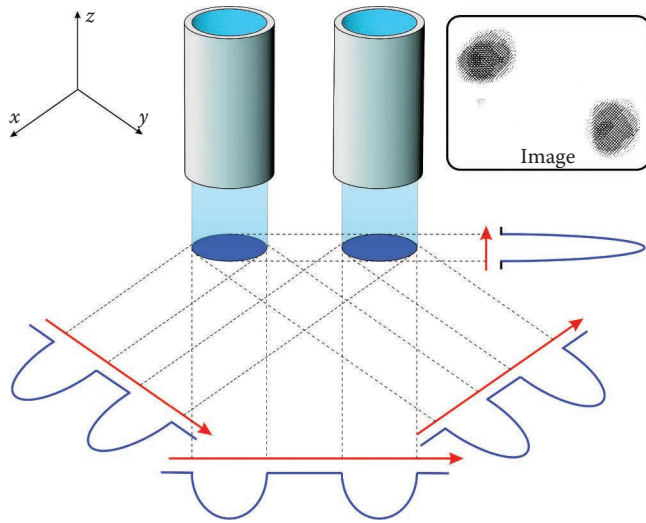


FIGURE 1.1

Principle underlying the first MRI experiment, performed by P.C. Lauterbur [1]. Two objects (water-filled capillaries) aligned with the z -axis are shown, along with their projection onto the x - y plane. Magnetic field gradients applied along various directions cause the NMR response to spread out in frequency, producing 1D projections reflecting the distribution of water (blue curves). Multiple projections, acquired along different gradient directions (indicated by red arrows), are then combined to reconstruct a 2D image. Inset: Lauterbur's NMR image of two 1 mm inner-diameter water-filled capillaries. (Data from Lauterbur, P., *Nature*, 242, 190–191, 1973, reprinted with permission from Nature Publishing Group.)

It is a story that is much richer and nuanced than can be adequately described in a few pages; our narrative certainly ignores many critical contributions to the field. The basic physical principles of NMR are then introduced; these form the basis for understanding the “NMR response” referred to above. Again, the treatment presented here is necessarily brief. The interested reader is encouraged to consult some of the excellent and extensive monographs that have been written on this topic [5–10]. Finally, the basic principles underlying magnetic resonance (MR) image generation itself are introduced; many of these topics are covered in greater detail in subsequent chapters, but again the interested reader will find valuable additional information about the underlying physics in more specialized references [11–15].

1.1 History

The foundations of NMR—and hence MRI—were laid during the 1940s, in experiments designed to directly detect the precession of nuclear magnetic moments in a magnetic field [16–18]. Those experiments, which

involved hydrogen atoms in liquids and solids, built on work carried out during the 1930s at Columbia University. There, a team led by Isidore I. Rabi showed that an oscillating magnetic field could be used to induce transitions between nuclear spin states of lithium and chlorine atoms in a molecular beam [19]. Rabi's pioneering experiments in turn employed spin-state selection and detection techniques similar to those developed in Frankfurt during the 1920s by Otto Stern and Walther Gerlach, in connection with their seminal discovery of spin quantization using a beam of silver atoms [20].

The extension of Rabi's 1938 observation of NMR in a beam of independent molecules to solid and liquid samples was successfully, independently, and essentially simultaneously accomplished in 1945 by Edward M. Purcell and Felix Bloch. A key feature of these experiments was the fact that both employed direct electromagnetic detection techniques to resolve the resonances. At the Massachusetts Institute of Technology (MIT) Radiation Laboratory, Purcell, Torrey, and Pound worked with 1 L of solid paraffin in a cavity tuned to resonate at 30 MHz. They observed a 0.4% change in radiofrequency (RF) signal amplitude across the cavity as the static magnetic field was swept through “an extremely sharp resonance”; this reduction in quality factor was attributed to energy dissipation associated with nuclear spin relaxation of H atoms [16]. Meanwhile at Stanford University, Bloch, Hansen, and Packard performed similar experiments on a 1.5 cm³ sample of water at 7.7 MHz. They used two orthogonal RF coils; the receive coil detected RF power when the nuclei of the water protons (H atoms) were resonantly excited by the transmit coil [18]. Although Rabi's work was crucial as the initial demonstration of NMR (he was awarded the Nobel Prize in Physics in 1944 “for his resonance method for recording the magnetic properties of atomic nuclei”), the conceptual and technical leap achieved by Bloch and Purcell really set the stage for the development of modern NMR and MRI.

EARLY ATTEMPTS AND FIRST SUCCESSES

The first reported attempt to observe nuclear spin transitions in solids was published in 1936 by Cornelius J. Gorter [21], who was based in Leiden. That experiment failed, as did a later attempt described in a 1942 paper [22]. Gorter's second paper contains the first published reference to *nuclear magnetic resonance*, a term that he attributed to Rabi. Meanwhile in Kazan, Yevgeny Zavoisky also failed to reliably detect NMR transitions in solids and liquids, but went on to discover electron spin resonance (ESR) in 1944.



I.I. Rabi

C.J. Gorter

Y.K. Zavoisky

Reprinted with permission from (l-r): The Nobel Foundation; Eddy de Jongh; World Scientific.

The first truly successful NMR experiments on solids and liquids were reported in early 1946 [16,17], by two independent teams. One of these teams was led by Felix Bloch at Stanford University. Bloch obtained a PhD from the University of Leipzig in 1928. He left Germany in 1933 and moved to Stanford University, where he spent most of his career. During the latter part of World War II, he spent time at the Harvard Radio Research Laboratory, where he worked on counter-radar measures and became acquainted with modern developments in electronics. The other team was led by Edward M. Purcell at the MIT. Purcell obtained a PhD from Harvard in 1938. He spent the war years at the MIT Radiation Laboratory, where he was influenced by Rabi and contributed to the development of radar and various microwave techniques. He returned to Harvard in 1945 and spent the rest of his career there. Bloch and Purcell were awarded the 1952 Nobel Prize in Physics “for their development of new methods for nuclear magnetic precision measurements and discoveries in connection therewith.”



F. Bloch

E.M. Purcell

Reprinted with permission from The Nobel Foundation.

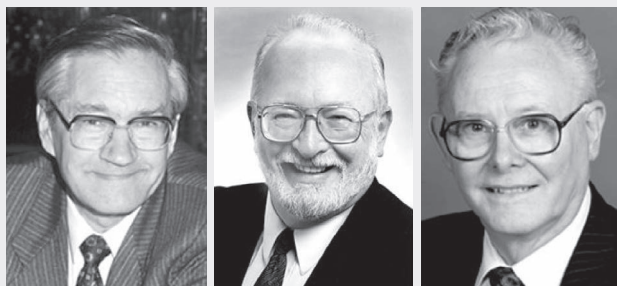
A final critical component of the modern NMR toolbox was contributed independently by Henry C. Torrey [23] and Erwin L. Hahn [24], who demonstrated the feasibility of pulsed NMR (an idea originally suggested by Bloch [25]) and observed free Larmor precession. Hahn further used pulsed NMR to generate and observe spin echoes [26].

The next 20 years saw the development of NMR as a powerful investigative tool in many areas of physics and even more so in chemistry. The sensitivity of the nucleus to its electronic environment in a molecule (the “chemical shift”) and to spin–spin interactions were originally viewed by those in the nuclear physics community as annoying features of the technique. However, the enormous potential of NMR spectroscopy for analytical studies was soon revealed through the discovery of the three peaks of ethanol in Purcell’s group [27]. Almost none of the early applications of NMR were medical, although a great deal of work was published on relaxation, diffusion, and exchange of water in cells and tissues, even in living human subjects [28] and whole animals [29].

As recounted above, MRI came into being in 1973 with Lauterbur’s publication of true 2D NMR images (Figure 1.1), reconstructed from 1D projections acquired while magnetic field gradients were applied in various directions [1]. Soon thereafter, and quite independently, Peter Mansfield at the University of Nottingham introduced critical methods for efficient image generation, including slice selection [30] and fast “snapshot” acquisition schemes wherein entire 2D images could be obtained in a few tens of milliseconds [31].

RECOGNITION FOR KEY CONTRIBUTIONS

Richard R. Ernst developed Fourier transform methods that paved the way for modern MRI. He was awarded the 1991 Nobel Prize in Chemistry for “contributions to the development of the methodology of high-resolution nuclear magnetic resonance (NMR) spectroscopy.” Paul C. Lauterbur and Sir Peter Mansfield were then jointly awarded the 2003 Nobel Prize in Physiology or Medicine “for their discoveries concerning magnetic resonance imaging.”



R.R. Ernst

P.C. Lauterbur

P. Mansfield

Reprinted with permission from The Nobel Foundation.

Another early and essential contribution to MRI was made by Richard Ernst at the Swiss Federal Institute of Technology in Zurich. During the 1960s, he had introduced Fourier transform NMR spectroscopy [32]. In 1975, he realized that one should be able to generate 2D

or three-dimensional (3D) NMR images by applying switched magnetic field gradients as NMR signals were acquired, and then employing the Fourier transform methods that are now a mainstay of modern MR image reconstruction [33].

During the 1970s, research in MRI was largely restricted to academic laboratories, most of them in the United Kingdom. This time period was marked by a series of important demonstrations: crude first *in vivo* images of a human finger (1975), hand (1976), thorax (1977), and head (1978). In 1980, William Edelstein, a postdoctoral fellow in John Mallard's group at the University of Aberdeen, implemented spin-warp (or Fourier) imaging and obtained the first clinically useful image of a human subject [34]. By this time, intense commercial investment in MRI had begun and clinical trials were being promoted. In 1983, Toshiba and Siemens brought the first commercial MRI scanners to market, equipped with 0.15 T (resistive) and 0.35 T (superconducting) magnets, respectively. Meanwhile, General Electric, one of the current leading manufacturers, recruited several of the pioneers in the field, including Edelstein. In 1985, it began to sell the first 1.5 T whole-body clinical MRI system.

Over the past three decades, MRI exams have become routine diagnostic procedures. In 2013, estimates place the number of operational scanners worldwide at more than 30 thousand and the number of exams performed every year at more than 100 million (Figure 1.2a) [35,36]. The ever-growing availability and performance of these systems has facilitated a remarkable and sustained growth in applications, as evidenced by measures such as the number of publications that make reference to MRI (Figure 1.2b).

One of the most obvious current trends in MRI technology is a concerted move toward a large installed base of 3 T systems, particularly for neurological imaging. Some of these scanners are now even being delivered as hybrid or dual-modality imaging systems, such as the promising combination of positron emission tomography and MRI

(see Chapter 19 in *Imaging of the Pelvis, Musculoskeletal System, and Special Applications to CAD*). There is also increasing interest in integrating the soft tissue imaging capability of MRI with interventional procedures, such as MR-guided focused ultrasound surgery (see Chapter 18 in *Imaging of the Pelvis, Musculoskeletal System, and Special Applications to CAD*). Another significant trend is in the area of image acquisition acceleration. The benefits of the latter include reduced motion or flow artifacts, the ability to capture anatomical motion (e.g., as desired in cardiac imaging), shorter scan times for patients, and more cost-efficient use of high demand resources. Improvements are being driven by concepts of sparse sampling (or compressed sensing) that exploit the spatial and/or temporal redundancies inherent in MRI data [37]. They are aided by parallel acquisition schemes built around the use of coil arrays, which provide direct access to spatial information and thus further enable under-sampling of image data [38,39].

Yet another promising initiative is in the area of hyperpolarization. The sensitivity of NMR as a probe is directly coupled to the orientation or alignment of nuclear spins in the applied magnetic field. At room temperature, the net equilibrium alignment (or polarization) of nuclei in any laboratory field is minuscule. In 1950, Alfred Kastler predicted that this polarization could be enhanced through "optical pumping" [40]; by the 1960s, this effect had been demonstrated in NMR experiments [41] and Kastler had been awarded the Nobel Prize in Physics (1966) "for the discovery and development of optical methods for studying Hertzian resonances in atoms." A number of such techniques are now capable of inducing up to a million-fold increase in NMR signal strength for specific nuclei. Examples include optical pumping [41,42], dynamic nuclear polarization [43], and para-hydrogen-induced polarization [44]. The enhancements provided by these methods are crucial when working with low-density or low-concentration nuclei, as encountered in MRI of gases

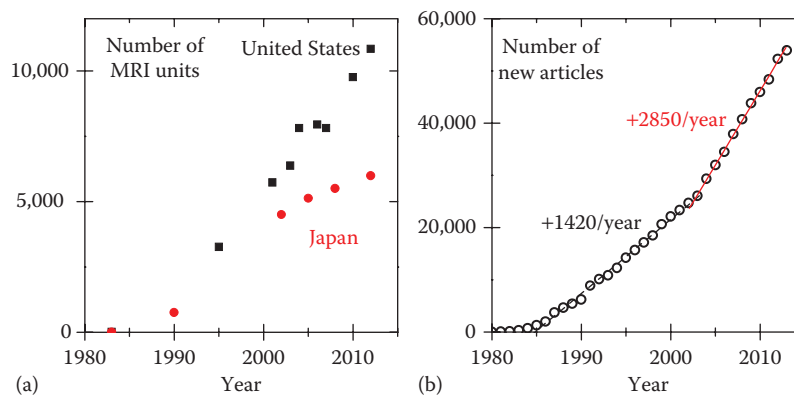


FIGURE 1.2

(a) Number of operational MRI units in two leading countries by year [35]. (b) Number of articles published in a given year making reference to "MRI" or "MR imaging" or "magnetic resonance imaging." (Data from Thomson Reuters *Web of Science* citation indexing service, 2014.)

in lung airspaces (see Chapters 10 and 13 in *Imaging of the Cardiovascular System, Thorax, and Abdomen*), ^{13}C nuclei in metabolites [45,46], injected Si nanoparticles [47,48], or “caged” ^{129}Xe [49,50].

In retrospect, the speed and extent to which the fields of NMR and MRI evolved is remarkable. Varian Associates played a key role in the rapid transition of NMR from the laboratory to a commercial product that revolutionized chemistry. The company was incorporated in 1948 and intentionally settled near Stanford; Martin Packard, part of Bloch’s team, joined shortly thereafter. From that point in time onward, technical development of the field was primarily driven by industry. Similarly, in the case of MRI, as soon as the clinical potential of the technique was recognized, commercial interests drove the necessary technological developments. Throughout the 1980s, a number of companies, including General Electric, Picker, Toshiba, Siemens, and Hitachi, invested heavily in research and development, and promoted clinical evaluation of images. By the 1990s, the installed base had grown to the point where MRI exams were commonplace in industrialized countries. To this day, the number of facilities offering access to MRI continues to grow at an impressive rate, while scan times get shorter and scan quality and resolution continue to increase.

It has been argued that the remarkable evolution of MRI as a clinical imaging modality benefited enormously from the timing of its invention [51]. Had the idea been proposed two decades earlier, key components of the necessary technologies would simply not have been available. In particular, the need for rapid computation of Fourier transforms would have presented an enormous challenge. However, had the idea been proposed two decades later, the demand for new imaging modalities would almost certainly have been greatly reduced. By that point in time, imaging modalities based on well-controlled ionizing radiation (e.g., computed tomography scanners) had evolved to the point where significant hurdles would have been encountered in trying to convince radiologists and medical equipment manufacturers to invest in a new and entirely unproven technology. Even more important is the extent to which the regulatory environment has changed since the 1980s. The level of proof needed to obtain safety approval is now so high that if MRI was proposed today, few if any investors would likely be willing to fund its development.

1.2 Fundamentals of NMR

NMR is intrinsically a quantum mechanical phenomenon. It deals with the dynamics of microscopic objects (atomic nuclei) that behave according to the seemingly

curious (but well-understood) laws of quantum mechanics. Fortunately, one does not need years of background study in quantum mechanics in order to appreciate and understand the essential elements of MRI. The reason is that MRI is invariably used to probe macroscopic objects, involving vast numbers of atomic nuclei. The collective behavior of these nuclei usually washes out the oddities of quantum mechanics, leaving something that bears resemblance to a familiar problem in classical mechanics: the precession of a spinning top in the earth’s gravitational field. It leads to a simple but powerful mathematical description of nuclear dynamics that accurately predicts the outcome of many experiments. In this sense, it often provides a sufficient basis for developing intuition and interpreting experimental results.

Unfortunately, the tendency for many people—beginners and practitioners alike—is to lose sight of the fact that the classical picture of NMR dynamics is simply an analogy: it is not a correct description of dynamics at the microscopic scale, and it can lead to nonsensical explanations of the underlying physics. Examples of situations in which the analogy has been carried too far can be found on popular web sites purporting to explain NMR and MRI using pictures of toy tops or “spinning charged nuclei.” As a rule of thumb, caution is advised whenever such props are encountered.

This section is organized into two parts. The first discusses the key factors that contribute to nuclear spin dynamics, leading to a set of phenomenological equations that encapsulate the essence of the classical description of the problem. These are the famous Bloch equations. The second part then outlines the various means by which the practitioner interacts with the atomic nuclei in a sample, both to induce collective motions and to detect the resulting response.

1.2.1 Bloch Equations and NMR Dynamics

In keeping with the spirit of this book, most of this chapter makes use of the classical picture of NMR. However, in order to motivate that picture, we start in Section 1.2.1.1 with a quick glimpse at a few quantum mechanical aspects of nuclear spin dynamics. The classical treatment of the problem is then presented in Section 1.2.1.2, leading to a statement of the Bloch equations in Section 1.2.1.3.

1.2.1.1 Spin: A Quantum Property

Particles such as the electron, the proton, and the neutron are characterized by their masses and electrical charges. They also possess “spin,” an entirely quantum mechanical property that is associated with an intrinsic angular momentum. (This angular momentum has nothing at all to do with physical rotation.) Spin angular momentum \mathbf{S} is a vector-like quantity; it has three spatial

components and can be oriented in different ways. At the same time, it is different than an ordinary geometric vector. The total “amount” of spin (the length of the arrow) is fixed; it cannot be changed. Moreover, only a subset of all possible orientations is permitted. More precisely, when the component S_i of angular momentum is measured in any particular direction, it is only ever observed to have discrete or “quantized” values. For a spin 1/2 particle (such as the electron, the proton, or the neutron), only two values are possible: $S_i = \pm\hbar/2$, where \hbar is Planck’s constant h divided by 2π . Curiously, this is less than the total spin angular momentum of the particle ($S = \sqrt{3}\hbar/2$). Pictorial representations of spins and spin states relying on arrows and cones are commonplace in MRI, but they are best viewed with caution. None of them are entirely satisfactory when held up to careful scrutiny.

Particles with spin possess a magnetic moment $\mathbf{m} = \gamma \hbar \mathbf{S}$. Here, the constant of proportionality γ is known as the gyromagnetic ratio; each particle with a magnetic moment has a characteristic gyromagnetic ratio. Thus, even though the electron, the proton, and the neutron are all spin 1/2 particles, they have different magnetic moments (see Table 1.1). The same is true of strongly bound collections of particles, such as those that form the nucleus of an atom. The spins of the individual nucleons combine quantum mechanically to yield a well-defined total nuclear spin, usually denoted \mathbf{I} , that is characterized by its magnitude I and by a unique gyromagnetic ratio γ (Table 1.1). Because most applications of NMR and MRI involve nuclei with spin 1/2, this is the only case that is considered below. That being said, there are many important situations in which NMR is employed in connection with nuclei that have higher spin values; the features of the resulting spin dynamics are correspondingly more complex.

TABLE 1.1

Values of Reduced Gyromagnetic Ratios $\gamma/2\pi$ and Nuclear Polarizations for Selected Spin 1/2 Particles and Nuclei

Particle or Nucleus	$\gamma/2\pi$ (MHz/T)	Polarization ($\times 10^{-6}/T$)
Electron	28,025	2,295
Neutron	29.165	2.39
Proton, ^1H	42.577	3.49
^3He	-32.434	-2.66
^{13}C	10.705	0.877
^{15}N	-4.316	-0.353
^{19}F	40.052	3.28
^{31}P	17.235	1.41
^{129}Xe	-11.777	-0.964

Equilibrium polarizations are computed for room temperature ($T = 293$ K) using Equation 1.1 and are expressed on a per unit-magnetic field basis. Examples of nuclei with (a) spin 0 (not suitable for NMR): ^4He , ^{12}C , ^{14}C , ^{16}O ; (b) spin 1: ^2H , ^{14}N ; (c) spin 3/2: ^{23}Na , ^{31}K ; and (d) spin 5/2: ^{17}O .

When an external magnetic field \mathbf{B} is applied to a nucleus (or a particle) possessing a magnetic moment, an interaction takes place. The energy of the nucleus changes by an amount $-\mathbf{m} \cdot \mathbf{B}$, where the scalar (or dot) product “ \cdot ” accounts for the orientation of \mathbf{m} relative to \mathbf{B} . The energy difference between the two states of the nucleus that have spin angular momentum components $\pm\hbar/2$ in the direction of \mathbf{B} is $\Delta E = -\gamma\hbar B$. Peculiar features arise if the tools of quantum mechanics are brought to bear on this problem. These two particular states (often referred to as “spin-up” and “spin-down”) are unique; they do not evolve in time. They are called stationary states. Other states of the nuclear spin \mathbf{I} in a magnetic field are dynamic; they change as a function of time. If a weak magnetic field \mathbf{B}_1 is applied perpendicular to a static magnetic field \mathbf{B}_0 aligned with the z -axis, and B_1 is made to oscillate at an angular frequency $\omega_0 = \Delta E/\hbar = |\gamma B_0|$, the nuclear spin will execute a complex periodic oscillation back and forth between the spin-up and spin-down states via quantum superpositions of the two. If the field B_1 is eventually turned off when the nuclear spin happens to be “half-way” between the two stationary states, its transverse components I_x and I_y will continue to oscillate back and forth between their allowed values... at the angular frequency $\omega_0 = \Delta E/\hbar = |\gamma B_0|$. The phenomenon of magnetic resonance results from the time evolution of spin states in combined static and resonantly oscillating magnetic fields.

For a physical system containing several (or many) nuclei, a full quantum treatment of spin dynamics is only required in particular situations. It is important, for instance, when short-range quantum correlations between interacting spins of nuclei in a molecule are strong. This is usually not the case in problems relevant to MRI, and a semiclassical treatment of spin dynamics is thus sufficient.* Quantum statistical mechanics is used to evaluate the properties and time evolution of nuclear spins in a sample containing a large number of identical nuclei. Unlike individual spins that can be prepared in *pure* quantum states, a large quantum mechanical system is usually in a *mixed state*: a statistical sum of pure states in which many (or most) quantum correlations are washed out.† For instance, in equilibrium at a temperature T (a state known as “thermal equilibrium”), the probabilities p_{up} and p_{down} of observing the up and down states, respectively, are given by the Boltzmann factor:

* A discussion of the need for a fully quantum mechanical approach to the problem can be found in [52] and references therein.

† Consider the following analogy to experiments with polarized light. Pure states of polarization can be combined and transformed: Right and left circularly polarized light can be combined to form linearly or elliptically polarized light. Unpolarized light, however, is different; it cannot be converted to linearly polarized light or to any other polarized state.

$$\frac{p_{\text{down}}}{p_{\text{up}}} = \exp\left(-\frac{\Delta E}{k_B T}\right) \quad (1.1)$$

where k_B is Boltzmann's constant. This ratio is usually very close to 1. The energy difference ΔE set by most laboratory-scale magnetic fields is very small compared to the thermal energy $k_B T$ at room temperature, and thus the probability of observing a spin in its up or down states is very nearly the same. Examples of the very small difference $p_{\text{up}} - p_{\text{down}}$, which is known as the nuclear polarization, are listed in Table 1.1. At the same time, the probability of observing any other spin state (i.e., in a direction tilted away from \mathbf{B}_0) is equal to 0: The sum $p_{\text{up}} + p_{\text{down}} = 1$.

The nuclear magnetic properties of a sample can be determined from the quantum statistical description of its spin dynamics. Each nuclear magnetic moment \mathbf{m} produces a magnetic field, similar to that produced by a tiny closed loop of electric current. Technically, this field is known as that of a magnetic dipole, or simply a "dipolar field." Its orientation depends on the orientation of \mathbf{m} (and hence \mathbf{I}) and decreases rapidly in strength as one moves away from the source. Adding up contributions from many nuclei leads naturally to the concept of a local magnetization density \mathbf{M} , representing the magnetic moment per unit volume. The thermal equilibrium magnetization \mathbf{M}_0 is either parallel or antiparallel to the applied magnetic field \mathbf{B}_0 (depending on the sign of γ) and is proportional to both the local density of nuclear spins in the sample and the thermal equilibrium polarization. During experiments, the nuclear magnetization can be manipulated by applying static and/or time-varying magnetic fields, as discussed below and in Section 1.3. Similarly, the net magnetization of the sample can be inferred through monitoring the associated nuclear magnetic field. Normally, this involves detecting changes in magnetic flux passing through a coil of wire (or similar structure) as the nuclear magnetization evolves in time, as discussed in Section 1.2.2.2.

QUANTUM DYNAMICS OF A SPIN 1/2 PARTICLE

The spin-up and spin-down states of a spin 1/2 particle, which are often denoted $|+\rangle$ and $|-\rangle$, are called pure states. Repeated measurements of their spin angular momentum along a particular axis (as was done in the Stern–Gerlach experiment mentioned in Section 1.1) always yield $\hbar/2$ for the up state and $-\hbar/2$ for the down state. All other pure states, with a maximum spin projection

value $\hbar/2$ in a direction \hat{u} other than $\pm z$, are "linear superpositions" of these states: $\alpha|+\rangle + \beta|-\rangle$, where α and β are complex coefficients such that $\alpha^2 + \beta^2 = 1$. For instance, $(|+\rangle + |-\rangle) / \sqrt{2}$ is the pure state in the \hat{x} direction and $(|+\rangle + i|-\rangle) / \sqrt{2}$ is the pure state in the \hat{y} direction. Unlike the up and down states, these quantum mechanical superpositions are not stationary; they evolve in time. In particular, the direction \hat{u} evolves in exactly the manner predicted by the semiclassical treatment of the time evolution of \mathbf{m} summarized in Section 1.2.1.2.

These concepts can be extended. For example, a two-level atomic system is formally identical to a spin 1/2 quantum system. Transitions between the two (quasi-) stationary states of the atom correspond to the emission or the absorption of a quantum of energy (a photon). This picture forms the basis for the popular—but incorrect—statement that NMR phenomena involve the emission or absorption of radio waves. To understand why this statement is wrong, one need only consider the fact that the electromagnetic wavelength associated with the Larmor frequency produced by a laboratory strength magnetic field is almost always large compared to the dimensions of typical samples and receive coils. In other words, NMR (and particularly MRI) is performed in the near-field electromagnetic regime and the photons that are involved are virtual [53,54].

1.2.1.2 Classical Magnetization Dynamics

A classical description of nuclear spin dynamics is obtained by considering a model system in which the macroscopic magnetic moment \mathbf{m} and the resultant angular momentum \mathbf{J} are coupled such that $\mathbf{m} = \gamma\mathbf{J}$. This seemingly innocuous relationship is the same as that which is obeyed by individual nuclei; only now \mathbf{m} and \mathbf{J} are purely classical quantities (not subject to the subtle restrictions imposed by quantum mechanics). This vector proportionality causes a gyroscopic response to an applied magnetic field, analogous to the dynamics of a spinning top in a gravitational field.

A MISLEADING ANALOGY: THE COMPASS NEEDLE

The relationship $\mathbf{m} = \gamma\mathbf{J}$ is not a general property of macroscopic objects. The magnetic moment of a compass, for example, is locked to the long axis of the needle, which is in turn free to rotate in a

plane about its midpoint. (This is what makes the compass a useful device.) The angular momentum of the compass, however, is proportional to the angular rotation rate of the needle. Thus, $\mathbf{m} \neq \gamma \mathbf{J}$. A compass needle oscillates in a plane about its midpoint; it does not precess like a spinning top or like a collection of nuclear spins! Conversely, the nuclear magnetization in NMR is not locked to the physical orientation of the sample (or subject), as is the magnetization of a compass needle. Thus, in *magic angle spinning* (an NMR technique in which the sample is physically rotated at high speed), it is the lattice of the crystal structure that is spun, not the nuclear magnetization.

In a sample or subject, the local macroscopic magnetization density \mathbf{M} associated with the magnetic moments of the nuclei obeys the classical equation of motion:

$$\frac{d\mathbf{M}}{dt} = \gamma \mathbf{M} \times \mathbf{B}. \quad (1.2)$$

An important feature of this equation is that the amplitude M of the local magnetization (the length of the vector \mathbf{M}) remains constant. At all times, the change in \mathbf{M} is perpendicular to both \mathbf{M} and \mathbf{B} . This behavior is encoded in the vector (or cross) product “ \times ” in Equation 1.2.

A common and convenient graphical tool for depicting the time evolution of \mathbf{M} is the *Bloch sphere*: an imaginary sphere of radius M . With a coordinate system chosen such that the static magnetic field \mathbf{B}_0 is aligned with the z -axis, the corresponding thermal equilibrium magnetization \mathbf{M}_0 can be drawn as a vector pointing from the midpoint of the sphere to the “North Pole.” In this case $\mathbf{M} = \mathbf{M}_0$ and $\mathbf{B} = \mathbf{B}_0$, and thus Equation 1.2 gives $d\mathbf{M}/dt = 0$. That is, nothing happens; \mathbf{M} remains aligned with \mathbf{B}_0 . The same thing is true if \mathbf{M} is somehow aligned to point to the “South Pole” of the Bloch sphere. In the language of Section 1.2.1.1, these situations correspond to the two stationary quantum spin states.

If instead \mathbf{M} is somehow reoriented so that it is canted with respect to \mathbf{B}_0 by some angle other than 180° , as shown in Figure 1.3, Equation 1.2 gives a nonzero result for $d\mathbf{M}/dt$. In this case, the tip of the magnetization vector traces out a circular path at constant latitude, returning periodically to its starting point. This motion is referred to as *free precession*. Unless other processes intervene, it persists forever. It occurs at an angular velocity

$$\Omega_0 = -\gamma B_0 \quad (1.3)$$

or an angular speed $\Omega_0 = -\gamma B_0$, both of which indicate the sense of the motion. The expression *angular Larmor*

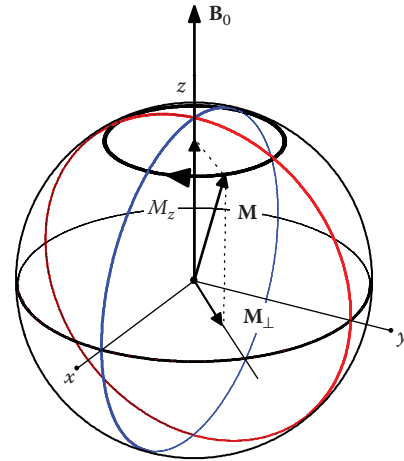


FIGURE 1.3

Graphical representation of solutions to Equation 1.2 for a constant field \mathbf{B}_0 . The time-dependent magnetization vector \mathbf{M} can be associated with a point on a sphere of radius M centered at the origin: the Bloch sphere. The longitudinal component M_z of \mathbf{M} is static, whereas the transverse component \mathbf{M}_\perp rotates in the transverse (x - y) plane at the angular Larmor frequency ω_0 .

frequency is used by some authors to describe Ω_0 , while others take it to mean $\omega_0 = |\gamma B_0|$. Care is thus required any time the absolute sense of rotation is needed. Importantly, the Larmor frequency is independent of the angle to which \mathbf{M} is canted relative to \mathbf{B}_0 .

The phenomenon of NMR enters when a time-varying magnetic field \mathbf{B}_1 is added. Imagine that a weak magnetic field \mathbf{B}_1 is added perpendicular to the static field \mathbf{B}_0 and that \mathbf{B}_1 rotates about \mathbf{B}_0 at the Larmor frequency. That is, the amplitude of \mathbf{B}_1 is constant while its direction changes. In this case \mathbf{M} must precess about both \mathbf{B}_0 and \mathbf{B}_1 , and so the tip of the vector traces out two simultaneous motions: a fast precession about \mathbf{B}_0 and a slow precession about the instantaneous orientation of \mathbf{B}_1 . This produces tightly wound spiral trajectories such as the one shown in Figure 1.4a.

The examples shown in Figures 1.3 and 1.4a reveal that the longitudinal and transverse components of \mathbf{M} exhibit very different dynamical behavior. The dynamics of the longitudinal component M_z (a scalar) correspond to a slow oscillation that involves variations in amplitude. The dynamics of the transverse component \mathbf{M}_\perp (a 2D vector), however, involve a fast rotation about the z -axis at an angular frequency ω_0 combined with a slow oscillation that involves variations in amplitude. Here \mathbf{M}_\perp can be decomposed into orthogonal components M_x and M_y . Equivalently, it can be represented as the quantity $M_x + iM_y$ in the complex plane. The latter approach enables one to use complex algebra rather than matrix algebra in the solution of Equation 1.2. With complex algebra, a rotation of the complex quantity \mathbf{M}_\perp by an angle Φ is obtained by adding Φ to its phase, or multiplying by $e^{i\Phi}$.

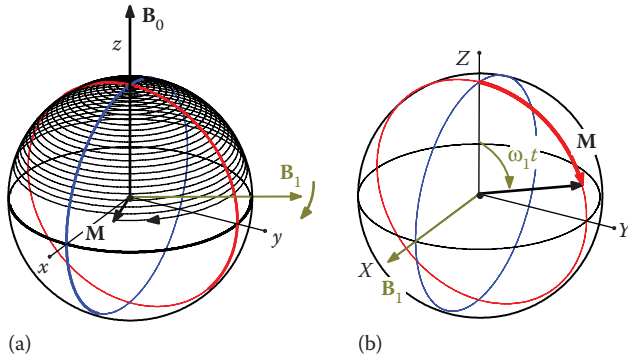


FIGURE 1.4

(a) Part of the spiral trajectory executed by the tip of the magnetization vector under resonance conditions. It results from the cumulative action of a weak magnetic field \mathbf{B}_1 in the x - y plane, rotating at the angular Larmor frequency ω_0 . The amplitudes of the longitudinal (M_z) and transverse (M_\perp) components of \mathbf{M} oscillate periodically. (b) The same trajectory is shown in the rotating frame where \mathbf{B}_1 is fixed along the X -axis (see text).

Setting $\mathbf{B} = \mathbf{B}_0$ and using complex notation for \mathbf{M}_\perp reduces Equation 1.2 to $d\mathbf{M}/dt = -i\gamma B_0 \mathbf{M}_\perp$. The solution to this differential equation is the trajectory shown in Figure 1.3: that is, M_z is constant and $\mathbf{M}_\perp(t) = \mathbf{M}_\perp(0)e^{i\Omega_0 t}$, where $\Omega_0 = -\gamma B_0$. Note here that the sense in which the tip of the vector \mathbf{M} traces out a circle depends on the sign of γ . When $\gamma > 0$ and the Bloch sphere is viewed from above, the sense of the free precession trajectory is clockwise. If $\gamma < 0$, as it is for some of the nuclei listed in Table 1.1, the sense of the free precession trajectory is counterclockwise. The sense of this rotation can be assessed experimentally by using two orthogonal detectors; the phase difference between the signals induced in the two detectors reveals the sense of the trajectory, and hence the sign of γ .

The motion of \mathbf{M} is complicated by the rapid rotation of \mathbf{M}_\perp about \mathbf{B}_0 at the Larmor frequency. It is technically simpler to display and compute trajectories of \mathbf{M} if one works in a reference frame that is also rotating about the z -axis at the Larmor frequency. This is analogous to jumping onto a merry-go-round (or carousel) to better observe the wooden horses and their riders. More precisely, in a reference frame with axes X , Y , and Z rotating at an angular velocity Ω about the Z -axis (with $Z \equiv z$), Equation 1.2 becomes

$$\begin{aligned} \frac{d\mathbf{M}}{dt} &= \gamma \mathbf{M} \times \mathbf{B}_0 + \mathbf{M} \times \Omega \\ &= \gamma \mathbf{M} \times \left(\mathbf{B}_0 + \frac{\Omega}{\gamma} \right) \end{aligned} \quad (1.4)$$

where \mathbf{B} has been set to \mathbf{B}_0 . Comparison of Equations 1.2 and 1.4 reveals that the magnetization now behaves as if it is responding to an apparent field

$$\mathbf{B}_{\text{app}} = \mathbf{B}_0 + \frac{\Omega}{\gamma} \quad (1.5)$$

and that in this frame its angular velocity is $\Omega_0 - \Omega$. If the rotation rate is chosen such that $\Omega = \Omega_0$, the apparent magnetic field \mathbf{B}_{app} vanishes and the magnetization vector \mathbf{M} appears stationary.

Likewise, when a transverse magnetic field \mathbf{B}_1 rotating about \mathbf{B}_0 is added, the time evolution of \mathbf{M} is best described using a reference frame in which \mathbf{B}_1 appears stationary. That is, in a reference frame that is synchronous with \mathbf{B}_1 . In any such frame, Equation 1.2 becomes

$$\frac{d\mathbf{M}}{dt} = \gamma \mathbf{M} \times (\mathbf{B}_{\text{app}} + \mathbf{B}_1). \quad (1.6)$$

If the field \mathbf{B}_1 is resonant with the free Larmor precession of the magnetization (i.e., $\Omega = \Omega_0$ so that $\mathbf{B}_{\text{app}} = 0$), then \mathbf{M} simply rotates around \mathbf{B}_1 at an angular velocity $\Omega_1 = -\gamma \mathbf{B}_1$ and its tip traces out a great circle on the Bloch sphere. This scenario is sketched in Figure 1.4b, where the particular rotating frame that was chosen is the one in which \mathbf{B}_1 is aligned with the X -axis. Viewed in the laboratory frame, this motion produces the spiral trajectory shown in Figure 1.4a. The pitch of the spiral is given by the ratio of magnetic field amplitudes B_1/B_0 .

This last example forms the basis for pulsed NMR. If the field \mathbf{B}_1 is applied on resonance for a finite period of time τ , \mathbf{M} traces out an arc on the surface of the Bloch sphere that subtends an angle $\theta = \omega_1 \tau$. Afterward, \mathbf{M} undergoes free precession as shown in Figure 1.3. Here, $\omega_1 = |\Omega_1|$ denotes the angular nutation frequency and the finite-duration \mathbf{B}_1 field is referred to as a tipping pulse. The angle θ through which \mathbf{M} is rotated is variously referred to as the tip, flip, rotation, or nutation angle. It can be controlled through the amplitude of B_1 or the time τ . Starting from thermal equilibrium where $\mathbf{M} = \mathbf{M}_0$, a 90° or $\pi/2$ tipping pulse will rotate the magnetization into the transverse plane, at which point it will undergo free precession. Alternately, a 180° or π pulse will invert the magnetization, transforming it from \mathbf{M}_0 to $-\mathbf{M}_0$.

If the field \mathbf{B}_1 is applied off resonance rather than precisely at the Larmor frequency, it is still convenient to work in a frame that is synchronous with \mathbf{B}_1 and employ Equation 1.6. The magnetization now rotates around an effective field $\mathbf{B}_{\text{eff}} = \mathbf{B}_{\text{app}} + \mathbf{B}_1$ as shown in Figure 1.5a, and the trajectories traced out by the tip of \mathbf{M} are no longer great circles. If one starts from an initial magnetization \mathbf{M}_0 aligned with \mathbf{B}_0 it is no longer possible to reach the antipodal point on the Bloch sphere where $\mathbf{M} = -\mathbf{M}_0$; that is, perfect π -pulses leading to magnetization reversal are only possible at resonance. As the detuning $|\Omega - \Omega_0|$ increases, the circular

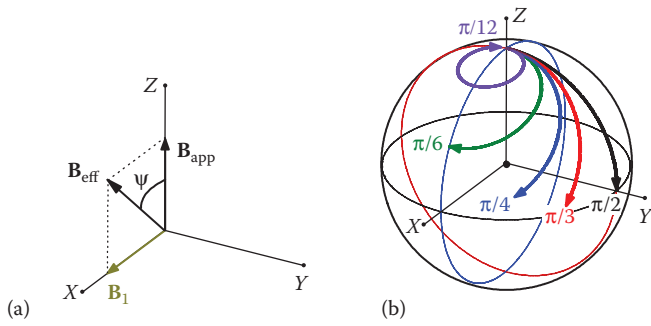


FIGURE 1.5

(a) Components \mathbf{B}_1 and \mathbf{B}_{app} of the effective magnetic field \mathbf{B}_{eff} in the rotating frame. (b) Examples of trajectories on the Bloch sphere for several detunings. In each case, the same evolution time $\tau = \pi/2\Omega_1$ is employed. Values of the angle ψ , which characterize the extent of the detuning (i.e., $\tan \psi = \Omega_1/|\Omega - \Omega_0|$) are indicated.

trajectories traced by the tip of \mathbf{M} on the Bloch sphere (in the rotating frame) become smaller and they are traveled at faster rates (Figure 1.5b). This illustrates the fact that NMR tipping pulses are frequency-selective. Only spins that precess at frequencies close to that of the applied \mathbf{B}_1 field are influenced to any significant degree.

As another example, consider situations where the Larmor precession frequency is not the same for all nuclei in a sample. This inhomogeneity could be the result of an intentionally applied magnetic field gradient, or it could be the result of an intrinsic property of the sample. In either case, there is no unique rotating reference frame in which $\mathbf{B}_{\text{eff}} = 0$ everywhere. Despite this, it is still advantageous to work in a rotating reference frame, a common choice being a frame that rotates at the average Larmor frequency. Figure 1.6 shows a sequence in which (a) a $\pi/2$ pulse is used to rotate the thermal equilibrium magnetization \mathbf{M}_0 into the transverse plane, at which point (b–c) the magnetization undergoes free precession. Unlike the situation pictured in Figure 1.3, the Larmor precession rate is not uniform; some spins precess faster than the average rate and some spins precess slower. This distribution is shown schematically as a series of arrows representing “isochromats”: idealized collections of spins that precess at the same rate. Over time the distribution of angles subtended by these isochromats grows and the net transverse magnetization diminishes. If the sequence pictured in Figure 1.6b and c is allowed to continue indefinitely, the net transverse magnetization will average to zero.

Hahn recognized that the ordered dephasing of isochromats evident in Figure 1.6 can be “undone” by applying another tipping pulse, leading to the formation of a spin echo (or a Hahn echo) [26]. For example, if a π pulse at the average Larmor frequency is applied along the

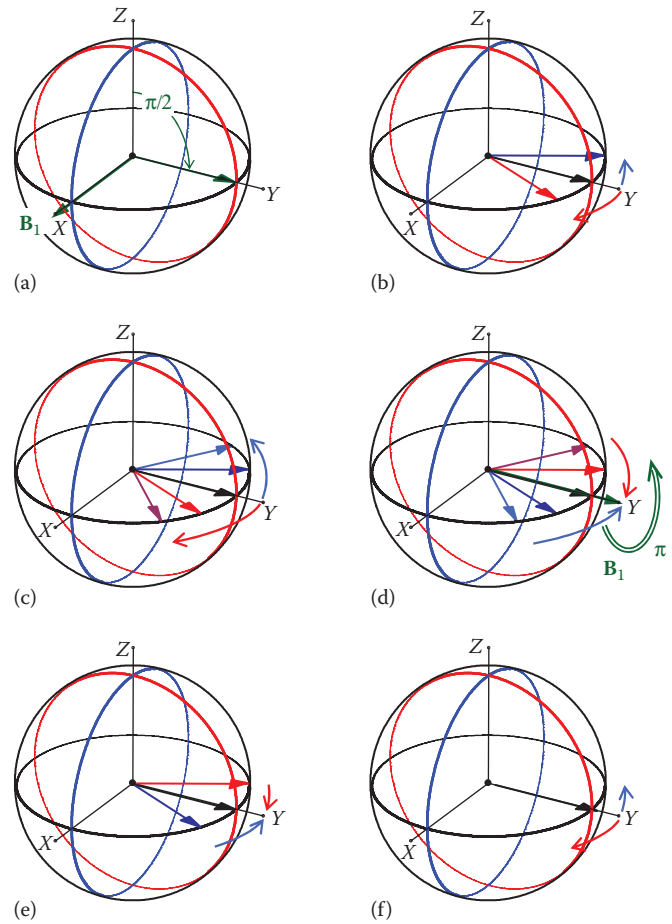


FIGURE 1.6

Spin dephasing and echo formation in the rotating frame: (a) A $\pi/2$ tipping pulse rotates the thermal equilibrium magnetization into the transverse plane. Over time (b,c) some spins precess faster than average while others precess slower. A distribution of azimuthal angles builds up, represented schematically by arrows indicating isochromats. (d) A π pulse applied along the Y-axis when the distribution is as shown in (c) inverts the magnetization. Over time (e,f), the magnetization is refocused, leading to a revival (spin echo) in panel (f). At times later than those shown here the spins continue to dephase.

Y-axis at the time pictured in Figure 1.6c, the isochromats undergo a 180° rotation. Thus in Figure 1.6d the isochromats that precess at the fastest rate are behind the average in terms of total accumulated phase. Conversely, the isochromats that precess at the slowest rate are ahead of the average. As the magnetization continues to execute free precession the angular width of the distribution narrows, forming a revival or spin echo in Figure 1.6f.

1.2.1.3 Irreversibility: The Bloch Equations

The classical theory of nuclear spin dynamics summarized above provides tools for manipulating nuclear spins, and for establishing states characterized by various forms of phase coherence (or correlation) between local magnetization vectors. These states do not persist

forever. Given enough time, and the absence of further manipulations, we expect any interacting spin system to return to thermal equilibrium. That is, a state where \mathbf{M} is aligned with \mathbf{B}_0 and has a magnitude M_0 that is set by the Boltzmann distribution (Equation 1.1).

The processes through which a spin system returns to thermal equilibrium can be complex. They typically involve an exchange of energy between the spins and their environment, and are usually mediated by random magnetic interactions. In many practical circumstances the rate at which this exchange proceeds can be characterized by a phenomenological timescale referred to as the “spin–lattice relaxation time” or the “longitudinal relaxation time.” By convention, it is designated by the symbol T_1 . If the longitudinal component of \mathbf{M} is displaced from thermal equilibrium, the equation of motion governing its return is

$$\frac{dM_z}{dt} = -\frac{(M_z - M_0)}{T_1}. \quad (1.7)$$

Thus, if \mathbf{M}_0 is inverted at time $t = 0$ through application of a π pulse, the return of M_z to equilibrium is given by

$$M_z(t) = M_0 \left[1 - 2 \exp\left(-\frac{t}{T_1}\right) \right]. \quad (1.8)$$

Similarly, coherence of the local transverse magnetization is degraded over time by random interactions or processes that destroy correlations. This degradation is distinct from the dephasing of spins in an inhomogeneous magnetic field described in connection with Figure 1.6, in the sense that it is irreversible. No subsequent manipulation of the nuclear spins can produce an echo or revival. Again, in many practical circumstances, the rate at which coherences of the transverse magnetization are attenuated can be characterized by a phenomenological timescale referred to as the “spin–spin relaxation time” or the “transverse relaxation time.” By convention, it is designated by the symbol T_2 . If the magnetization is manipulated so as to establish a transverse component, and then allowed to undergo free precession, the equation of motion describing the inevitable attenuation of \mathbf{M}_\perp is

$$\frac{d\mathbf{M}_\perp}{dt} = -\frac{\mathbf{M}_\perp}{T_2}. \quad (1.9)$$

Thus, if a $\pi/2$ pulse is applied to a spin system in thermal equilibrium, producing $M_\perp = M_0$ at time $t = 0$, the transverse magnetization subsequently satisfies

$$M_\perp(t) = M_0 \exp\left(-\frac{t}{T_2}\right). \quad (1.10)$$

The full equations of motion for the local magnetization density \mathbf{M} that give rise to these exponential relaxation functions are known as the Bloch equations. They can be written

$$\frac{d\mathbf{M}}{dt} = \gamma \mathbf{M} \times \mathbf{B} - \frac{\mathbf{M}_\perp}{T_2} - \frac{(M_z - M_0)}{T_1} \quad (1.11)$$

where the first term on the right accounts for precession and the other terms account for relaxation. A more compact expression is obtained by introducing the relaxation matrix

$$[R] = \begin{pmatrix} \frac{1}{T_2} & 0 & 0 \\ 0 & \frac{1}{T_2} & 0 \\ 0 & 0 & \frac{1}{T_1} \end{pmatrix} \quad (1.12)$$

and writing

$$\frac{d\mathbf{M}}{dt} = \gamma \mathbf{M} \times \mathbf{B} + [R](\mathbf{M}_0 - \mathbf{M}). \quad (1.13)$$

Even though the original formulation of these equations was based on two phenomenological parameters, there are many important situations in which T_1 and T_2 can be derived from quantum mechanical principles.

ORIGIN AND REGIMES OF RELAXATION

In liquids and gases, rapid random fluctuations of intermolecular orientations and distances permit the use of perturbative methods to evaluate relaxation. This was originally described by Bloembergen, Purcell, and Pound, and has since often been called the BPP theory [55]. A key parameter in this theory is the correlation time, τ_c , which characterizes the relevant fluctuations in the relaxation process. An important result of the BPP theory is that it predicts exponential relaxation for both M_z and M_\perp , and provides values for the corresponding relaxation time constants T_1 and T_2 . In the weak field–fast motion limit ($\omega_0 \tau_c \ll 1$), T_1 and T_2 are equal and proportional to $1/(\omega_0 \tau_c)$. In the opposite high field–slow motion regime, $T_2 \propto 1/(\omega_0 \tau_c) \ll T_1 \propto \omega_0 \tau_c$. A minimum in T_1 is obtained in the intermediate regime, for $\omega_0 \tau_c = 1$. Over the years, more elaborate descriptions have been developed, encompassing different situations of interest in NMR spectroscopy [56] but seldom relevant for MRI of tissues.

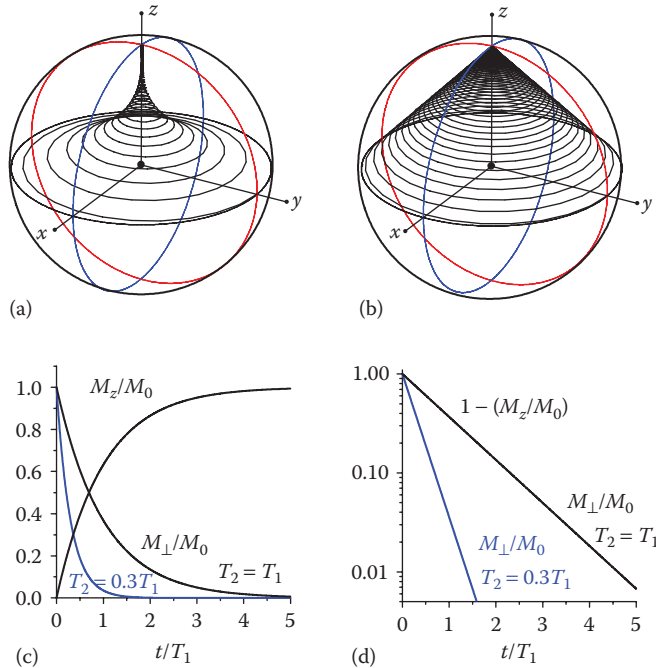


FIGURE 1.7

Influence of relaxation on the time evolution of \mathbf{M} . Trajectories are shown for an initial transverse magnetization aligned with the y -axis for (a) $T_2 = 0.3T_1$ and (b) $T_2 = T_1$. Panel (c) shows the normalized magnitudes of M_z and M_\perp . Panel (d) shows the normalized magnitude of M_\perp again, on a logarithmic scale.

Examples illustrating the combined influence of T_1 and T_2 on the time evolution of \mathbf{M} are shown in Figure 1.7. One of the most striking differences relative to examples in Section 1.2.1.2 is that the trajectory of the tip of \mathbf{M} is no longer restricted to the surface of the Bloch sphere. In Figure 1.7a, T_2 is substantially shorter than T_1 . The resulting spiral collapses toward the z -axis much faster than it climbs toward the North Pole. In Figure 1.7b, the two relaxation times are equal. In this case the spiral trajectory is constrained to a cone-like surface. Figure 1.7c shows the recovery of the longitudinal magnetization M_z and the decay of the transverse magnetization M_\perp for both scenarios. Note that the timescale has been normalized to T_1 , and thus the recovery of M_z is the same for both cases. Finally, the decays of M_\perp are shown again in Figure 1.7d, in order to highlight the fact that they are exponential.

One often encounters situations where the Bloch equations alone are not sufficient to characterize the time evolution of \mathbf{M} . Random atomic or molecular motions, for example, bring in the irreversible effects of diffusion. For liquids and gases these effects can often be characterized in terms of a diffusion coefficient D . More generally, when anisotropic media such as nerve tissue are involved, Equation 1.13 becomes

$$\frac{d\mathbf{M}}{dt} = \gamma\mathbf{M} \times \mathbf{B} + [R](\mathbf{M}_0 - \mathbf{M}) - \nabla \cdot [D]\nabla\mathbf{M} \quad (1.14)$$

where $[D]$ is the diffusion tensor. Equation 1.14 is known as the Bloch–Torry equation [57]. It provides the basis for extracting information about diffusion from NMR experiments and is central to understanding diffusion-weighted and diffusion tensor MRI—both of which are discussed in Chapter 4.

1.2.2 Electrodynamics of NMR

A myriad of MRI sequences exist, but they all start with the preparation of atomic nuclei in some well-defined state other than thermal equilibrium. They all also involve a mapping of the local Larmor precession frequency onto position. Information about the spatial distribution of some aspect of the nuclear magnetization \mathbf{M} (such as the number of contributing nuclei, their local environment, or their displacement over time) is then inferred through monitoring the transverse component of \mathbf{M} (i.e., M_\perp) as it evolves in time (and ultimately relaxes toward thermal equilibrium). A complete image is built up by repeating this measurement over and over again, as the mapping is systematically varied over an appropriate range of parameters.

The general procedures alluded to above are discussed further in Section 1.3 and in more detail in Chapter 2. Before getting to that point, however, it is worth examining the methods by which nuclear spin dynamics are initiated and manipulated. This is the focus of Section 1.2.2.1. It is also useful to understand the methods used to monitor nuclear spin precession. This is covered in Section 1.2.2.2. In both cases, the discussion is limited to the basic physics that is involved, as opposed to the instrumentation that is employed. Next, in order to set the stage for a discussion of specific imaging sequences, it is helpful to examine factors that influence the amplitude of signals that are detected in MRI and the extent to which these signals are influenced by unavoidable (intrinsic) sources of noise. This is the topic of Section 1.2.2.3. Finally, some of the same physics that is wrapped up in signal detection is responsible for undesirable effects: the deposition of RF energy into the subject and peripheral nerve stimulation. These issues are briefly summarized in Section 1.2.2.4 and are discussed further in Chapter 10.

1.2.2.1 Ampère's Law: Currents, Coils, and Fields

The dynamics of nuclear spin precession are controlled during MRI sequences by imposing magnetic fields. These magnetic fields are in turn produced by electric currents, and in some cases by magnetized (and/or magnetizable) materials. The precise manner in which magnetic fields are generated and influenced by these currents and magnetic materials is encapsulated in a

mathematical expression known as Ampère's law.* The various fields that are typically required for MRI are summarized in Sections 1.2.2.1.1 through 1.2.2.1.3.

1.2.2.1.1 Static Field

A magnetic field is required to establish an energy difference between the spin-up and the spin-down states of the nucleus (Section 1.2.1.1). This is done by immersing the subject in a homogeneous magnetic field B_0 . This field is variously referred to as the static field, the main field, the homogeneous field, or simply "Bee-zero" or "Bee-naught". It is conventional to choose the direction of B_0 as the direction that defines the z-axis of the coordinate system.

The simplest and most effective way to produce a strong, homogeneous, and accessible magnetic field is with a solenoid: a single wire wrapped many times around the circumference of a cylinder. When current flows through the wire, a homogeneous magnetic field is produced along the axis of the cylinder.† The central field produced by a thin uniformly wound cylindrical solenoid of length L and diameter D such as the one shown schematically in Figure 1.8 is given by

$$B_0 = \frac{\mu_0 n I}{\sqrt{1 + \left(\frac{D}{L}\right)^2}} \quad (1.15)$$

where $\mu_0 = 4\pi \times 10^{-7} \text{ Tm/A}$ is the permeability of free space and n represents the winding density. Choosing $L = 1.8 \text{ m}$, $D = 0.9 \text{ m}$, $I = 190 \text{ A}$, and $7 \times 10^3 \text{ turns/m}$ (i.e., a wire wrapped around the cylinder approximately 12,600 times for a length totaling a few tens of kilometers) yields $B_0 = 1.5 \text{ T}$, which is typical of the fields employed in the majority of clinical imagers in service today.‡ In practice, superconducting solenoids are usually employed to generate this magnetic field. These "magnets" are operated in a "persistent" mode at cryogenic temperatures such that the current flows through the solenoid in a closed loop, without a power supply and effectively without dissipation. The main field magnet and the associated cryogenic vessel account for the bulk of the tubelike infrastructure that one normally sees when looking at an MRI scanner.

A key function of the main magnetic field is to set a uniform Larmor precession frequency for all of the

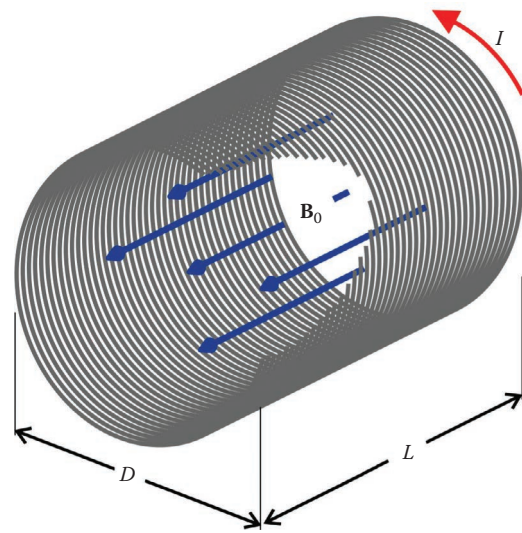


FIGURE 1.8

A solenoid of length L and diameter D carrying current I . The central magnetic field B_0 is given by Equation 1.15. The large number of turns required for an MRI magnet results in a coil that has many layers. Normally, the winding density is varied to improve the field homogeneity. A second (larger) solenoid wound outside the primary magnet, and in the opposite sense, provides "active shielding." The net field at the center of the combined magnet is somewhat weaker than that of primary magnet alone, but the external field is dramatically suppressed.

nuclei that are going to be imaged.§ In practice, a simple finite length solenoid (or other winding pattern, or other magnet geometry) is not sufficient to produce the native magnetic field homogeneity that is required for high-resolution MRI. A number of shim (or correction) coils and judiciously placed ferromagnetic (magnetizable) materials are also used to create a central volume over which a very high degree of magnetic field uniformity (and hence nuclear spin precession rate) is achieved. The subject is then positioned such that the region to be imaged coincides with this "sweet spot." In typical whole-body clinical MRI systems, B_0 varies by at most a few parts-per-million over a 30 cm-diameter sphere at the center of the magnet (distortions equivalent to adding or subtracting a fraction of the Earth's magnetic field to B_0).

The nominal Larmor precession rate for ^1H nuclei (protons) in a 1.5 T imager is 63.87 MHz (see Table 1.1). In a 3 T imager, it is 127.73 MHz. Yet higher static magnetic fields can and have been employed for MRI, and yield substantial improvements in signal-to-noise ratio (SNR).¶ Lower fields can also be employed and offer other advantages

* Additional considerations come into play when high frequencies are involved. In such cases, Maxwell's equations (which include the physics described by Ampère's law) are employed.

† The field is perfectly homogeneous only for an infinitely long solenoid.

‡ To put this in perspective, the Earth's magnetic field is of order 10^{-4} T or 1 G.

§ It is also usually responsible for establishing the thermal equilibrium polarization of the nuclei, and hence the maximum amplitude of the signals that can be detected.

¶ They also present new challenges, such as limitations on the amplitude and duration of RF pulses that can be applied, as discussed in Sections 1.2.2.2 and 1.2.2.4.

TABLE 1.2

Classification of MRI Scanners by Static Field Strength

Range	Field Strength (T)	¹ H Frequency (MHz)
High	$B_0 > 2$	$f > 85$
Conventional	$0.5 < B_0 < 2$	$20 < f < 85$
Low	$0.1 < B_0 < 0.5$	$4 < f < 20$
Very-low	$0.001 < B_0 < 0.1$	$0.04 < f < 4$
Ultra-low	$B_0 < 0.001$	$f < 0.04$

Over time the definition of what constitutes a “high-field” system has drifted upward. During the 1980s, a 1 T scanner would have been considered a high-field system. Most clinical systems in service today operate at 1.5 T, but the fastest growing segment of the market is for 3 T systems. The production of low-field scanners has dropped significantly in recent years. Scanners that operate in the very-low and ultra-low regimes are employed for niche applications.

such as the possibility of open geometries where ready access to the subject is possible and the imager environment is less likely to be claustrophobic. The magnets at the heart of these low-field systems can be wound from superconducting wire or ordinary copper wire, or they can be constructed from permanent magnets. Imagers that operate at yet lower magnetic fields have been developed in connection with a variety of different research initiatives. A crude classification of MR imagers by magnetic field strength is given in Table 1.2.

1.2.2.1.2 Gradient Fields

Spatial resolution in MRI is accomplished by inducing well-defined distortions of the main magnetic field, which produce the desired mapping between nuclear precession frequency and position. These distortions are created by running currents through sets of coils that are designed for this purpose.* This is precisely what Lauterbur did in his original demonstration (Figure 1.1). It is conventional to refer to these distortions as magnetic field gradients and to the coils that produce them as gradient coils.

In a solenoidal main field geometry, a longitudinal field gradient $G_z = dB_z/dz$ increases the field strength toward one end of the cylinder and decreases it toward the other. Transverse gradients ($G_x = dB_z/dx$ and $G_y = dB_z/dy$) increase the field strength on one side of the cylinder and decrease it on the other (to the left and the right of the subject, or above and below, or in fact in any transverse direction that is desired). Simple sets of coils generating such field gradients are sketched in

* Large magnetostatic forces are exerted on these coils whenever current flows through them. Imaging sequences normally require rapid switching or pulsing of the field distortions. The sudden changes in mechanical stress exerted on the coil support structure produce the characteristic patterns of acoustic noise that are generated by MRI scanners.

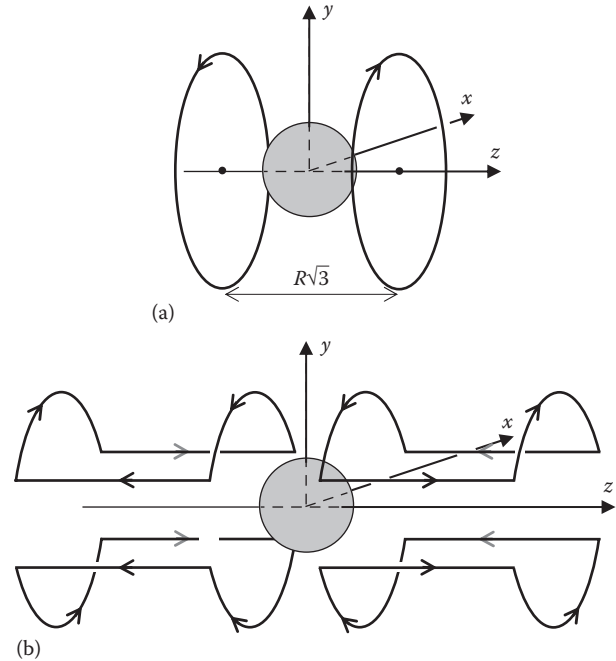


FIGURE 1.9

Elementary coil winding patterns that generate field gradients over a central region (indicated by the gray sphere). The main magnetic field B_0 is assumed to be in the \hat{z} -direction. (a) A Maxwell coil pair, with currents flowing in opposite directions, creates a z -odd field variation and hence produces a longitudinal gradient G_z . For the specified coil spacing, the z^3 term in the series expansion of the field vanishes, and G_z has a high uniformity. (b) A Golay coil consists of four saddle coils with currents flowing in the specified directions. It produces a transverse gradient G_y . Current flowing in the wires parallel to the z -axis does not produce a field in the \hat{z} -direction and does not affect G_y . The positions of the arcs and the angle that they subtend are chosen so as to maximize gradient uniformity. Note that the orientation of the x , y , and z axes differs from that chosen in Section 1.2.1: the z -axis is still aligned with B_0 , but is now shown as being horizontal as it is for almost all clinical MRI systems.

Figure 1.9. Improved performance is obtained using analytical or numerical methods to obtain complex yet compact winding patterns for which gradient strengths and uniformity are maximized and the associated coil inductance is minimized [58,59].

Normally the field distortions induced by gradient coils are very small. For example, at 1.5 T they are typically less than 1% of B_0 over the Field of View (FOV). A careful examination of the magnetic fields produced by gradient coils reveals that they always do more than simply provide the nominal “desired effect.” For example, a coil that produces a longitudinal field gradient dB_z/dz always produces a gradient in orthogonal components of the field (dB_x/dx and/or dB_y/dy).† In many

† The term *field gradient*, which is ubiquitous in MRI, is really a misnomer. It is technically a tensor quantity with nine components. In free space, constraints imposed by Maxwell’s equations reduce the number of independent terms in the tensor to 5.

instances, the effects produced by these “concomitant gradients” (or Maxwell terms) are negligible, simply because the magnitude of the transverse components of the distorted field (B_x and B_y) are so small compared to the longitudinal field B_0 . However, this is not always the case, particularly when very strong gradients or weak static fields are employed.

1.2.2.1.3 RF Field

Up to this point, all of the coils that have been discussed serve to control and manipulate the longitudinal magnetic field B_z , and hence the Larmor precession frequency. They do not produce fields that induce transition between nuclear energy levels. For this one usually needs a field directed orthogonal to B_z that oscillates at the Larmor frequency or close to it. That is, the field B_1 of Section 1.2.1.2 that causes the net nuclear magnetization \mathbf{M} to rotate about an axis perpendicular to z , as long as it is applied.

In practice, the rotating field B_1 is often obtained as one of the two counter-rotating components of a linearly polarized oscillating field (see Figure 1.10). The other component, which rotates in the opposite sense, is detuned from the nuclear resonance by twice the Larmor frequency. It thus has almost no effect on nuclear spin dynamics. This linearly polarized oscillating field is produced by driving a time-varying current $i_0 \cos \Omega t$ through a coil with an appropriate geometry. The amplitude of this current (and hence the amplitude of the field B_1) and the time period over which it is applied control the tip (or flip) angle. Dozens of such coils have been developed and employed for MRI; they are generically known as transmit coils (or antennas), TX coils, RF coils, or even B_1 coils (“Bee-one coils”). Here, the reference to radiofrequencies is simply the fact that Larmor precession frequencies are typically in the radiofrequency range of the electromagnetic spectrum.

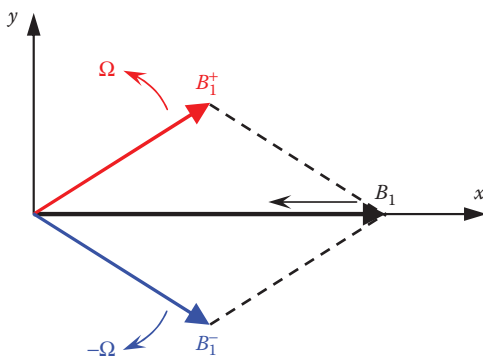


FIGURE 1.10

A linearly polarized oscillating magnetic field $B_1(t) = B_1^m \cos \Omega t$ aligned with the x -axis can be decomposed into two rotating components with equal and constant amplitudes but opposite angular velocities. That is, $B_1(t) = (B_1^m / 2)[\exp(i\Omega t) + \exp(-i\Omega t)]$.

More often than not RF coils are “tuned”; inductive and capacitive elements in the circuit are balanced so that the net electrical impedance is purely resistive at the Larmor frequency. This facilitates efficient coupling between the transmitter and the coil, and hence efficient production of the largest possible B_1 field amplitudes.

Normally, RF coils are designed to produce a reasonably homogeneous oscillating field over the volume to be imaged, in order to generate reasonably uniform flip angles [60,61]. Some designs involve little more than a circular conducting loop, tuned to resonate at the Larmor frequency. A current flowing through this loop produces a magnetic field that is roughly aligned with its axis, and that is reasonably strong out to a distance of order its radius. This is an example of a “surface coil” (see Figure 1.11); it is convenient in situations where the tissues of interest are close to the surface and flip angle homogeneity is not terribly important. Other RF coils involve more sophisticated arrangements of current paths. The birdcage coil, for example, involves a series of long straight parallel conductors uniformly arranged around the periphery of a cylinder (Figure 1.11). These conductors act like inductors, and are carefully and individually tuned with capacitors to produce a resonance at the desired frequency; at resonance, the current flowing through the wires at any instant in time

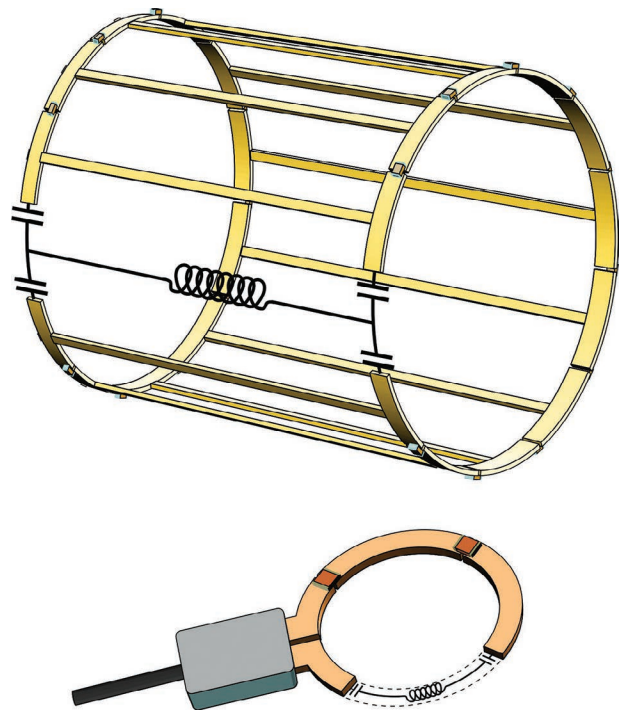


FIGURE 1.11

A surface coil (lower) and a birdcage coil (upper), both of which can function as a transmit (TX) coil, a receive (RX) coil, or a combined TX/RX coil. A few of the capacitive and inductive elements in each coil are shown schematically.

is a sinusoidal function of the azimuthal angle. This arrangement is an example of a “volume coil”; it produces a very homogeneous B_1 field directed perpendicular to the axis of the cylinder. Importantly, the intensity of this field remains constant in time while its direction rotates. In the reference frame rotating at the Larmor frequency, this field is constant.

The use of coils like the birdcage that produce rotating or “circularly polarized” B_1 fields (as opposed to linearly polarized fields; see Figure 1.10) can be very important at high frequencies where essentially all of the energy delivered to the coil by the transmitter is ultimately dissipated in the subject. In effect, half of a linearly polarized oscillating field is wasted from an NMR perspective. It does, however, contribute to the rate at which energy is deposited in the subject. This point is discussed further in Section 1.2.2.4.

1.2.2.2 Faraday’s Law: NMR Detection

A changing magnetic field creates an electric field E . The faster the magnetic field changes, the more intense is the resulting electric field. This is the essence of Faraday’s law of induction,^{*} which forms the basis for the detection of most NMR signals.

The net precessing nuclear magnetization that is established after a tipping pulse is applied has associated with it a small magnetic field whose orientation rotates about the z -axis at the Larmor frequency. This changing magnetic field produces an associated electric field, which also changes as a function of time. If an open loop of wire (or a coil with many turns) is placed near the region in which the precessing nuclei are situated, and arranged so that it intercepts some of the changing magnetic flux produced by those nuclei, an *electromotive force* (emf) or potential will be established between its two ends (see Figure 1.12). This emf is proportional to the amplitude of the transverse component of the precessing magnetization and to the precession frequency. It depends on the actual distribution of magnetization in an extended sample and on the geometry of the coil and sample. The principle of reciprocity [62] enables one to conveniently compute this elementary emf as a function of the coil shape and source position. The total emf, $e(t)$, induced around the loop is obtained by integration over the entire sample volume, taking into account variations in the phase of the nuclear magnetization across the sample and geometrical weighing factors. Typically, the detected emf is very small and needs to be amplified as soon as possible to avoid unnecessary degradation of signal quality due to interference from external noise sources. The

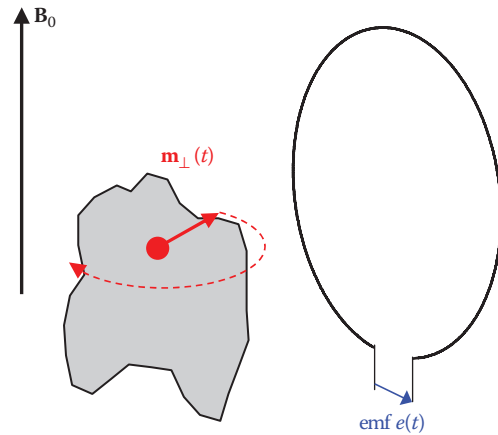


FIGURE 1.12

An elementary volume (the red sphere) within the magnetized sample (the gray volume) has a net magnetic moment m_{\perp} . Its precession in the applied field B_0 gives rise to an oscillating magnetic flux in the nearby detection loop, hence to an emf $e(t)$ oscillating at the corresponding Larmor frequency ω_0 .

use of tuned detection coils conveniently provides a significant enhancement prior to amplification. For a tuned coil with quality factor Q , the resulting signal is $S(t) = Qe(t)$.

The coil used to detect nuclear precession signals is another RF coil, in the sense that it operates at the same frequency as the B_1 coil. It is typically referred to as a detection coil, a receive coil (or antenna), an RX coil, or a pickup coil. In some cases the same physical coil is used for both transmit and receive functions, but more often than not one wants to minimize cross talk or interference between the two. When two coils are used, efforts are made to ensure that they are orthogonal. If this is not done, the intense B_1 field produced by the transmit coil will induce an enormous emf across the terminals of the receive coil, complicating attempts to detect subsequent nuclear induction signals.

Just as is the case for B_1 coils, one is often interested in using volume detection coils designed to have reasonably uniform sensitivity to precessing magnetization over the entire volume of interest. In such cases, signals are approximately proportional to the total (integrated) magnetization of the sample. Alternatively, surface coils or arrays of surface coils can be employed. The recorded signal(s) from these arrays provide coarse information about the location of the magnetization within the sample [38,39].

1.2.2.3 Signal Amplitude Considerations

It is often stated that NMR is an inherently insensitive experimental probe. What is meant by this is that the conventional signature of NMR precession—the induced emf $e(t)$ discussed in Section 1.2.2.2—is

^{*} As was the case with Ampère’s law in Section 1.2.2.1, Faraday’s law provides a precise mathematical connection between B and E .

invariably a weak signal that is readily obscured by noise. Weak or not, those signals still encode a wealth of information about the local magnetic environment in which the sample nuclei are immersed.

Qualitative appreciation for the relative strength or weakness of conventional NMR signals can be gleaned through considering alternative methods for monitoring nuclear precession that were developed early in the history of the field. Rabi's 1938 demonstration of NMR [19], for example, involved measuring the flux of molecules in a weak but fully polarized beam. A deflection of the beam, and hence a change in detected intensity, was observed when an oscillating magnetic field was applied at the Larmor frequency. Two decades later, Brossel and Cagnac [63] realized Kastler's proposal [64] for optical detection of nuclear magnetic resonance in optically polarized atomic vapors. A change in the polarization of fluorescent light emitted by low-density Hg vapor was observed in response to a change in the nuclear spin state, driven by an oscillating magnetic field applied at the Larmor frequency.

These pioneering experiments have two features in common that distinguish them from conventional NMR. First, in both cases the measurement was indirect, involving the detection of molecules or visible photons rather than the magnetic field produced by nuclei. The energy scale associated with each detected event (molecule or photon) was in the electron-volt range: 9 orders of magnitude more than the energy difference between the two nuclear spin states in the applied magnetic field (see Table 1.1 for characteristic values). Second, in both cases the nuclear polarization was very far from equilibrium ($|p_{\text{up}} - p_{\text{down}}| \approx 1$), dramatically enhancing the contrast between measurements performed on- and off-resonance. Recall here for scale that the equilibrium nuclear polarization at room temperature in a 1 T magnetic field is of order 10^{-6} or 1 ppm, and yet smaller in weaker fields. Combined, these features represent an astounding 15 order-of-magnitude advantage (or enhancement in signal amplitude) relative to direct detection of the nuclear transition under equivalent conditions. Of course, this discrepancy is compensated in part through the huge increase in density that is obtained when liquid or solid samples are employed rather than molecular beams or dilute atomic vapors. Nevertheless, one is left with the naïve impression that direct detection of NMR presents a daunting signal acquisition problem relative to the highly leveraged schemes described above.

A proper evaluation of this problem requires consideration of two parameters: the amplitude of the detected signal and the amplitude of the detected noise. The quality of the signal is then expressed in terms of a signal-to-noise ratio. For given sample and coil geometries the detected emf $\epsilon(t)$ in conventional NMR scales

as B_0^2 ; one factor of B_0 comes from the dependence of the equilibrium magnetization on field (Equation 1.1) and the other comes from the fact that the induced emf is proportional to the time derivative of the precessing magnetization (Faraday's law), and hence $\omega_0 = |\gamma B_0|$ (Equation 1.3). Estimating the field dependence of the detected noise is more involved and requires an understanding of its physical origin. Here it is useful to make a distinction between extrinsic and intrinsic sources. Noise from extrinsic sources, such as RF interference (often referred to as electromagnetic interference or EMI) or noise generated by amplifiers and recording electronics, can typically be suppressed or minimized through design: MRI systems are typically installed in a shielded room (or Faraday cage) for precisely this reason. Noise from intrinsic sources, however, is unavoidable: it typically arises from thermal agitation of electrical charges (Johnson noise) in the sample and the detection coil. If the sample is the dominant source of intrinsic noise, Faraday's law introduces the same factor of $\omega_0 = |\gamma B_0|$ to the corresponding induced emf as it does for the signal, and thus the SNR increases linearly with B_0 . If the coil is the dominant source of intrinsic noise, however, SNR increases more rapidly as the operating field is increased, scaling as $B_0^{7/4}$ [65,66].

For most clinical imaging applications, the sample (i.e., tissues in the subject's body) acts as the dominant source of intrinsic noise, particularly as the operating field is increased. Conversely, in low or very-low magnetic fields, when small samples are employed (as is the case for MRI of small animals or in MR microscopy experiments) or when nonconducting samples are probed, the detection coil tends to dominate the intrinsic noise. In such cases it can be advantageous to use cold probes or even superconducting coils [67]. The spectral density of thermal noise appearing across a resistor R at temperature T is given by $\sqrt{4k_B RT}$, and thus gains are realized through reducing both R and T . More exotic options for enhancing SNR in MRI for niche applications are being explored, such as the use of SQUID-based detectors [68] and optical magnetometers [69] for ultra-low-field applications and force detection in magnetic resonance force microscopy for submicron resolution MRI [70].

1.2.2.4 Health Safety Considerations

The application of time-varying magnetic fields can lead to undesirable effects. Intense RF tipping pulses induce strong Faraday electric fields, which can in turn drive eddy currents and cause energy dissipation in the tissues of a subject. This energy dissipation rate has a strong frequency dependence, scaling as ω^2 over many decades in frequency [66]. In high-field MRI systems, where RF frequencies in the VHF band of the electromagnetic spectrum (30–300 MHz) and above are

employed, situations can arise in which most of the RF power delivered to the B_1 coil is dissipated in the subject [71,72]. Likewise, fast switching of magnetic field gradients can also induce strong Faraday electric fields. In this case the characteristic frequencies are much lower and energy dissipation in the subject is usually not a concern. Instead, the induced electric fields E can cause peripheral nerve stimulation [73]. In both cases, restrictions and standards imposed by regulatory bodies and international commissions [73] limit the maximum permissible Faraday electric fields that can be induced. For RF fields, these limitations are normally expressed in terms of specific absorption rates (SARs); for switched magnetic field gradients, limitations are variously expressed in terms of peak values of dB/dt and/or E , as well as direct volunteer-based observations of nerve stimulation thresholds. These issues are discussed further in Chapter 10.

1.3 Fundamentals of MRI

This chapter began with a brief and qualitative description of Paul Lauterbur's first published MRI experiment, as summarized in Figure 1.1. In this section, we revisit that experiment and examine somewhat more precisely the nature of the 1D projections of the "NMR response" that he obtained. We then survey a few key modern approaches to MR image acquisition, based on the use of pulsed NMR and Fourier transform methods. In effect, this sets the stage for the remainder of the book.

This section is organized into three parts: The first deals with methods for generating 1D projection images; the second deals with the acquisition of data for 2D and 3D images; and the third identifies the primary methods through which the "NMR response" is tuned or adapted to reflect different aspects of the nuclear environment. It is at this point in the process—the sensitization of NMR signals to different "contrast mechanisms"—that crucial connections are formed between the acquired data and the underlying structure and function of the tissues that are imaged.

1.3.1 Effect of a Field Gradient: 1D Imaging

Consider a uniform magnetic field $\mathbf{B}_0 = B_0 \hat{z}$ upon which is superimposed a uniform gradient $G \equiv dB_z/dk$, in the direction \hat{k} . The strength of the resulting magnetic field is a function of position \mathbf{r} . As long as concomitant gradients can be ignored, it can be written:

$$B_0(\mathbf{r}) = B_0(0) + G\hat{k} \cdot \mathbf{r}. \quad (1.16)$$

The Larmor precession frequency of nuclei subjected to this field similarly becomes a linear function of position, and takes on the same value in any given plane oriented perpendicular to \hat{k} . If a time-varying magnetic field \mathbf{B}_1 oriented perpendicular to \hat{z} is then applied at angular frequency ω , resonance will only occur in the vicinity of one such plane. For a continuous wave (CW) NMR experiment, where the field B_1 is applied continuously, the width of this region is of order $\delta r = 1/(\gamma GT_2)$.

If the NMR signal is received using a coil that has uniform coupling to all parts of the sample (e.g., a long solenoid or a birdcage coil), its amplitude is proportional to the number of nuclei in the band that is excited. Sweeping or stepping the frequency ω or the field B_0 causes the resonant band to translate across the sample, generating a 1D map or projection image of the magnetization density. The frequency (or field) scale for this mapping is set by the strength G of the field gradient. More precisely, the projection represents the convolution of a Lorentzian line shape (whose width is set by the spin–spin relaxation rate $1/T_2$) with the net nuclear magnetization density. As long as $1/T_2$ is appropriately small, the signal reflects the spatial distribution of M_0 . This is illustrated in Figure 1.13a, which shows the spectrum that is expected for a magnetic field gradient applied perpendicular to the axis of a cylindrical sample of radius a . It thus represents the signal that Lauterbur would have observed had he used only one tube in his experiments. By using two tubes instead of one, and by varying the direction \hat{k} in which the gradient was applied relative to their axes, he was able to resolve both

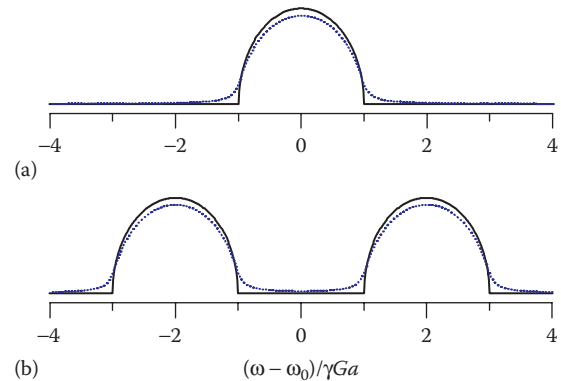


FIGURE 1.13

(a) Anticipated CW NMR spectra for a cylindrical sample of radius a in a uniform magnetic field gradient G applied perpendicular to its axis. *Solid line:* Ignoring the effects of relaxation, the spectrum is proportional to $\sqrt{1 - (\omega - \omega_0)^2 / (\gamma Ga)^2}$, which is simply the projected width of the cylinder at a distance $(\omega - \omega_0) / (\gamma Ga)$ from its axis. *Dotted line:* With some relaxation added to the Bloch equations (but ignoring the effects of diffusion), sharp features are smoothed out; here $\gamma GaT_2 = 2$. (b) Anticipated spectra for two parallel cylindrical samples, a situation modeling Lauterbur's experiment summarized in Figure 1.1. Solid and dotted lines correspond to relaxation being ignored or included, as in (a).

their physical extent and their apparent separation, as illustrated in Figure 1.13b. In the remainder of this section we will assume that $1/(\gamma GaT_2) \ll 1$ and that the effects of diffusion can be ignored.

The procedure outlined above—sweeping the static magnetic field (or the frequency at which the field B_1 is applied) and collecting CW NMR spectra for various field gradient orientations—is time consuming. Most modern implementations of Lauterbur’s experiment employ pulsed NMR, in which the field B_1 is only applied for finite periods of time. Subsequent to these tipping pulses, the nuclear magnetization \mathbf{M} undergoes free precession and induces a time-varying emf in the detection coil:

$$e(t) \propto \int_{\text{sample}} M_{\perp}^0(\mathbf{r}) \cos[\gamma B_0(\mathbf{r})t + \phi] e^{-t/T_2}. \quad (1.17)$$

Here $M_{\perp}^0(\mathbf{r})$ is the local amplitude of the transverse magnetization immediately after the tipping pulse (at time $t = 0$), the local position-dependent Larmor frequency $\gamma B_0(\mathbf{r})$ depends on the local magnetic field strength (given by Equation 1.16) and the phase ϕ is a parameter that depends on the particular tipping pulse that is applied and on the position of the coil with respect to the sample.

Normally, the signal that is actually recorded during a pulsed NMR experiment is obtained by mixing the detected high-frequency emf $e(t)$ with a reference signal at a comparable frequency and fixed phase. The reference signal is often referred to as the local oscillator (LO), and also forms the basis for generating the field B_1 . A common choice is thus to set $\omega_{\text{LO}} = \gamma B_0(0)$. The resulting “signal” is complex:

$$S(t) = \int_{\text{sample}} M_{\perp}^0(\mathbf{r}) \exp[i(\gamma G \hat{k} \cdot \mathbf{r})t] e^{-t/T_2}. \quad (1.18)$$

It has two components: one that is in-phase with the LO and another that is 90° out of phase (or “in-quadrature”) with the LO. These are referred to as the real and imaginary parts of the signal, respectively. Equation 1.18 represents the sum of contributions to the detected emf arriving from all parts of the sample, as viewed in a frame of reference rotating at the local oscillator frequency ω_{LO} . The complex nature of $S(t)$ keeps track of the sense of rotation in the rotating frame, and thus discriminates between frequencies that are above or below ω_{LO} .

Figure 1.14a shows the anticipated signal $S(t)$ following a single tipping pulse applied to the same cylindrical sample used to generate Figure 1.13a. The rapid apparent attenuation of this “free induction decay”

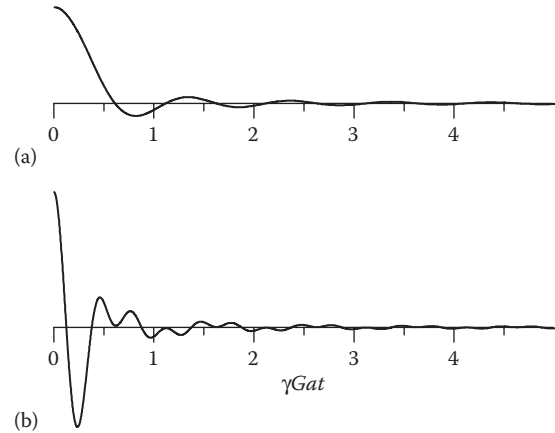


FIGURE 1.14

(a) Real part of the NMR free induction decay signal (Equation 1.18) anticipated for a cylindrical sample of radius a in a uniform magnetic field gradient of amplitude G directed perpendicular to its axis, as was the case in Figure 1.13a. The phase of the signal is constant, and its imaginary or quadrature component (not displayed) is zero at all times. The effects of relaxation and diffusion have been ignored. (b) Anticipated signal for two parallel cylinders, analogous to the situation in Figure 1.13b.

(FID) merely reflects the fact that a magnetic field gradient has been imposed. The nuclear precession frequency varies as a function of position across the sample or subject, and the net emf detected by the coil is subject to destructive interference between the contributions generated at different locations (see Figure 1.12). For a sample of size a , the characteristic timescale for the apparent decay of $S(t)$ is of order $1/(\gamma Ga)$. Figure 1.14b shows the expected signal for the sample of Figure 1.13b: the high-frequency modulation within the same overall signal lifetime corresponds to interference, or “beats,” between contributions from the two tubes. This illustrates how an applied frequency-encoding gradient links spatial characteristics of a sample to spectral features in the acquired data.

The information present in Figure 1.14 can be used to recover the same spectra as were obtained in the CW NMR experiment. All that is required is a calculation of the Fourier transform of $S(t)$ after setting $S(-t) = S^*(t)$, where the $*$ indicates complex conjugation. This Fourier transform represents the distribution of frequencies present in the FID, and hence the distribution of nuclear precession frequencies in the sample as the FID was recorded. Thus, apart from the necessary computations, the time required to obtain a 1D projection image of the sample via pulsed NMR is dramatically reduced relative to the CW approach outlined earlier.

The dephasing of the precessing magnetization that is responsible for the apparent decay in Figure 1.14 occurs on a timescale that is short compared to that set by relaxation (i.e., T_2). It can be represented pictorially with a series of isochromats, as was done in Figure 1.6.

* $S(t)$ is only called the signal for convenience. It is merely proportional to the voltages that are digitized and recorded.

Similarly, it can be refocused in order to generate spin- or gradient-echoes. Therefore, for example, if the direction of the field gradient is inverted at time τ , the recorded signal at subsequent times (i.e., $t > \tau$) becomes

$$S(t) = \int_{\text{sample}} M_{\perp}^0(\mathbf{r}) \exp[i(\gamma G \hat{k} \cdot \mathbf{r})(2\tau - t)] e^{-t/T_2}. \quad (1.19)$$

Spins that were initially precessing faster than average end up precessing slower after the inversion, and vice versa. By the time $t = 2\tau$, the net phase accumulated by all spins in the sample is the same and an echo is formed. The amplitude of the recorded signal at $t = 2\tau$ is the same as it was at $t = 0$, to the extent that relaxation and diffusion can be ignored. Moreover, the recorded signal at times $t > 2\tau$ evolves just as it did immediately after the tipping pulse (see Figure 1.14). And, just as was the case for the initial FID, calculating the Fourier transform of the recorded echo data yields a 1D projection image of the sample.

This gradient echo formation procedure can be generalized. For example, the sense in which G is applied can be periodically reversed at times $\tau, 3\tau, 5\tau, \dots$ as shown in Figure 1.15a to form an echo train; that is, a periodic revival of phase coherence across the sample. The inevitable decay of the peak response every time an echo is formed provides information about irreversible processes such as relaxation and diffusion. More generally, the strength of the field gradient before and after the reversal can be changed; an echo is then formed every time the time integral of $G(t)$ vanishes.

HARD OR SOFT PULSES: WHICH SPINS ARE EXCITED?

When a magnetic field gradient G is present, the spatial uniformity of the flip angle induced by an RF pulse depends critically on the amplitude of the field B_1 . This effect was alluded to in connection with Figure 1.5. When an intense RF pulse is applied, the effective magnetic field \mathbf{B}_{eff} in the rotating frame is dominated by \mathbf{B}_1 . The angle ψ shown in Figure 1.5 is thus always very close to 90° and the trajectory traced by the tip of the magnetization vector \mathbf{M} on the Bloch sphere is essentially part of a great circle. The condition required for this to be true everywhere in the sample is that $B_1 \gg Ga$, where a is the size or extent of the object in the direction that G is applied. This condition defines what is known as a “hard pulse.” The FID pictured in Figure 1.14 was implicitly launched using a hard RF pulse; even though a magnetic

field gradient was present, the trajectory of \mathbf{M} during the pulse and the initial phase of the transverse magnetization immediately afterward were effectively the same at all points in the sample.

A very different result is obtained when a “soft pulse” is applied. In this limit, $B_1 \ll Ga$, and the effective magnetic field \mathbf{B}_{eff} in the rotating frame is dominated by the apparent field \mathbf{B}_{app} (Equation 1.5), which—because of the applied gradient—is a function of position. To first approximation, only spins located near the plane $\hat{k} \cdot \mathbf{r} = (\omega - \omega_0) / (\gamma G)$ are strongly influenced by B_1 . This forms the basis for “slice selection,” which is discussed further in Section 1.3.2. The width of the region over which a soft pulse is effective in rotating the magnetization depends on the duration of the pulse, and the spatial profile of the flip angle can be controlled by the shape of the RF pulse envelope in time.

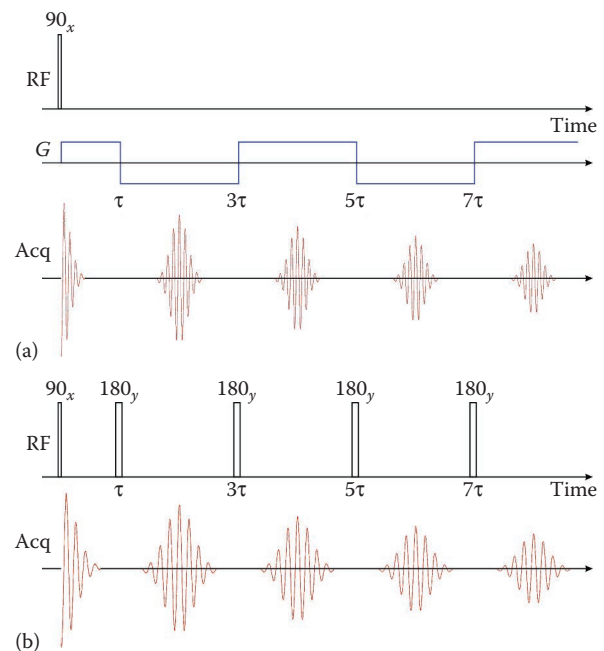


FIGURE 1.15

Schematic diagram showing the synchronization of applied B_1 fields (RF), switched gradient fields (G), and acquired nuclear induction signals (Acq) for two pulse sequences. Both begin with a 90° RF tipping pulse that rotates the thermal equilibrium magnetization into the transverse plane. In the first example (a), the sense of the applied magnetic field gradient G is periodically reversed, creating a train of gradient echoes. In the second example (b), the phase of the magnetization is periodically inverted by applying 180° tipping pulses, creating a train of spin echoes. The time between the initial RF pulse and the peak of the first echo (or the time between successive echoes) is referred to as the echo time and is conventionally denoted TE or T_E . Often, sequences such as those shown here are repeated, in which case the repetition time (the time between successive applications of the sequence) is conventionally denoted TR or T_R .

Alternatively, the spin-echo procedure outlined in connection with Figure 1.6 can be used to generate echoes and echo trains as shown in Figure 1.15b. In this case the gradient G remains the same, but the phase of the magnetization is inverted by applying 180° tipping pulses about any axis in the transverse plane. The phase advance of “fast” spins near one end of the sample suddenly becomes a phase lag, and vice versa for “slow” spins on the other end. If the inversion occurs at time τ , an echo is formed at time 2τ .

The signals that are obtained when spin- and gradient-echoes are formed are similar, but they are not identical. Experimental constraints often dictate the selection of one approach over the other. For example, a weakness of the gradient-echo technique is that the inversion of field gradients is usually imperfect. The current delivered to the gradient coils (and hence the field they produce) can certainly be inverted, but the static magnetic field itself is never perfectly uniform. Thus, inverting the applied magnetic field gradient G is not quite the same as inverting the total magnetic field gradient. Even worse, when strong gradients are applied (or weak magnetic fields are employed), the notion of a magnetic field gradient itself breaks down, and the influence of orthogonal components of the field on the time evolution of \mathbf{M} needs to be considered. In either case, a progressive loss of phase coherence occurs on a timescale that is often shorter than the transverse relaxation time T_2 . This particular limitation can be eliminated by generating spin echoes instead of gradient echoes. To the extent that perfect and uniform 180° tipping pulses can be generated, inverting the phase of the magnetization leads to coherent echo formation irrespective of imperfections in B_0 . However, a limiting factor for spin-echo sequences when human subjects are involved is the need to employ short, high-amplitude B_1 fields in order to obtain uniform 180° rotations. In high-field systems, the energy associated with these pulses is invariably deposited in the subject and can pose a safety hazard (see Section 1.2.2.4 and Chapter 10).

Ultimately, the precision of the spectrum representing the 1D distribution of the precessing magnetization that is obtained from the Fourier transform of the recorded signal is limited. The time variation of $S(t)$ is sampled at discrete points in time (at a sampling frequency f_s) and over a finite period of time (T_{obs}) that is usually centered* on

the echo formation time 2τ or $2n\tau$. The spectrum obtained from these data (through a discrete Fourier transform procedure) has a frequency resolution $1/T_{\text{obs}}$ and extends over a frequency range $\pm f_s/2$. This frequency resolution limits the maximum spatial resolution of the 1D projection image described above to $1/(\gamma G T_{\text{obs}})$. Factors such as a finite transverse relaxation time T_2 (see Figure 1.13), diffusion, and noise (see Section 1.2.2.3) all serve to reduce this maximum resolution. The frequency range also plays an important role; it imposes a finite FOV given by $f_s/(\gamma G)$. The FOV must be larger than the physical extent of the sample or subject; otherwise folding artifacts associated with undersampling of high-frequency components of the signal can occur. Artifacts in MRI are discussed further in Chapter 9.

1.3.2 2D and 3D Imaging Methods

Paul Lauterbur’s 2D NMR images of water-filled capillaries (such as the one shown in Figure 1.1) were obtained through a process of mathematical inference known as “back projection.” This involves combining several 1D or “line” images, each acquired in a different direction in the same plane, to form a 2D image on a grid of points by iteratively modeling the unknown distribution of nuclear magnetization. Although this approach to image reconstruction played an important role in the early evolution of MRI, it is not often used today. Modern MR image reconstruction relies heavily on the phase and frequency encoding of the (precessing) nuclear magnetization in a sample, multidimensional Fourier transform techniques, and the selective excitation of nuclei in specific, well-defined planes or bands intersecting the sample or subject. The general principles by which MR image data are acquired are discussed next. Further examples are presented in Chapter 2. We begin with the process of “slice selection,” which is ubiquitous in modern MRI.

A soft RF tipping pulse applied in the presence of a magnetic field gradient $G\hat{k}$ is selective. Maximum rotation of the magnetization vector is obtained in the plane defined by $\hat{k} \cdot \mathbf{r} = (\omega - \omega_0)/(\gamma G)$; elsewhere the effect is much smaller. For small tip angles,[†] the spatial width of the region that is influenced is proportional to the spectral width of the pulse, which is in turn inversely proportional to its duration in time τ . Rectangular RF pulse envelopes, where the field B_1 has a constant amplitude for a finite period of time, yield awkward sinc-shaped slice profiles in space; the plane on which the maximum rotation is obtained is symmetrically flanked by a series

* The observation window does not have to be centered on the echo time; a recording of half of the echo starting or ending with the signal at the echo time is sufficient. This is possible because of the symmetry of echoes, which result from the fact that the phase of the precessing magnetization was uniform at the start of the experiment. A full recording of a FID starting immediately after a tipping pulse (as implied by the example shown in Figure 1.14) is often technically difficult to acquire; a delay following the tipping pulse is normally required to avoid saturation of the detection electronics by the applied B_1 field. A symmetric echo is usually recorded to increase SNR, but asymmetric echoes are often used in ultrafast acquisition schemes.

[†] More sophisticated pulse shaping procedures are required when large tip angles are desired [74], because of the nonlinear dependence of flip angle on RF amplitude and detuning illustrated in Figure 1.5.

of side lobes. A sinc-shaped RF pulse envelope is much more useful. Modulating the amplitude of B_1 in time such that

$$B_1(t) = B_1(0) \frac{\sin\left(\frac{\gamma G \Delta z t}{2}\right)}{\left(\frac{\gamma G \Delta z t}{2}\right)} \equiv \text{sinc}\left(\frac{\gamma G \Delta z t}{2}\right) \quad (1.20)$$

yields a rectangular (uniform) slice of width Δz in space. Starting from thermal equilibrium, a soft sinc-shaped, small-tip-angle RF pulse applied in the presence of a “slice selection gradient” conveniently produces a transverse magnetization that is uniform in amplitude over this slice and zero elsewhere. This would be ideal for imaging if not for the fact that, by the end of the pulse, the magnetization is strongly dephased by the gradient. The simplest and most convenient way to deal with this is by generating a gradient-recalled echo. Rather than turning off the slice selection gradient at the end of the RF pulse, its direction is momentarily reversed as shown in Figure 1.16. At the point in time where the echo is formed ($t = T_e$), the transverse magnetization in the sample or subject is uniform in a well-defined slice of thickness Δz and zero elsewhere. This slice can be positioned anywhere in the sample by choosing an appropriate frequency for B_1 . As long as a 2D image can be generated from the selectively excited magnetization in each slice, a full 3D image can be recorded.

A strategy for generating a 2D image following slice selection is summarized in Figure 1.17. It proceeds as

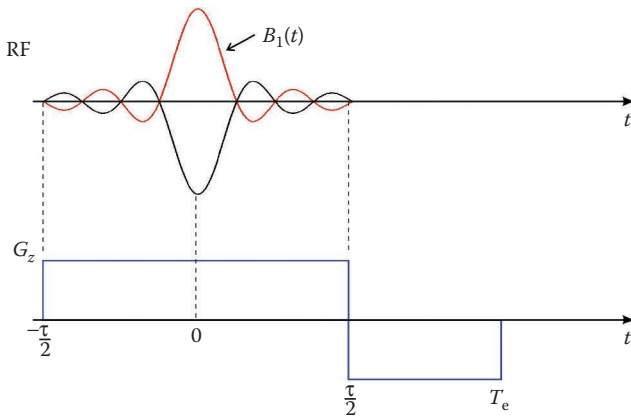


FIGURE 1.16 A soft sinc-shaped RF pulse for selective excitation of the transverse magnetization in a well-defined slice. The slice selection gradient G_z is reversed at the end of the RF pulse in order to unwind the accumulated phase of the magnetization. An echo is formed at the same instant that the gradient is turned off ($t = T_e$). The schematic depiction of the RF pulse only indicates the envelope or amplitude of $B_1(t)$ (see Equation 1.20). The high-frequency oscillation of B_1 at $\omega \sim \omega_0$ is not shown. Note that truncation of the sinc function distorts the rectangular slice profile. We have ignored such effects in this discussion.

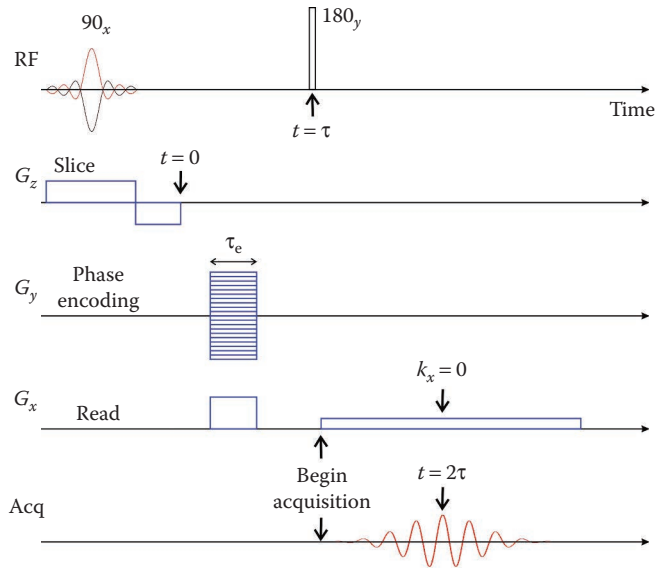


FIGURE 1.17 Outline of a sequence for 2D Fourier transform imaging. The first RF pulse in the presence of a gradient ($G_z \hat{z}$) excites one rectangular slice of the sample (see Figure 1.16). The second RF pulse at $t = \tau$ generates a spin echo that peaks at time $t = 2\tau$. A phase-encoding gradient ($G_e \equiv G_y \hat{y}$) applied during the first free evolution period establishes a gradient in the phase of the transverse magnetization along the y -axis. Each time this sequence is repeated, a different phase encoding gradient is employed. An orthogonal read (or frequency-encoding) gradient ($G_r \equiv G_x \hat{x}$) is then applied while the echo is acquired. The read gradient causes the transverse magnetization to dephase, and thus an extra gradient pulse is applied along \hat{x} during the first free evolution period to compensate. The net phase shift caused by the read gradient at the echo maximum is thus zero. In practice, refinements to this basic scheme (such as the use of a selective 180° RF pulse) are often either necessary or desirable.

follows: A gradient G_e is first applied in the plane of the slice for a time period τ_e . This establishes a gradient in the phase of the transverse magnetization as it undergoes free precession. This gradient is consequently referred to as a phase-encoding gradient. Next, a 180° RF pulse is applied at time $t = \tau > \tau_e$ to invert the phase of the precessing magnetization (relative to the phase of the pulse). A second gradient G_r is then applied in the plane of the slice but perpendicular to G_e , in anticipation of the spin echo generated by the 180° rotation. This gradient is known as a read gradient* because it is applied during signal acquisition.

As a concrete example, assume that a rectangular slice of thickness Δz has been selected perpendicular to the z -axis and that G_r and G_e happen to be applied along the x and y axes, respectively. The recorded signal (analogous to Equation 1.19) in the vicinity of the echo is of the form

* It is also referred to as a frequency-encoding gradient, in connection with the manner in which it is employed for Fourier transform spectroscopy. For imaging, signals are processed in terms of the spatial modulation of the magnetization in the sample (k -space) rather than frequency.

$$S(t > \tau) = \int_{\text{sample}} M_{\perp}^0(\mathbf{r}) \exp[i(k_x(t)x + k_y y)] e^{-(t/T_2)} \quad (1.21)$$

where $k_x(t) = \gamma(2\tau - t)G_r$ and $k_y = \gamma\tau_e G_e$ are interpreted as components of a wave vector, describing the spatial modulation of the magnetization in the sample. Equivalently, the recorded signal represents

$$\begin{aligned} S(k_x, k_y) &= \int_{\text{sample}} M_{\perp}^0(\mathbf{r}) \exp[i(k_x x + k_y y)] e^{-(t/T_2)} \\ &= \Delta z \int_{\text{slice}} M_{\perp}^0(x, y) \exp[i(k_x x + k_y y)] e^{-(t/T_2)} \end{aligned} \quad (1.22)$$

at a fixed value of k_y and over a range of k_x . More generally, ignoring attenuation and assuming $S(k_x, k_y)$ is known for all values of k_x and k_y , the 2D inverse Fourier transform of Equation 1.22 is $M_{\perp}^0(x, y)\Delta z \propto M_{\perp}^0(x, y)$, which is the desired 2D spatial distribution of nuclear magnetization in the slice.

In practice, the sequence shown in Figure 1.17 is repeated N_e times for evenly spaced values of k_y corresponding to phase-encoding gradients in the range $-G_{\max} < G_e < G_{\max}$. Each iteration probes $S(k_x, k_y)$ for evenly spaced values of k_x set by the sampling rate f_s and the acquisition time. The result is a 2D Cartesian array of data spanning a range of “ k -space,” as shown in Figure 1.18a. The (discrete) 2D inverse Fourier transform of these data corresponds to a 2D image of the transverse nuclear magnetization in the slice. The FOVs in the direction of the read gradient and the direction of the phase-encoding gradient are $f_s/(\gamma G_r)$ and $N_e/(2\gamma\tau_e G_{\max})$, respectively.

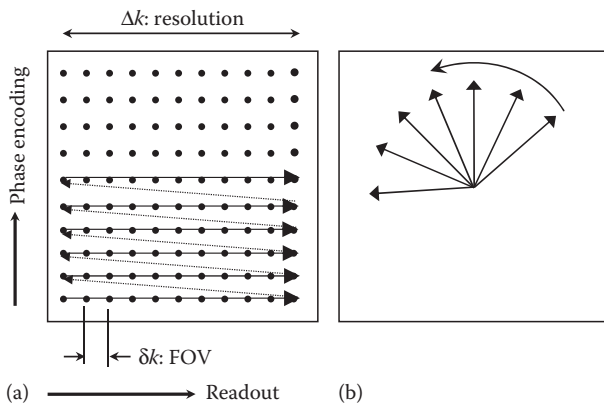


FIGURE 1.18

Examples of trajectories for 2D k -space sampling. (a) Cartesian mapping of the plane is obtained from a series of data acquisitions, each with different phase encoding in the y -direction. (b) Radial mapping is obtained from acquisitions along different azimuthal directions, each one of which samples the center of k -space.

k -SPACE IN MRI

The signals that are detected and recorded in MRI do not usually come from localized regions of the sample or subject. Rather, they represent spatially modulated depictions of the nuclear magnetization integrated over the entire volume to which the receive coils are sensitive. This spatial modulation is imposed and controlled by the linear magnetic field gradients that are applied and can be characterized by a wave vector \mathbf{k} . A mathematical analysis of this problem shows that the detected signals are nothing more than Fourier transforms (or a spatial frequency representation) of the nuclear magnetization distribution that is being imaged.

The space in which the components k_x and k_y of the wave vector \mathbf{k} are the natural parameters of the recorded signal $S(k_x, k_y)$ is conventionally referred to as k -space or reciprocal space. As long as enough data are acquired to characterize $S(k_x, k_y)$ in reciprocal space, one need only perform an inverse Fourier transform to reconstruct an image of the magnetization distribution in real space [75–78].

Imaging sequences, such as the one shown in Figure 1.18, are often thought of as being recipes or instructions for acquiring data that span k -space. Strictly speaking, standard receive coils only sense the average nuclear magnetization and hence only monitor the centre of k -space. It is actually the Fourier transform of the magnetization that traverses k -space as the imaging sequence is executed. Nevertheless, all of the information needed for image reconstruction is still acquired.

The concept of k -space or reciprocal space is commonplace in disciplines such as crystallography, solid-state physics, and optics. Often one is able to view or resolve key features of a complex system much more clearly in k -space than in real space. An important example is the phenomenon of Bragg diffraction, which occurs when coherent short-wavelength radiation is scattered from the lattice planes of a crystalline solid or other periodic structure. This is not the case in MRI. Generally, little or no useful information is evident when one looks at raw k -space MRI data. It is only when the real space image is reconstructed that useful information is revealed.

Many variants of this basic strategy exist. For example, the spin echoes generated by the sequence shown in Figure 1.17 are readily replaced with gradient-recalled echoes, which in some cases are useful for fast imaging. Even faster rates are possible when echo

trains are formed after each excitation. In this way a different phase-encoding gradient can be used each time the magnetization is refocused, enabling rapid passage through k -space. This is the basic idea behind echo-planar imaging. Other approaches include radial acquisition schemes, as suggested in Figure 1.18b. These enable frequent resampling of the center of Fourier space, which can be used to help minimize movement artifacts to which other sequences are susceptible. It also permits fast time resolution using sliding window methods. Yet other strategies for acquiring data in k -space employ spiral (or interleaved spiral) trajectories or partial (e.g., half-plane) acquisition schemes [79].

1.3.3 Contrast

As described, the imaging strategies outlined in Sections 1.3.1 and 1.3.2 all have one thing in common: the acquired signal—and hence the image that is generated—nominally reflects the local magnetization density in the sample or subject. If proton NMR is employed, the signal strength scales with the density of H atoms, which are abundant in the water and lipids of all tissues. As a result, these strategies yield anatomical images with poor contrast and are of little use from a clinical perspective. It is only when they are “tuned” or modified to probe physical processes that are tissue-specific that the real potential of MRI is realized. Sensitization—or “weighting”—of the acquired signal to these processes can yield significantly enhanced contrast between organs with similar proton density, or between regions characterized by normal and pathological behavior. A brief summary of common image weighting schemes is given below. Much more information can be found in later chapters.

Sensitization of acquired NMR signals to nuclear relaxation—irreversible processes characterized by the phenomenological parameters T_1 and T_2 —is the most obvious and most widely employed method of enhancing image contrast. In fact, Lauterbur’s original demonstration of 2D MRI included a T_1 -sensitized image [1]. And, in connection with this image, he noted that longer than normal values of T_1 had been observed in malignant tumors [80].

T_1 weighting of images is naturally obtained when the sequence repetition time T_R (or TR) is comparable to the longitudinal relaxation time. Endless repetition of the sequence under these conditions does not provide enough time for the magnetization to return to thermal equilibrium between iterations. As a result, the steady-state magnetization is suppressed relative to its thermal equilibrium value M_0 such that

$$M = M_0 \frac{1 - \exp\left[-\left(\frac{T_R}{T_1}\right)\right]}{1 - \cos \theta \exp\left[-\left(\frac{T_R}{T_1}\right)\right]} \quad (1.23)$$

where θ is the tip angle of the RF pulse (see Figure 1.4).

For appropriate choices of θ and T_R , the magnetization in regions characterized by short values of T_1 will recover more than that in regions characterized by long values of T_1 . They will thus provide larger amplitude signals and ultimately be rendered as more intense regions on an image. In normal tissues, fat (lipids) is characterized by shorter values of T_1 than water, and thus it appears white in T_1 -weighted MR images. Thus, cerebral white matter appears white on a T_1 -weighted MR image because it contains more lipids than does gray matter.

T_2 weighting of images is obtained when the echo formation time T_e (or TE) is comparable to the transverse relaxation time T_2 . Under these conditions, significant irreversible dephasing of the transverse magnetization occurs between the initial RF excitation (tipping pulse) and the measurement of the signal amplitude. This effect is responsible for the factor $\exp(-t/T_2)$ appearing in the various expressions for $S(t)$ and $S(k_x, k_y)$ in Section 1.3.2; when $t = T_e \sim T_2$, the resulting signal attenuation becomes significant. This is precisely the opposite of the effect observed for T_1 weighting. That is, regions characterized by strong T_2 relaxation yield relatively weak NMR signals and are rendered as being dark on a T_2 -weighted image. Regions characterized by strong T_1 relaxation yield relatively strong NMR signals and are rendered as being bright on a T_1 -weighted image. Lipid-rich regions tend to be characterized by stronger relaxation (both T_1 and T_2) than water-rich regions. They thus tend to appear relatively brighter in T_1 -weighted images and darker in T_2 -weighted images.

The intrinsic T_1 - or T_2 -weighted contrast induced by tissue structure or pathology is not always strong enough to reveal features or to enable a sensitive and specific diagnosis. In such cases, it is sometimes possible to enhance contrast through the introduction of paramagnetic contrast agents. Gadolinium-based contrast media injected into the bloodstream, for example, enhance T_1 relaxation and yield a local increase in T_1 -weighted signal intensity wherever blood perfusion is present. Small iron oxide and other superparamagnetic particles, on the other hand, enhance T_2 relaxation and lead to a corresponding decrease in T_2 -weighted signal intensity wherever they are present. The use of contrast agents in MRI is discussed in Chapter 3.

A third physical process that can be used for image contrast is diffusion, as was discussed in Section 1.2.1.3.

Like relaxation, diffusion naturally causes an irreversible degradation of NMR signal coherence. One method for diffusion-weighting MR images involves adding a bipolar field gradient pulse between the initial RF excitation and the rest of the normal sequence. The purpose of this bipolar gradient is to imprint a helix-like pattern on the phase of the magnetization along the direction of the diffusion-sensitizing gradient, and then unwind it. If the nuclear spins contributing to the NMR signal are stationary, this manipulation has no effect. However, if diffusion occurs on the timescale of the pulse, the net phase accumulated by a particular spin depends on the (random) path it happened to follow in the interim. The net result is an attenuation of the net transverse magnetization by a factor $\exp(-D\gamma^2 G^2 \tau_d^3)$, where D is the relevant diffusion coefficient, G is the sensitizing gradient amplitude, and τ_d is a timescale associated with the duration of its application.* As with T_2 weighting, regions characterized by significant diffusion yield less signal than those characterized by little diffusion, and are thus rendered as being darker.

Diffusive motions are often *restricted*. Atoms or molecules might be relatively free to wander short distances (“free diffusion”), but then encounter barriers that impede longer range motion. In such cases, when pulsed gradient NMR techniques are used to measure D , an *apparent diffusion coefficient* (ADC) is observed. This ADC is invariably smaller than the free diffusion coefficient, but the factor by which it is reduced depends on the timescale over which the measurement is made. ADC imaging of the brain is routinely performed in cases of ischemic or hemorrhagic stroke (see Chapter 23).

An additional factor arises when the confining structures are anisotropic, as is the case with nerve fiber tracts. In this case, ADC mapping can be performed as a function of the direction in which the sensitizing gradient is applied. The resulting diffusion tensor images provide information about both the direction and the magnitude of the underlying diffusion processes. Pulsed-field diffusion tensor MRI of the brain enables visualization of white matter fiber tracts and can be used to map subtle changes associated with diseases such as multiple sclerosis or epilepsy.

Further discussion of diffusion-sensitized MRI can be found in Chapter 4. The same general strategies used to characterize diffusion can be adapted to probe displacements and velocities (flow imaging; Chapter 9 in *Imaging*

of the Cardiovascular System, Thorax, and Abdomen) and have many applications to angiography.

References

1. Lauterbur PC (1973) Image formation by induced local interactions: Examples employing nuclear magnetic resonance. *Nature* 242:190–191.
2. Carr HY (1952) Free precession techniques in nuclear magnetic resonance. PhD thesis, Harvard University, Cambridge, MA.
3. Walters GK, Fairbank WM (1956) Phase separation in He³-He⁴ solutions. *Phys. Rev.* 103:262–263.
4. Osheroff DD, Gully WJ, Richardson RC, Lee DM (1972) New magnetic phenomena in liquid He³ below 3 mK. *Phys. Rev. Lett.* 29:920.
5. Abragam A (1961) *Principles of Nuclear Magnetism*. Oxford University Press, Oxford.
6. Cowan B (1997) *Nuclear Magnetic Resonance and Relaxation*. Cambridge University Press, Cambridge.
7. Ernst RR, Bodenhausen G, Wokaun A (1987) *Principles of Nuclear Magnetic Resonance in One and Two Dimensions*. Oxford University Press, New York.
8. Slichter CP (1990) *Principles of Magnetic Resonance*. Springer-Verlag, Berlin, Germany.
9. Levitt MH (2001) *Spin Dynamics: Basics of Nuclear Magnetic Resonance*. John Wiley & Sons, West Sussex, England.
10. Callaghan PT (2011) *Translational Dynamics and Magnetic Resonance: Principles of Pulsed Gradient Spin Echo NMR*. Oxford University Press, Oxford.
11. Blümich B (2000) *NMR Imaging of Materials*. Clarendon Press, Oxford.
12. Brown MA, Semelka RC (2010) *MRI: Basic Principles and Applications*. John Wiley & Sons, Hoboken, NJ.
13. Callaghan PT (1991) *Principles of Nuclear Magnetic Resonance Microscopy*. Oxford University Press, New York.
14. Kuperman V (2000) *Magnetic Resonance Imaging: Physical Principles and Applications*. Academic Press, New York.
15. Kimmich R (1997) *NMR Tomography, Diffusometry, Relaxometry*. Springer-Verlag, Berlin, Germany.
16. Purcell EM, Torrey HC, Pound RV (1946) Resonance absorption by nuclear magnetic moments in a solid. *Phys. Rev.* 69:37–38.
17. Bloch F, Hansen WW, Packard M (1946) Nuclear induction. *Phys. Rev.* 69:127.
18. Bloch F, Hansen WW, Packard M (1946) The nuclear induction experiment. *Phys. Rev.* 70:474–485.
19. Rabi II, Zacharias JR, Millman S, Kusch P (1938) A new method of measuring nuclear magnetic moment. *Phys. Rev.* 53:318.
20. Gerlach W, Stern O (1922) Das magnetische moment des silberatoms. *Z. Physik* 9:353.

* An alternate and commonly employed variant of this measurement involves the insertion of a time delay Δ between two short oppositely directed gradient pulses. In this case, the degree to which the signal is attenuated by diffusion during this time period is characterized by a parameter that is conventionally referred to as the “ b -value,” as discussed further in Chapter 4.

21. Gorter CJ (1936) Negative result of an attempt to detect nuclear magnetic spins. *Physica* 3:995.
22. Gorter CJ, Broer LJJ (1942) Negative result of an attempt to observe nuclear magnetic resonance in solids. *Physica* 9:591–596.
23. Torrey HC (1949) Transient nutations in nuclear magnetic resonance. *Phys. Rev.* 76:1059–1068.
24. Hahn EL (1950) Nuclear induction due to free Larmor precession. *Phys. Rev.* 77:297–299.
25. Bloch F (1946) Nuclear induction. *Phys. Rev.* 70:460–474.
26. Hahn EL (1950) Spin echoes. *Phys. Rev.* 80:580–594.
27. Arnold JT, Dharmatti SS, Packard ME (1951) Chemical effects on nuclear induction signals from organic compounds. *J. Chem. Phys.* 19:507.
28. Singer JR (1959) Blood flow rates by nuclear magnetic resonance measurement. *Science* 130:1652–1653.
29. Jackson JA, Langham WH (1968) Whole-body NMR spectrometer. *Rev. Sci. Instrum.* 39:510.
30. Garroway AN, Grannell PK, Mansfield P (1974) Image formation in NMR by a selective irradiative process. *J. Phys. C: Solid State Phys.* 7:L457–L462.
31. Mansfield P, Maudsley AA (1977) Planar spin imaging by NMR. *J. Magn. Reson.* 27:101–119.
32. Ernst RR, Anderson WA (1966) Application of Fourier transform spectroscopy to magnetic resonance. *Rev. Sci. Instrum.* 37:93.
33. Kumar A, Welte D, Ernst RR (1975) NMR Fourier zeugmatography. *J. Magn. Reson.* 18:69–83.
34. Edelstein WA, Hutchison JMS, Johnson G, Redpath T (1980) Spin warp NMR imaging and applications to human whole-body imaging. *Phys. Med. Biol.* 25:751–756.
35. OECD (2013) Magnetic resonance imaging units, total, Health: Key tables from OECD, No. 36. doi:10.1787/magresimaging-table-2013-2-en.
36. OECD (2013) Magnetic resonance imaging (MRI) exams, total, Health: Key tables from OECD, No. 46. doi:10.1787/mri-exam-total-table-2013-2-en.
37. Lustig M, Donoho D, Pauly JM (2007) Sparse MRI: The application of compressed sensing for rapid MR imaging. *Magn. Reson. Med.* 58:1182–1195.
38. Sodickson DK, Manning WJ (1997) Simultaneous acquisition of spatial harmonics (SMASH): Fast imaging with radiofrequency coil arrays. *Magn. Reson. Med.* 38:591–603.
39. Pruessmann KP, Weiger M, Scheidegger MB, Boesiger P (1999) SENSE: Sensitivity encoding for fast MRI. *Magn. Reson. Med.* 42:952–962.
40. Kastler A (1950) Quelques suggestions concernant la production optique et la détection optique d'une inégalité de population des niveaux de quantification spatiale des atomes—Application à l'expérience de Stern et Gerlach et à la résonance magnétique. *J. Phys. Radium.* 11:255–265.
41. Colegrove FD, Schearer LD, Walters GK (1963) Polarization of He³ gas by optical pumping. *Phys. Rev.* 132:2561–2572.
42. Happer W (1972) Optical pumping. *Rev. Mod. Phys.* 44:169–249.
43. Abragam A, Goldman M (1978) Principles of dynamic nuclear polarisation. *Rep. Prog. Phys.* 41:395.
44. Natterer J, Bargon J (1997) Parahydrogen induced polarization. *Prog. Nucl. Magn. Reson. Spectrosc.* 31:293–315.
45. Ardenkjaer-Larsen JH, Fridlund B, Gram A, Hansson G et al. (2003) Increase in signal-to-noise ratio of >10,000 times in liquid-state NMR. *PNAS* 100:10158–10163.
46. Mansson S, Johansson E, Magnusson P, Chai CM et al. (2006) C-13 imaging—A new diagnostic platform. *Eur. Radiol.* 16:57–67.
47. Ackerman JJH (2013) Magnetic resonance imaging: Silicon for the future. *Nat. Nanotechnol.* 8:313–315.
48. Cassidy MC, Chan HR, Ross BD, Bhattacharya PK et al. (2013) In vivo magnetic resonance imaging of hyperpolarized silicon particles. *Nat. Nanotechnol.* 8:363–368.
49. Fogarty HA, Berthault P, Brotin T, Huber G et al. (2007) A cryptophane core optimized for xenon encapsulation. *J. Am. Chem. Soc.* 129:10332.
50. Klippel S, Doepfert J, Jayapaul J, Kunth M et al. (2014) Cell tracking with caged xenon: Using cryptophanes as MRI reporters upon cellular internalization. *Angew. Chem. Int. Ed.* 53:493–496.
51. Young IR (2004) Significant events in the development of MRI. *J. Magn. Reson. Imaging* 20:183–186.
52. Jeener J (2000) Equivalence between the “classical” and the “Warren” approaches for the effects of long range dipolar couplings in liquid nuclear magnetic resonance. *J. Chem. Phys.* 112:5091–5094.
53. Hoult DI, Ginsberg NS (2001) The quantum origins of the free induction decay signal and spin noise. *J. Magn. Reson.* 148:182–199.
54. Hoult DI (2009) The origins and present status of the radio wave controversy in NMR. *Concepts Magn. Reson.* A 34A:193–216.
55. Bloembergen N, Purcell EM, Pound RV (1948) Relaxation effects in nuclear magnetic resonance absorption. *Phys. Rev.* 73:679–712.
56. Murali N, Krishnan V (2003) A primer for nuclear magnetic relaxation in liquids. *Concepts Magn. Reson.* 17A:86–116.
57. Torrey HC (1956) Bloch equations with diffusion terms. *Phys. Rev.* 104:563–565.
58. Turner R (1993) Gradient coil design: A review of methods. *Magn. Reson. Imaging* 11:903–920.
59. Hidalgo-Tobon SS (2010) Theory of gradient coil design methods for magnetic resonance imaging. *Concepts Magn. Reson.* A 36A:223–242.
60. Mispelter J, Lupu M, Briguet A (2006) *NMR Probeheads for Biophysical and Biomedical Experiments*. Imperial College Press, London.
61. Vaughan JT, Griffiths JR (eds.) (2012) *RF Coils for MRI*. John Wiley & Sons, Chichester, England.
62. Hoult DI (2000) The principle of reciprocity in signal strength calculations: A mathematical guide. *Concepts Magn. Reson.* 12:173–187.
63. Cagnac B, Brossel J, Kastler A (1958) Résonance magnétique nucléaire du mercure Hg-201 aligné par pompage optique. *C.R. Acad. Sci.* 246:1827–1830.
64. Kastler A (1957) Optical methods of atomic orientation and of magnetic resonance. *J. Opt. Soc. Am.* 47:460–465.
65. Hoult DI, Lauterbur PC (1979) Sensitivity of the zeugmatographic experiment involving human samples. *J. Magn. Reson.* 34:425–433.

66. Hayden ME, Bidinosti CP, Chapple EM (2012) Specific absorption rates and signal-to-noise ratio limitations for MRI in very-low magnetic fields. *Concepts Magn. Reson. A* 40A:281–294.
67. Bittoun J, Querleux B, Darrasse L (2006) Advances in MR imaging of the skin. *NMR Biomed.* 19:723–730.
68. Mossle M, Myers WR, Lee SK, Kelso N et al. (2005) SQUID-detected in vivo MRI at microtesla magnetic fields. *IEEE Trans. Appl. Supercond.* 15:757–760. (2004 *Applied Superconductivity Conference*, Jacksonville, FL, October 3–8, 2004.)
69. Budker D, Romalis M (2007) Optical magnetometry. *Nat. Phys.* 3:227–234.
70. Mamin HJ, Poggio M, Degen CL, Rugar D (2007) Nuclear magnetic resonance imaging with 90-nm resolution. *Nat. Nanotechnol.* 2:301–306.
71. Homann H, Boernert P, Eggert H, Nehrke K et al. (2011) Toward individualized SAR models and in vivo validation. *Magn. Reson. Med.* 66:1767–1776.
72. Wolf S, Diehl D, Gebhardt M, Mallow J et al. (2013) SAR Simulations for high-field MRI: How much detail, effort, and accuracy is needed? *Magn. Reson. Med.* 69:1157–1168.
73. International Electrotechnical Commission (2010) Medical electrical equipment part 2-33: Particular requirements for the basic safety and essential performance of magnetic resonance equipment for medical diagnosis, Geneva, International Standard IEC 60601-2-33.
74. Pauly J, Leroux P, Nishimura D, Macovski A (1991) Parameter relations for the Shinnar-Le Roux selective excitation pulse design algorithm. *IEEE Trans. Med. Imaging* 10:53–65.
75. Ljunggren S (1983) A simple graphical representation of Fourier-based imaging methods. *J. Magn. Reson.* 54:338–343.
76. Xiang QS, Henkelman RM (1993) K-space description for MR imaging of dynamic objects. *Magn. Reson. Med.* 29:422–428.
77. Hennig J (1999) K-space sampling strategies. *Eur. Radiol.* 9:1020–1031.
78. Paschal CB, Morris HD (2004) k-Space in the clinic. *J. Magn. Reson. Imaging* 19:145–159.
79. McGibney G, Smith MR, Nichols ST, Crawley A (1993) Quantitative-evaluation of several partial Fourier re-construction algorithms used in MRI. *Magn. Reson. Med.* 30:51–59.
80. Weisman ID, Bennett LH, Maxwell LR, Woods MW et al. (1972) Recognition of cancer in vivo by nuclear magnetic resonance. *Science* 178:1288–1290.

This page intentionally left blank

2

Introduction to the Basics of MRI to Introduce the Macroscopic Magnetization M

Luigi Barberini

CONTENTS

2.1	Introduction: The Basic of MRI to Introduce the Macroscopic M	29
2.2	Bloch Equations for the Macroscopic Magnetization (M) Dependences: From Protons to Echo Tissues Signals (Intrinsic MRI Parameters Fast Description: T_1 T_2 T_2^* PD)	33
2.3	MR Hardware for Sequences Production: Electronic Chain for the RF System and Gradient System.....	36
2.3.1	RF Electronic Unit.....	37
2.3.2	Gradient Electronic Unit.....	38
2.3.3	RF Pulses and Macroscopic Net Magnetization M Effects.....	39
2.3.4	Gradient Waveforms and Macroscopic Net Magnetization M Effects	40
2.4	k -Space and Complexification of the Space	42
2.5	Sequences and Contrast Control in the Imaging for MR.....	49
2.5.1	SE Sequences	52
2.5.2	GE Sequences.....	53
2.5.3	IR Sequences.....	54
2.6	Sequence Engineering as a Strategy for Developing Innovative Diagnostic Applications	55
2.6.1	Functional MRI Sequences	55
2.6.1.1	Echo-Planar Imaging (Functional MRI)	55
2.6.2	Magnetic Resonance Angiography	56
2.6.3	Flow-Dependent Angiography	57
2.6.3.1	Phase-Contrast	57
2.6.3.2	Time-of-Flight	57
2.6.4	Contrast-Enhanced Angiography.....	58
2.7	Conclusion	59
	Bibliography	59

2.1 Introduction: The Basic of MRI to Introduce the Macroscopic M

MRI is one of the most important technical tools for the diagnostic process developed in the recent period. Modern MRI systems provide highly detailed images of tissue in the body with fast scan, reducing the examination time for the best comfort of the patient. With the MRI, it is possible to study the human body and the internal organs producing high-quality images without the use of ionizing radiation. This imaging technique is based on the resonance physics phenomenon that practically is the way to exchange energy between

physical systems at particular frequencies, which is the characteristic, in some way, of these systems; these frequencies are called *natural frequencies* of the system. Under these conditions, energy flows from one system to the other with none or little dumping and can be efficiently stored by the living matter under investigation. The relaxation phenomena of the living matter can give much information to be used for the image construction.

The resonance phenomenon can occur between mechanical waves and vibrational physical systems like diapason, for example, and at the level of electrons and nuclear spin interacting with electromagnetic (EM) microwaves and radio waves.

In order to acquire information about the structural and functional properties of the molecules in biofluids, tissues, and organs in living systems, the nuclear magnetic resonance (NMR) technique can be used. Such information can be acquired from *in vitro* samples, for example, liquid mixtures of molecules contained in particular tubes, from samples in the solid state with appropriate coils (or probes); furthermore, molecular properties can also be acquired directly on the living tissues and organs (*in vivo*) in order to obtain morphological and functional images of tissues and organs. Several kinds of nuclei have the possibility to get coupled to the EM field: they are the ones without zero spin values. For these systems, characteristic frequencies of resonance are generated putting the matter into a static magnetic field. The most important nucleus in the NMR is the proton, with the nucleus of the hydrogen usually indicated by ^1H . ^1H has the spin value $S = 1/2$; hydrogen atoms have an inherent magnetic moment as a result of their nuclear spin. When placed in a strong magnetic field, the magnetic moments of these hydrogen nuclei tend to align along the B_0 direction with a motion of precession defined by the Larmor frequency; part of these spins align with a precession motion along the same direction of B_0 and part align in the opposite direction creating a two-level energy system (Figure 2.1).

This balance, maintained by the thermal agitation, generates a net magnetization because a little amount of spins prefers to stay in the lower energetic state; the net magnetization is the sum over all spins of the microscopic magnetic moments. We can represent the precession motion in a particular reference frame, a system rotating at the same precession of the spin and magnetization. In this reference frame, \mathbf{M} is a vector aligned along B_0 (Figure 2.2).

For the physics of nuclear spins, we will return later on the references systems; for the moment, we can consider the one in which spins are aligned to B_0 .

For the *bare* hydrogen, the characteristic frequency of precession defined as the Larmor angular velocity, at the 1 T magnetic static field is

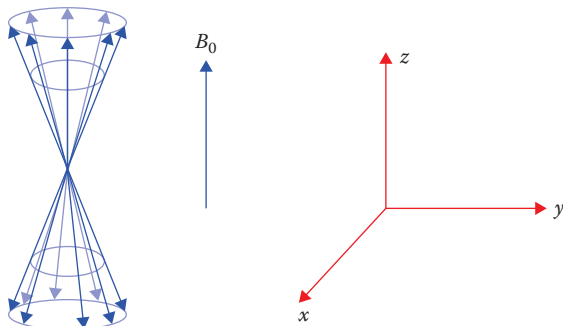


FIGURE 2.1
Spins motion and directions of reference.

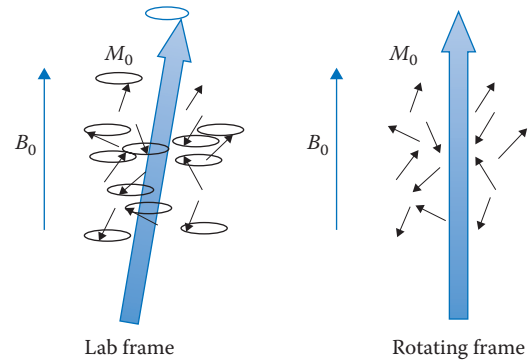


FIGURE 2.2
Spins behavior and reference frames.

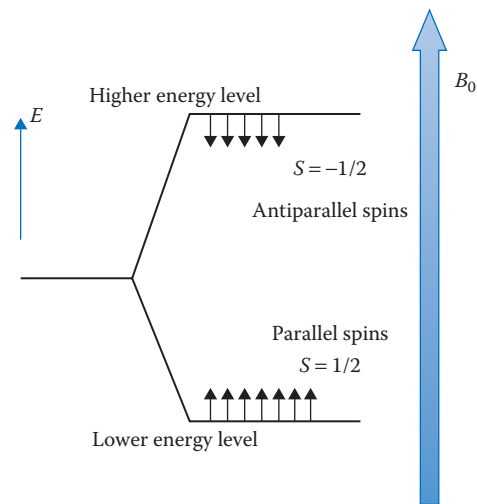


FIGURE 2.3
Zeeman levels and spins directions in space.

$$\omega = \frac{-e\hbar}{2m} B_0 \quad (2.1)$$

In this way, protons can exchange energy with EM wave through the coupling of the nuclear magnetic moment and the magnetic component of the EM wave; the exchanged energy corresponds to the transition of the spins from the lower energy level to the higher level (Figure 2.3).

This energy corresponds, in the EM spectrum region, to radiofrequency (RF) waves (Figure 2.4).

So, the EM field can be coupled to the biological matter protons at the *characteristic* frequency of the Larmor precession of the net magnetization M around the static magnetic field B_0 . With the term *characteristic*, we indicate that it depends on the nucleus considered, proton, carbon, phosphorus (all nuclei with not null magnetic moment) and, most of all, on the applied magnetic field.

From the macroscopic point of view, the physical entity of interest in MRI is the magnetization vector \mathbf{M} and its components M_P and M_I .

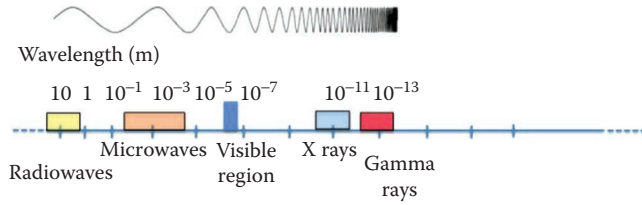


FIGURE 2.4
Electromagnetic spectrum.

The magnetization M_p (sometimes also indicated by the symbol M_0 to emphasize the relation with B_0) of the substance is the average of all the spin magnetic moments of each atom μ_i . We write

$$M_p = \sum \mu_i$$

which is pointed along of the z -axis.

The dynamic of the \mathbf{M} vector is totally described by the phenomenological Bloch equations. In order to derive these equations, we have to consider the physical status of the spins. Thermal equilibrium defines, in the interaction spins-EM field, the distribution of the hydrogen spins on the two energetic levels as described the Maxwell-Boltzmann distribution:

$$\frac{N_1}{N_2} = \mu_0 B_0 e^{-(\Delta E/RT)} \quad (2.2)$$

The projection of this vector along the z direction defines the M_p or M_0 . In order to produce a detectable time-varying signal to process by means of the MRI system, it is mandatory to rotate the M_0 vector in the plane orthogonal to z . Proper stimulation by means of a resonant magnetic, or an RF field at the resonant frequency of the hydrogen nuclei, can force the magnetic moments of the nuclei to partially, or completely, tip into a plane perpendicular to the applied field. The angle of this rotation is called the *flip angle* and indicated by FA; this rotation is strictly related to the temporal duration of the pulse. This is the excitation process of the biological and living matter at the resonance condition or phase concordance between radiation and spins. These RF pulses are indicated with the $B_1(t)$ expression after the B_0 symbol for the static magnetic field. The precession motion complicates the real motion of the \mathbf{M} in the laboratory frame (Figure 2.5). But the dynamic of the \mathbf{M} vector, when an RF pulse is acting on the spins (exchange of energy in resonant mode), can be decomposed as a rotation of \mathbf{M} around the z -axis and a change in the angle between z and \mathbf{M} (FA), called *nutations*. This composite motion can be represented by a conic helix trajectory of the \mathbf{M} vector in the lab frame with parametric equations (Figure 2.6):

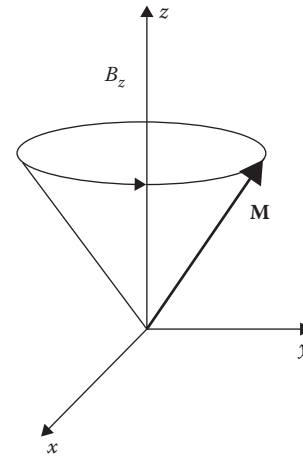


FIGURE 2.5
Precession of the \mathbf{M} vector in the lab system.

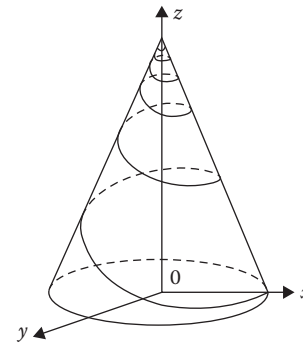


FIGURE 2.6
Conic helix trajectory of \mathbf{M} vector in the laboratory frame.

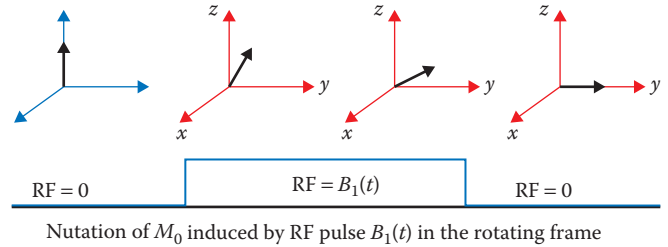


FIGURE 2.7
Effects of RF pulse P90 for the \mathbf{M} orientation.

$$\begin{aligned} x(t) &= (R_0(1-t) + R_1)\sin(N2\pi t) \\ y(t) &= (R_0(1-t) + R_1)\cos(N2\pi t) \\ z(t) &= Ht \end{aligned} \quad (2.3)$$

The motion of \mathbf{M} toward the x - y plane is the one of interest for the description of the transversal magnetization generation (Figure 2.7).

So, the hydrogen atoms, which are abundant in tissue, are placed in a strong magnetic field B_0 , and then excited by a resonant magnetic excitation pulse $B_1(t)$ applied as long as needed to rotate magnetization; after the $B_1(t)$ field is switched off, the spin relaxation process starts, and the net magnetization laying in the x - y plane begins to decay due to the local spin-spin interaction. Meanwhile, due to the spin-lattice interaction, there is a loss of energy toward the bulk of matter related to the tissue nature and to the physical state of the matter in the tissue, and the longitudinal magnetization begins to rise. Spin-spin and spin-lattice interactions are different phenomena. Parameters of these phenomena are different: they contribute to the loss of magnetization along the x - y plane and to the recovery of the M_0 magnetization, and they depend on the tissue nature and on its physical status. The magnetization M_P (sometimes also indicated with the symbol M_0 to emphasize the relation with B_0) of the substance is the average of all the spin magnetic moments of each atom μ_i . We write

$$M_{\parallel} = \sum \mu_i$$

which is pointed along the z -axis.

The field $B_1(t)$ exerts a torque force on the vector M_0 leading it to the y -axis (Figure 2.8).

Then, the relaxation phenomena give back the energy absorbed from EM wave, transporting the RF pulse to the external environment with all the information about the location and the physical status of the nuclear spins. But the relaxation is a double process: spins lose the coherence, and the summation of the spins generating the M_{\perp} magnetization decreases (Figure 2.9).

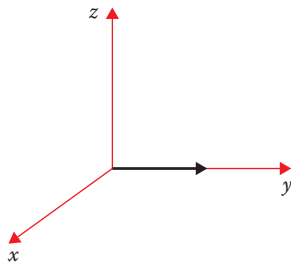


FIGURE 2.8
Transversal magnetization M after P90 RF pulse.

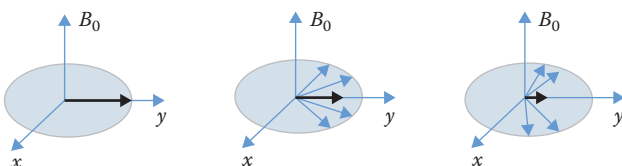


FIGURE 2.9
Dephasing of nuclear spins.

At the same time, but with different time constant, the M_P starts to recover toward the initial value M_0 .

Meanwhile, the longitudinal magnetization begins the recovery process, but with a different temporal constant T_1 , due to the interaction of the spins with the bulk of tissues (Figure 2.10).

In the frame laboratory, the magnetization vector \mathbf{M} rotates in the x - y plane and in the z - y plane. Rotational motion in the x - y plane is not related to an energy exchange, so we can imagine a frame transformation to put in rotation the xyz frame around the z -axis to hide this behavior of $B_1(t)$. This is called the *rotating frame*. In the rotating frame, the magnetization vector \mathbf{M} rotates only in the z - y plane without precession. The properties of interest of the living matter are resumed by the macroscopic magnetization \bar{M} and its dynamic; the information used to realize images with structural and functional informative content is derived by the dynamic of the \bar{M} vector equations. \bar{M} is the net magnetic moment per volume unit (a vector quantity) of a sample in a given region, considered as the integrated effect of all the individual microscopic nuclear magnetic moments μ_i . \bar{M} will be the actor of our play in MRI.

The microscopic magnetic moments and the macroscopic magnetization are *vectors*, entities endowed by intensity, line, and direction of action and phase. As usual, in order to work with these entities, it is better to define the reference work system used: the natural frame reference for MRI study is the *laboratory* system where a left-hand system is defined by the z direction along the B_0 field direction and x and y are oriented as shown in Figure 2.11.

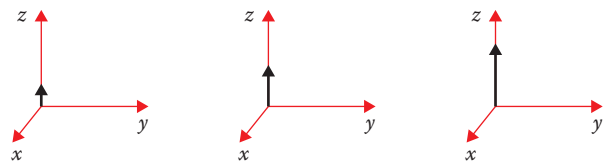


FIGURE 2.10
Longitudinal magnetization recovery. Please note that in this representation, transversal magnetization is not reported; in this way, we highlight that longitudinal and transversal magnetization vary with different physical phenomena and different time constants.

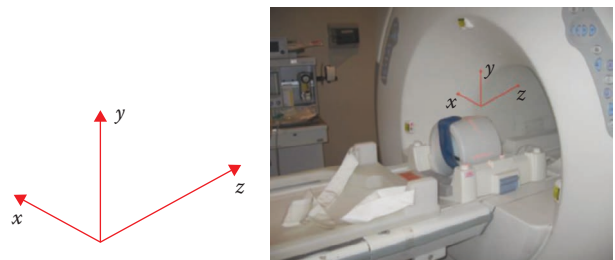


FIGURE 2.11
Spatial orientation in MRI.

In this frame, as mentioned before, the motion of \mathbf{M} is complicated by the precession phenomenon. The same complication arises considering the excitation of the magnetization with the RF pulse. The equation for the \mathbf{M} dynamic, in the laboratory reference frame, is

$$\left(\frac{d\mathbf{M}}{dt} \right)_{\text{lab}}^i = \overset{r}{\mathbf{M}} \times (\omega \overset{r}{z}) \quad (2.4)$$

The helical motion of the \mathbf{M} vector in the lab frame can be simplified applying the transformation group of rotation. If we consider that it is possible to define a new reference frame rotating in the x - y plane with angular speed ω , we can define the previous equation in the rotating frame, and it is possible to demonstrate

$$\left(\frac{d\mathbf{M}}{dt} \right)_{\text{rotating}}^i = (\omega - \omega_0) \overset{r}{\mathbf{M}} \times \overset{r}{z} \quad (2.5)$$

If the rotation speed is equal to the Larmor frequency, then temporal derivative is null and \mathbf{M} becomes a stationary vector. The same transformation can be applied to the RF pulse (in order to produce the alignment of the magnetization in the x - y plane), and simplifications of the same level can be introduced for the RF pulse description. The dynamic of the RF pulse $B_1(t)$ in the lab system is

$$\vec{B}_1(t) = \hat{x}B_1(t)\cos(\omega t) - \hat{y}B_1(t)\sin(\omega t) \quad (2.6)$$

and in the rotating frame is

$$\vec{B}_1(t) = \hat{x}B_1(t) \quad (2.7)$$

The rotating frame introduces a great amount of simplification in equations and formulas, and it is useful for the discussion about the relaxation process of the \mathbf{M} net magnetization.

The most important phenomena for the use of MR in the investigation about the matter structure are the relaxation mechanisms of \mathbf{M} that happens after the truncation of the EM (no-ionizing) fields exciting the living tissues. Generally speaking, living tissues and molecules should be transparent to the EM window of the RF and this part of the radiation spectra should not be able to exchange energy with the molecules. But using a static magnetic field, molecules are able to exchange energy with the EM field in the region of the RF and tissues become opaque to RF in different ways related to the status of the molecule bulk. In this way, it becomes possible to excite selectively the living matter and to record the relaxation MRI signal, which brings a lot of information about the molecules status.

The relaxation of the macroscopic magnetization is a dynamic phenomenon. This dynamic is different for each kind of tissue, and it is related to the bulk physical status, the molecular environment, in addition to the spin parameters. By using the RF pulses and a slow controlled linear variation of the static magnetic field, it is possible to *manipulate* the status of the single nuclear spin and the level of coherence between each other; from the macroscopic point of view, we can manipulate the \mathbf{M} dynamic in the excitation and relaxation period. It is important to highlight that the possibility to *manipulate* the signals in imaging to produce images of interest has its maximum expression in the MRI; only the MRI, with the great amount of *free parameters* characterizing the phenomenon gives to researchers the possibility of acting on tissues and receiving different signals with different information.

2.2 Bloch Equations for the Macroscopic Magnetization (M) Dependences: From Protons to Echo Tissues Signals (Intrinsic MRI Parameters Fast Description: T_1 T_2 T_2^* PD)

Usually, in MRI we do not deal with microscopic entities as the spins: the vector used to describe the behavior of the biological matter in the MRI scanner is the net macroscopic magnetization \mathbf{M} . As previously reported, at the thermal equilibrium, \mathbf{M} is a vector with a precession motion around the B_0 field (Figure 2.12).

We introduce a perturbation of the thermodynamic equilibrium with the transmission of RF pulses for the excitation of tissue's nuclei. As previously represented,

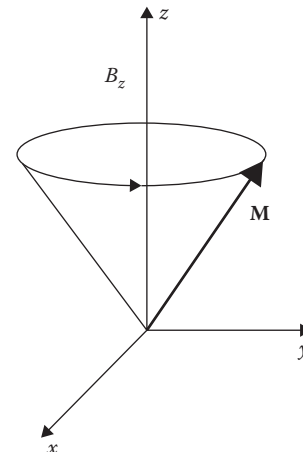


FIGURE 2.12 \mathbf{M} vector in the lab system.

the RF pulses are labeled in the MRI theory as $B_1(t)$ in order to emphasize that it is a magnetic field time variant that is interacting with a nuclear magnetic spin. As previously reported, RF pulses are EM waves in the RF range of the spectrum.

During this energy transfer, part of the M_P is transformed in M_{\perp} . M_P is the result of the N_1/N_2 fraction of spin, orthogonally orientated to B_0 . Spins are in coherent motion due to the $B_1(t)$ perturbation: Zeeman levels are coherent energetic states. After the end of the perturbation, that is, after the RF pulse is switched off, the energy transfer from the EM wave to spins is interrupted, thermal agitation of the spins starts to destroy the coherence between spins, and this introduces a decay of the orthogonal component of the \mathbf{M} . At the same time, part of the M_{\perp} can be recovered in the z direction and the longitudinal magnetization starts to arise in this direction. Energy and coherence losing are relaxation phenomena. The most important parameters of these phenomena are PD, proton density; T_2 , time constant for the molecule–molecule interaction describing the orthogonal magnetization recover; and T_1 , time constant for the molecule–bulk interaction, describing the longitudinal magnetization recover. Furthermore, it is possible to calculate the effects of local decreasing of the T_2 values of tissues: in fact, the blood oxygenation level dependent (BOLD) mechanism realizes the explanation of a faster decrease of the local T_2 (called T_2^*) in tissue due to the activation of the neurons located in the brain area devoted to a task execution. Default brain activity leaves other areas in the default state of activation with a usual signal of M_{\perp} decreasing with the usual T_2 time constant. These properties of interest can be all used in the construction of images with morphological and functional significance.

The molecule–molecule interaction is studied along the B_0 field direction; meanwhile, the molecule–bulk interaction is better studied in the x – y plane orthogonal to the direction of the B_0 field, that is, the z direction. So pulses must be used to selectively orientate the macroscopic magnetization. To produce an image with the MRI system, we must first stimulate the hydrogen nuclei in a specific region of the body. Excited nuclei, after the end of perturbation, radiate in the space a signal in the form of the EM wave until the energy absorbed during the excitation phase is completely released; this is the process called *relaxation*. Relaxation produces the NMR signal used to create images of differentiated tissue types and to produce images for MRI systems. So, initial MR signal amplitudes are directly related to hydrogen nuclei density in the tissue being imaged. Primarily, it will be notable for the concentration of mobile hydrogen atoms within a sample of tissue; the concentration of hydrogen atoms in water molecules or in some groups of fat molecules within tissues is defined by the term

proton density (PD). Then, the relaxation process of the magnetization determines the evolution of the MRI signal.

The passage from the microscopic to the macroscopic scale can be described by the summation:

$$M = \sum_i \mu_i \quad (2.8)$$

So, from the time variation of each single spin magnetic momentum expressed as

$$\frac{d\mu}{dt} = \mu \times \gamma \mathbf{B} \quad (2.9)$$

we arrive to the \mathbf{M} vector dynamic after the summation of μ over the volume; this gives the following equation of macroscopic magnetization dynamic:

$$\frac{d\mathbf{M}}{dt} = \mathbf{M} \times \gamma \mathbf{B} \quad (2.10)$$

as previously reported as Equation 2.4, that is, \mathbf{M} precession along \mathbf{B} with a frequency equal to $\omega = \gamma B$.

Vector \mathbf{M} , and its temporal derivatives, can be represented by the three vector components in the lab frame. In order to relate the time evolution of magnetization to the external magnetic fields and to the relaxation times, Bloch equations can be used:

$$\begin{aligned} \frac{dM_x(t)}{dt} &= \gamma(M(t) \times B(t))_x - \frac{M_x(t)}{T_2} \\ \frac{dM_y(t)}{dt} &= \gamma(M(t) \times B(t))_y - \frac{M_y(t)}{T_2} \\ \frac{dM_z(t)}{dt} &= \gamma(M(t) \times B(t))_z - \frac{M_z(t) - M_0}{T_1} \end{aligned} \quad (2.11)$$

The component along the z direction is called *longitudinal magnetization* $M_0 = M_{||}$. The other two components can be represented as a vectorial sum lying in the x – y plane orthogonal to the z direction: for this reason, it is represented as M_{\perp} .

The phenomenological Bloch equations explain the evolution of the magnetization moment during its precession. The magnetic field $B_1(t)$ is time dependent, the same as the magnetization moment $M(t)$. The important phenomenon related to the evolution of the magnetization vector is the relaxation following the precession induced by the excitation. As previously reported, two different relaxation processes occur: the longitudinal relaxation and the transverse relaxation.

As illustrated in Figures 2.9 and 2.10, interactions between spins result in the destruction of the coherence phase between spins, and in this way, the sum

over the spin is incoherent and tends to decay toward zero. Meanwhile, the energy absorbed by excitation is released as a result of the energy exchanges between spins and bulk, or lattice: spins excited to the upper level come back to the lower restoring the $M_0 = M_{||}$ macroscopic magnetization. It is really interesting to note that time constants of these processes are quite different because of different physics processes underlying the phenomena.

Typically, the solution of the differential equation with the form of Equation 2.2 has an exponential form; the dynamics of the $M_{||}$, M_{\perp} vectors are different and their solutions will have different temporal constants. The typical time evolution constant for the $M_{||}$ is labeled T_1 and the M_{\perp} vector has a temporal constant labeled T_2 . The graphical evolution of the two vectors is shown in Figures 2.13 and 2.14.

The pure T_2 time constant is the observed decay parameter of the FID because of the loss of phase coherence among spins due to the spin-spin interaction for the spin thermal agitation. But commonly, the coherence loss is due to a combination of the static magnetic field in homogeneity and spin-spin transverse relaxation, with the result of more rapid loss in the transverse magnetization and MRI signal decay:

$$\frac{1}{T_2^*} = \frac{1}{T_2} + \Delta\omega = \frac{1}{T_2} + \gamma\Delta B$$

T_2^* depends on the local magnetic field nonuniformities ΔB ; due to this phenomenon, the protons precess at slightly different frequencies. The T_2^* effect causes a faster loss in spins coherence and transverse magnetization, and the T_2^* time results lower than the T_2 .

In order to control the magnetization and weighting the images in PD, T_1 , T_2 , and T_2^* , defined as the intrinsic MRI parameters, we need to submit the matter to a proper sequence of RF pulses and gradient waveforms. The parameters used to describe the temporal properties of these sequences are called *extrinsic parameters* for

the contrast control: the number of pulses, the intensity, the timing, the power of the pulses, and the gradient shape and length allow the sequence designers to realize a proper project of sequence to act on the magnetization in order to produce the proper contrast (Figure 2.15).

Before describing these parameters, we have to introduce and discuss the electronic chain components for the production and control of the RF pulses and gradients.

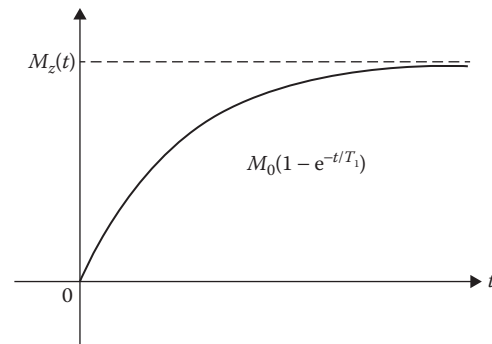


FIGURE 2.13 Longitudinal relaxation.

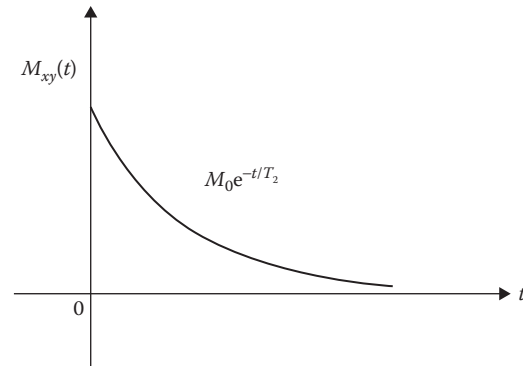


FIGURE 2.14 Transversal relaxation.

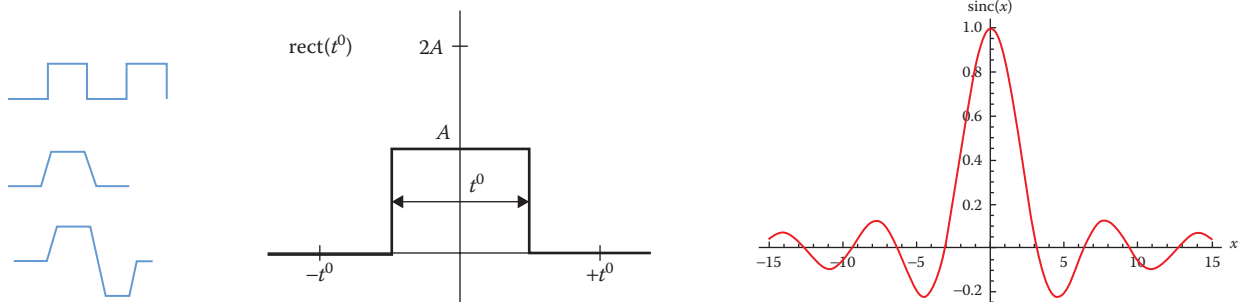


FIGURE 2.15 Principal gradient and RF pulses shapes.

2.3 MR Hardware for Sequences

Production: Electronic Chain for the RF System and Gradient System

Among the main hardware elements in the MRI scanner systems that we can consider for the sequences description, there are static magnetic field and shimming coils, gradient magnetic field coils, RF receiver–transmitter coils, pulse waveform generator and timing, gradient waveform generator and timing, frequency synthesizer, amplifiers and analog-to-digital—digital-to-analog (ADC–DAC) converters, power unit, and the image signal processing unit.

A schematic representation of a scanner is shown in Figure 2.16.

In order to have all the elements for the general comprehension of the MRI, it is mandatory to have a look at some important concepts related to the electronic components listed before and related to some important operations performed on the signals in MRI. Signals to and from scanner must be digitalized, processed, and stored. Electronic circuits at very high speeds perform part of these operations. This is the reason why companies involved in the MRI scanner market spend a lot of money in the electronic development for the new systems. The digital *treatment* of a signal is characterized by some important issues: the analogical signal must be measured with appropriate transducers (coils) functioning as *receivers* (or *transmitters* when they have to put in resonance the nuclear spin); in the receiving process, analogical signals must be sampled in order to allow the

storage on the electronic memory for the mathematical treatment. At this stage, we tackle the problem of the amplification of the signal: in some cases, the intensity of the electric signal emitted by transducers could be very low and it is necessary to provide *amplification* to this signal in order to acquire, store, and process the information in a proper way, avoiding storing *noise*. The electronic components devoted to this operation are the amplifiers. After amplification, the ADC provides the conversion of that signal in a digital form easily managed and stored by a computer. We also need to operate the inverse operation and convert a digital signal generated by the MRI system in the analogical format. For this operation, a DAC circuit is implemented in the electronic cabinets of the MRI system.

The analog–digital conversion is accomplished through two basic steps: sampling and quantization. Given a suitably amplified analogical signal, the sampling process consists in measuring that signal for a number of times per second, storing the measured values instead of the signal itself (Figure 2.17).

The signal is measured at regular intervals with a frequency-defined sampling frequency, which must be twice as much as the max frequency in the signal in order to avoid the lost of information about the signal (Nyquist theorem). In terms of time, the interval between two sampling is called *dwell time* Δt , and it represents the inverse of the full readout bandwidth. The readout bandwidth is the range of spin frequency in all the field of views (FOVs). Quantization is the process of mapping a large set of input values to a smaller and countable set, such as rounding values to some unit of

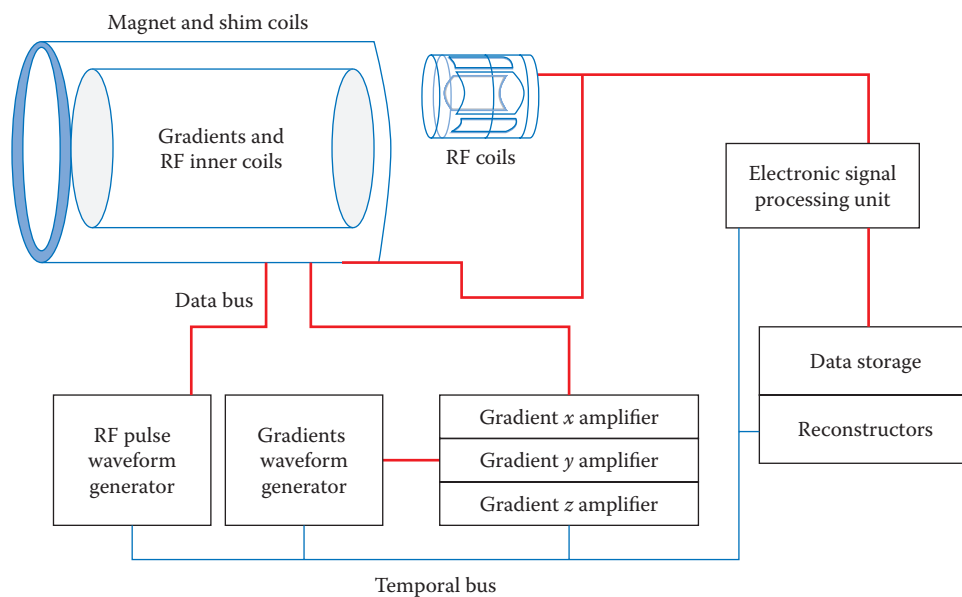


FIGURE 2.16
Flowchart of an MRI scanner.

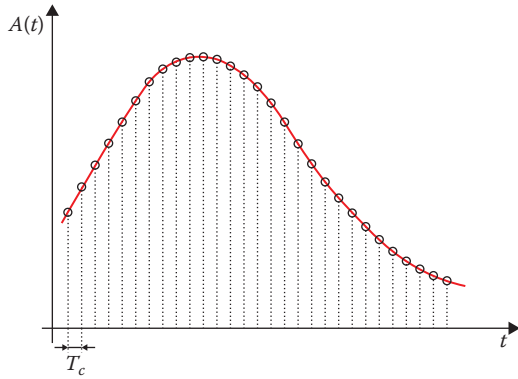


FIGURE 2.17
Sampling of the analogical signals.

precision. The difference between the actual analogical value and the quantized digital value is called the *quantization error*.

The signal coming out from transducers may contain variations related to the information of interest and some variations that are only *noise*. So, there is the need to filter the signal as better as possible in order to increase the part of the signal of interest and drastically reduce the noise. This is called the *digital signal processing*. Digital filters can be designed to operate the signal-to-noise ratio (SNR) and as much as possible to improve the quality of the image for the visual diagnostic process or for the computer-aided diagnosis (CAD).

2.3.1 RF Electronic Unit

The EM waves used in the NMR and MRI technologies are in the EM spectral region of the RFs. This wide range is named in such a way because some radio

transmissions are in this region. The usual radio stations for the music and news operating in the so-called frequency modulation are in the MHz range, or thousands of MHz. So the electronic terminology for the radio transmissions is frequently used to describe the process and equipment in MR. In fact, the operative process to excite nuclei in the matter and to recoil the signals echoing from the matter is an RF transmission and receiving process (Figure 2.18).

So, there is a part of the scanner, named transmitter, used to generate the RF pulses necessary to exchange energy with the hydrogen nuclei. The range of frequencies in the transmit excitation pulse and the magnitude of the gradient field determine the width of the image slice. A typical transmit pulse will produce an output signal with a relatively narrow bandwidth, about ± 1 kHz.

The shape of excitation wave in the time domain usually requires particular properties of the signal; for example, some RF pulses are used to prepare the magnetization for a selective excitation in order to saturate the energy level of some kind of biological matter to exclude it from the generation of the signal in the de-excitation of the matter. As reported in Section 2.3.3, these waveforms are usually digitally generated at the baseband and then up-converted by a mixer to the appropriate central frequency.

In electronics, a mixer or a frequency mixer is a non-linear electrical circuit that creates new frequencies from two signals applied to it (Figure 2.19).

Traditional transmitter circuitries require relatively low-speed DACs to generate the baseband waveform, as the bandwidth of this signal is relatively small. But with recent advances in DAC technology, other potential transmitter architectures are achievable. Very high speed, high-resolution DACs can be used for the direct RF

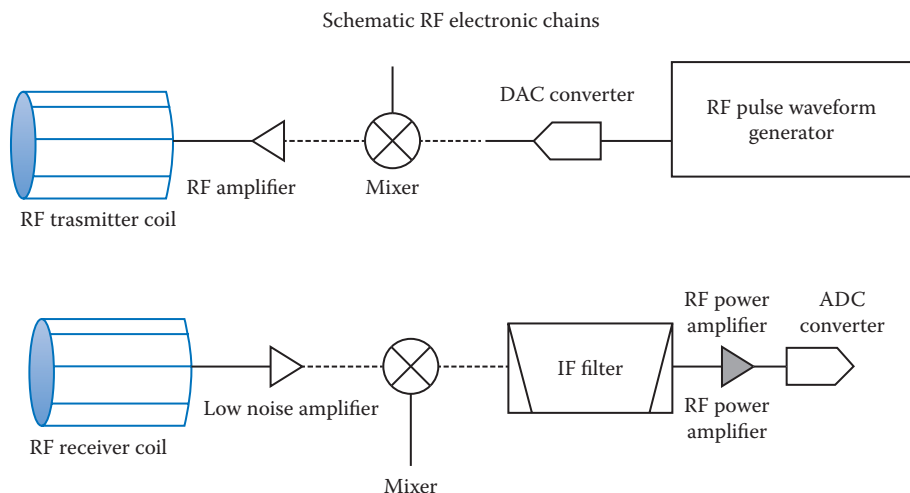


FIGURE 2.18
Electronic chains in MRI.

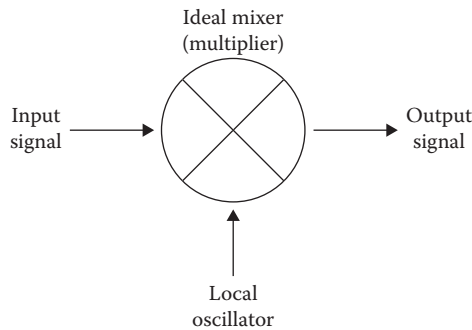


FIGURE 2.19
Ideal mixer of RF signals.

generation of transmit pulses up to 300 MHz. Therefore, waveform generation and up conversion over a broad band of frequencies can be entirely accomplished in the digital domain.

The biological matter excited by temporary RF pulses starts a rebalance process to emit the acquired energy, and this energy flows from the matter to the receiving circuit in the scanner.

An RF receiver is used to process the signals from the receiver coils. Recent MRI scanners have eight and more receiving channels to process the signals from multiple coils. The signals range from approximately 1 to 300 MHz, with the frequency range highly dependent on the applied-static magnetic field strength. The bandwidth of the received signal is small, typically less than 20 kHz, and is dependent on the magnitude of the gradient field. A traditional MRI receiver configuration has a low-noise amplifier (LNA) followed by a mixer. The mixer mixes the signal of interest to a low frequency for conversion by a high-resolution, low-speed, 12–32-bit ADC. In this receiver architecture, the ADCs used have relatively low sampling rates, below 1 MHz. Because of the low-bandwidth requirements, ADCs with higher sampling rates (1–5 MHz) can be used to convert multiple channels by means of the time multiplexing of the receiving channels through an analogical multiplexer into a single ADC.

Again, with the development of higher-performance ADCs, novel receiver architectures are now possible. High-resolution high-input bandwidth, 12–32-bit ADCs with samples rates up to 100 MHz can also be used for the direct sampling of the signals, hence eliminating the need for analogical mixers in the receive chain.

2.3.2 Gradient Electronic Unit

After the basic description of the electronics used to realize the RF pulses, we can now discuss the properties of the pulses. These properties are related to the magnetization modulation for the contrast control in the MRI. As previously mentioned, the MRI system stimulates hydrogen nuclei in a specific plane selected as slice in the body, and then determines the location of those nuclei within that plane as they relax to their ground state. These two tasks are realized using gradient coils with suitable shapes localized in the magnet. These coils, controlled by a chain of electronics devices, cause the magnetic field within a localized area to vary linearly as a function of spatial location (Figure 2.20).

As a result, the resonant frequencies of the hydrogen nuclei are spatially dependent within the gradient range variation, and consequently, by varying the frequency of the excitation pulses, it is possible to control the area to be stimulated. After the interruption of the excitation processes, the location of the stimulated nuclei precessing back to their ground state, can be determined by the emitted resonant RF and phase information.

An MRI system has gradient coils acting on the three axes X , Y , and Z . In a block diagram of the electronic chain for the gradient system, there is a control unit called the *waveform generator*, used to create a time-controlled waveform. This digital signal is sent to a DAC unit and then amplified, and directed to the proper segment of the gradient coil system.

To achieve adequate image quality and frame rates, the gradient coils in the MRI imaging system must rapidly change the strong static magnetic field in the

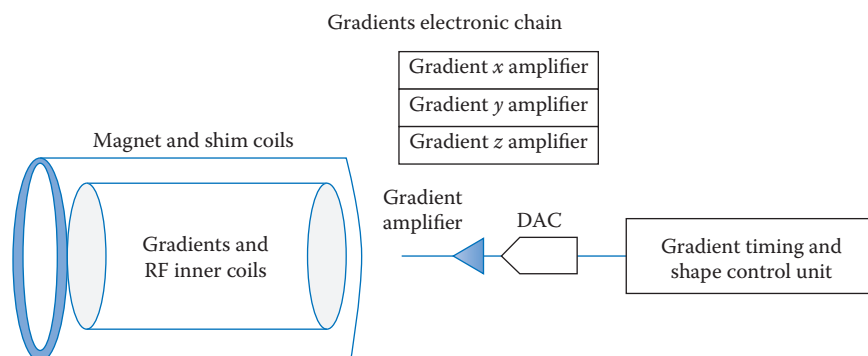


FIGURE 2.20
Schematic representation of the electronic chain for the gradients systems.

area of interest. A power electronic supply unit is used to drive the gradient coils. These electronic units operate at high voltage (up to few kilovolts) and high current (several amperes). In addition to the high power requirements, low noise and stability of the gradients are really important because any ripple in the coil current causes noise in the subsequent RF pickup. That noise directly affects the integrity of the images.

2.3.3 RF Pulses and Macroscopic Net Magnetization M Effects

We can start this section explaining that the RF pulses can primarily be used to excite the magnetization, to produce the inversion of this vector, and finally to refocus the spins in order to produce coherence and macroscopic magnetization. RF pulses can also be used for a saturation of undesired signals.

In order to better understand the use of the RF pulses, we have to highlight some important aspects: the pulse shape, the functionality of the pulse related to timing and duration, and the selectivity properties in space and in the spectrum. The duration of the RF pulse is also called *pulse width* and is typically measured in seconds or milliseconds. Regarding the pulse, it is also defined as an RF bandwidth Δf , measured in hertz, as a measure of the pulse frequency content and it represents the frequency profile for spin manipulation. Another parameter that is commonly used to describe the RF pulse effects is the FA θ . The FA is usually measured in degrees, and it describes the nutation angle produced by the pulse on the magnetization M . For example, an excitation pulse that tips the longitudinal magnetization completely into the transverse plane has a FA of 90° , and it is called *P90 pulse*. The FA is related to the duration of the pulse RF.

Another important parameter for the pulse property description is the shape. Principal shapes of RF pulses are described by the functions Rect and Sinc, with different mathematical properties that we do not treat in this context.

A Rect pulse is a pulse shaped like a RECT function in the time domain, which is zero for $|t| > T$; it is also called *hard pulse* because it is time independent. On the contrary, pulses that are time variant are defined as *soft pulses*. Hard pulses can be used when no spatial or spectral selection is required and are convenient because the pulse length can be very short. Usually, hard pulses are activated without a concurrent gradient. The bandwidth of a hard pulse, however, is broad enough to affect spins with a wide range of resonant frequencies.

A Sinc pulse is a pulse shaped like a SINC function in the time domain, that is a sine x over x .

The excitation of the magnetization vector entails the rotation of this vector from the magnetic field B_0 in the

z direction to the orthogonal x - y plane. It is possible to acquire an MR signal only if the signal is produced by the x - y plane magnetization, and for this reason, all the pulse sequences have at least one excitation pulse. This kind of pulse is called P90 pulse because it moves the M_0 vector completely in the plane orthogonal to the primary z -axis, rotating M_0 to 90° . Because the duration of the pulse is related to the nutation angle, the doubling of the duration leads to the inversion of the direction of the M vector. This rotation can be applied to the magnetization $M_{||}$ and to the M_{\perp} vector along each axis. Of particular interest is the effect of the inversion applied to M_{\perp} after a short time since P90: M_{\perp} begins to decrease due to the dephasing action of the thermal agitation. Loosing coherence in the motion, we will find the faster spins in the external trajectory, as shown in Figure 2.21.

Operating the inversion along the y -axis as shown in Figure 2.22, we have the a vector, which is faster than b , still in the external position to b but now rotating in the opposite direction. Spins start to recover phase and M_{\perp} has again the maximum intensity. This generates the echo signal that can be measured with the coils. So, by applying the RF pulses to invert magnetization, it is possible to generate an echo of the magnetization to be measured as needed.

RF pulses can be applied in different ways with specific functions related also to the shape of the RF pulse expressed by the *bandwidth*. This function can determine the selectivity on particular spectral regions. With this kind of a strategy, it is possible to control the magnetization transferred on the plane orthogonal to B_0 . In this way, the contrast in the images will be dependent on the kind and the amount of magnetization transferred; in fact, the pulses used to transfer the proper magnetization for the contrast of interest can be spectrally selective and can be used to reduce the MR signal from some types of tissue leaving other types virtually unaltered. These kinds of pulses can only reduce the MR signal. Consequently, there is an increase in the image contrast, because the effect is tissue-specific. A widely used application of these kinds of pulses can be found in the

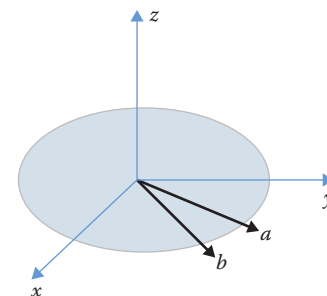


FIGURE 2.21 Rotating spins with different phases and velocity.

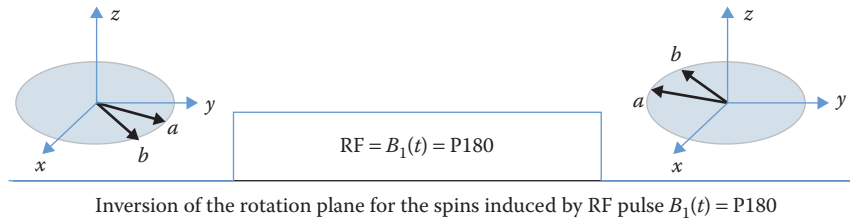


FIGURE 2.22
Spins after P180 pulse inversion.

magnetic resonance angiography (MRA), applied particularly to the cranial district, and performed with the so-called time-of-flight (TOF) sequence, reported in the following. Spectral selective pulses are used to attenuate the MR signal from brain parenchyma, while leaving the signal from blood unaltered.

This is just an example. All these functionalities and others not mentioned before but used in the modern MRI are performed by means of a sophisticated technology for the engineering of the shape, duration, and integration of the RF pulses with a gradient system. From the mathematical point of view, many of these arguments are very difficult to treat and we will have a qualitative approach to this argument.

Before moving further, let us have a look at the analog properties related to the gradient of the static magnetic field: the application of properly shaped and timed gradients allows us to further manipulate the spins and the magnetization.

Concluding, a proper mathematical description for these arguments is out of the topic of this chapter: interested readers can consult a proper treatment of the arguments in

1. *Principles of Magnetic Resonance imaging* by Yi Wang
2. *Handbook of MRI Pulse Sequences* by Bernstein et al.

2.3.4 Gradient Waveforms and Macroscopic Net Magnetization M Effects

A controlled variation of the static magnetic field in MR is a powerful tool for the manipulation of spins, at the microscopic level, and of the \mathbf{M} at the macroscopic level. Introducing a linear variation of the magnetic field overlapped to the static B_0 value along a direction of action produces the dependence of the Larmor frequency on the local value of the field. The static magnetic field during the switching-on of the gradient can be expressed by the following equation:

$$B_0(x) = B_0 + \left| \begin{matrix} i \\ G_x \\ r \\ x \end{matrix} \right| \quad (2.12)$$

$$\omega(x) = \frac{-e\hbar g}{2m} B_0(x) \quad (2.13)$$

Introducing a linear gradient field for each direction, we add a spatial label to give a different Larmor frequency at each point of the space in the magnet bore. In this way, we introduce a code for the spatial position by means of the different Larmor frequency assigned to the protons located in that place. Easy, powerful, and extremely important for the imaging technology based on the NMR, the spatial encoding of the Larmor frequency is used in the image reconstruction process to realize the slice selection along the z -axis and in the x - y plane to have the 2D *image signal*.

The shape of the gradient can be designed to produce particular effects on the nuclei polarization and consequently on M . Gradients can also be used to compensate inhomogeneity in the static magnetic field. This is an important operation because the magnetic field is altered by the introduction of the sample, the patient body for MRI. The *shimming* compensation, usually performed automatically in MRI, is an important operation for the quality of image or for the *cleanness* of the signals from the tomograph acquired for the spectroscopic analysis, both *in vivo* and *in vitro*. Shimming is performed, in an active way, by coils with particular shape around the FOV and controlled by the computer.

It is important to have a visual representation of the gradients. Let us consider a gradient operating along the x -axis and a gradient operating along the y -axis. We will use the negative and positive variations of the field along each direction, the so-called positive lobe and negative lobe of the gradients.

MR pulse sequences usually contain gradient waveforms for the frequency and phase encoding, and one for the slice selection. Commonly, each gradient pulse has two lobes, positive and negative, with different shapes: trapezoidal, triangular, and sinusoidal, depending on the requested imaging parameters (Figure 2.23).

Along each axes, we have a field profile as reported in Figure 2.24.

It is important to understand that these variations can be applied simultaneously on both directions or with an opportune timing considering, for example,

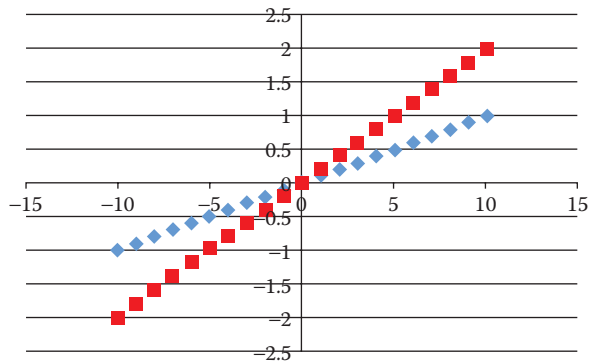


FIGURE 2.23
Strength and slope of gradient.

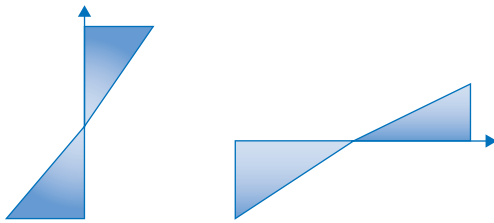


FIGURE 2.24
Linear gradient profiles for y - and x -axes.

the possibility of introducing the application of particular RF pulses. This is what happens in a particular kind of sequence to prepare the magnetization of some tissues.

An important consideration: gradients along the spatial axes allow for the labeling of the space with a different Larmor frequency for each point of the field of analysis. The receiver will capture the spectral frequency range depending on the excitation of RF pulses and on the gradient intensity and the gradient-related local magnetic field values.

If used properly in a combined way, both RF pulses and gradients give the researcher the possibility of manipulating spins and sampling signals in an extremely variable and plastic way. The primary use of gradients is the slice selections, that is, the selection of a slice of tissue to represent along the z -axes (the axial projection of the x - y plane) along the x -axis (the longitudinal projection of the z - y plane) and along the y -axis (the coronal projection of the x - z plane). After a plane selection, gradients act along the x direction for the so-called frequency encoding and along the y direction for the so-called phase encoding. Figure 2.24 gives the spatial representation of the gradient profile. In the sequence engineering, the time profile of the combinations of the characteristics and timing of the radio pulses and magnetic field gradients is important; they are used to manage the manipulation of the NMR signal and represent the so-called sequences. Different time lines are used for each gradient; one time line is used for the RF pulse representation

and one time line is used to represent the signal collection time. To keep pulse sequence diagrams as easy as possible, authors are used to simplify the representation of the gradient shapes in the drawings. One of the most common simplifications is to draw gradients as perfect rectangles, whereas they should be drawn as trapezoids (or some similar shape) having a more gradual rate of rise and fall; in fact, performances of the electronic gradient unit are expressed by their intensity, in mT/m, and their speed of variation, in mT/m/s. Another frequent simplification in the gradient drawing is that, in many references, the smaller downward projecting lobe in the slice-select gradient immediately after the RF pulse is not represented. This slice-rephasing lobe exists, and it helps to correct the phase dispersion of transverse magnetization that occurs with the application of the main slice-select gradient. Without the application of the rephasing lobe, we will tackle with an intravoxel phase dispersion, resulting in signal loss (Figure 2.25).

How gradients are used in MRI? This is a very important part of the *sequence* engineering. The z gradient is also called the gradient of selective excitation. It is applied along the z direction modifying in this way the Larmor frequency in this direction. Then the slice will be selected using a narrow-band RF pulse with the primary frequency centered on the value of interest.

The y gradient is called the *phase gradient* and it is applied for short time intervals. It used to de-phase the spins for a certain amount, and then it is switched off. After this procedure, spins return to rotate together, with the same angular velocity but with a constant phase shift dependent on the y coordinate. It is switched on and off with different intensities.

The last gradient is the x gradient, also called the readout gradient, is switched on during the *reading* of the signals from the P90 or P180 pulses.

Gradients can be activated several times in order to cover all the lines of the matrixes and all the slices selected. The process of timing of these pulses is very important. It is also energy consuming, and an apposite power unit is frequently devoted to the gradients supply. Finally, to describe the timing and the effects of RF pulses and gradients, we will use a diagram with these lines (Figure 2.26).

In each line, we will report the shape and the temporization for RF pulses and gradients. But now, before going further with the sequence description, it is better



FIGURE 2.25
Rephasing lobes.

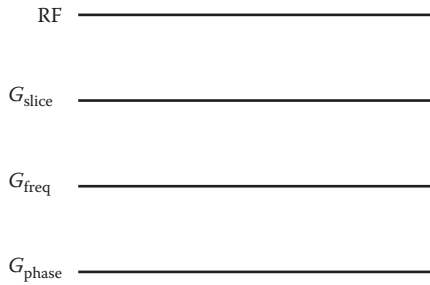


FIGURE 2.26
Representation for the sequence.

to give some more detail about the relation between the space position of the spin in the image FOV and the Larmor frequency and the energy of the RFs. We will introduce the important concept of the k -space in MRI.

2.4 k -Space and Complexification of the Space

Which is the best *workspace* for the MRI? We can start this discussion with some important considerations expressed in the previous paragraph: gradients along the spatial axes allow for the space labeling with a different Larmor frequency for each point of the field of analysis in view (FOV). The receiver, or coil, will capture frequencies in a spectral range depending on the excitation RF pulses and gradients activated during the excitation and the reading process.

So, there is a correspondence, through the Larmor frequency, between energy and spatial coordinates in the laboratory frame, expressed by the dependence of the Larmor frequency from the \mathbf{r} vector. So, $\omega(\mathbf{r})$ has a spatial distribution in the volume, or region of interest. Further, in MRI, the nature of the signal image is discontinued, due to the sampling and quantization of the space in voxels and pixels, and consequently also the image has a discontinued structure. The voxel or pixel in the image is a quantization of the spatial coordinates. There is a sort of lattice in the space, and coordinates are the multiple of axial spatial resolution of the gradients used. This is the reason why in imaging we speak about the image as the spatial matrix and treat the image as a matrix of pixel in 2D or voxel in the 3D or 4D matrix in the case of the fMRI. Properties of this matrix or lattice are quite complicated. So, the matter is represented with a periodic structure, like the lattice model used in the solid-state physics. Variations in the position, in a space nestled in gradients of magnetic field along all the axes, means to consider different energy states of the spins with differences in terms of frequency and phase associated with different voxels.

Well, where is the problem? Obviously, in Mathematics, the proper manipulation of the properties of these two workspaces is required: one related to the spatial coordinates and the complementary and the other related to the energetic coordinates. Usually, at this point of time, we should need to introduce the Fourier transform, the mathematics tool to correlate the spaces of some functions. But I would like to propose an innovative pathway related to the possibility of making the workspace of the MRI *complex*. So, let us introduce the complex numbers in MRI.

Let me give a brief excursion about the linear algebra used in the most part of our university studies: the great limitations to the calculus are given by the restriction to work in the \mathbb{R} ensemble! But \mathbb{R} is not a *good ambient* to work in. The natural environment for algebra, and particularly for matrices algebra, is \mathbb{C} , the complex space, where the application of algebra is straightforward and easy to understand. In the MRI Physics, we are in the same situation. We have to use a space with properties useful to calculation and explication of spin properties: this space is called the k -space which is properly defined in the complex space as a complex, discontinuous and with *reticular properties* space. k -space actually simplifies the comprehension and the use of data acquisition and evaluation methods used in MRI and in NMR microscopy. Obviously, you need a strong mathematics background to properly handle the k -space for these purposes, and most of this mathematics is related to the Fourier transform. Students of physics meet the k -space concept during the studies about solid-state physics, based on the concepts of reciprocal lattice, Brillouin zones, and Fermi levels. Also Bloch, the author of the phenomenological magnetization equations, produced a great amount of study of the EM interaction in periodic structures in the complex space. Bloch defined the auto-solution of the photon solid matter interaction problem.

Applications of the k -space formalism regard many fields in medicine, such as X-ray scattering, ultrasound echography, positron emission tomography, and electron microscopy. Its introduction into NMR and MRI can be found in the pioneering works of Ugurbil and Twieg. However, considering its deep roots in physics, the concept has never been considered as particularly important in other disciplines; and it was just used at minimum due to the fact that the most part of our algebra is in \mathbb{R} instead of \mathbb{C} . In fact, we need complex numbers to better introduce the k -space concept very useful in the MRI.

The first step toward this is the introduction of a generic vector $\mathbf{K} = (K_x, K_y, K_z)$ that we will later associate with the energy values of the spaces; then we can define the product of this vector with the spatial vector \mathbf{r} :

$$\mathbf{K} \cdot \mathbf{r} = (k_x x, k_y y, k_z z)$$

Then, we can consider the complex exponential function of this product that can be indicated as

$$e^{i(k \cdot r)}$$

term1

where i is the imaginary unit to define a complex number; this is the function that can be used for the complexification of a generic vector \mathbf{P} represented in the space.

There are several representations of the complex number (Figure 2.27). Using the $\cos(\theta)$ e $\sin(\theta)$ components of a vector in the 2D space, it is possible to relate the Cartesian coordinates with the component of the complex number z as

$$z = \rho[\cos(\Phi) + i \sin(\Phi)] = \rho e^{i\Phi} \quad (2.14)$$

Now, we can define a new vector with dependence from the spatial coordinates r , $s(\mathbf{r})$. Starting by $s(r)$ we can use the definition of term 1 and the vector \mathbf{K} to define the function $\tilde{s}(k \cdot r)$ defined in a infinitesimal volume dV :

$$\tilde{s}(k \cdot r) = s(\mathbf{r}) * e^{i(k \cdot r)} dV = s(\mathbf{r}) * e^{i(k \cdot r)} dx * dy * dz$$

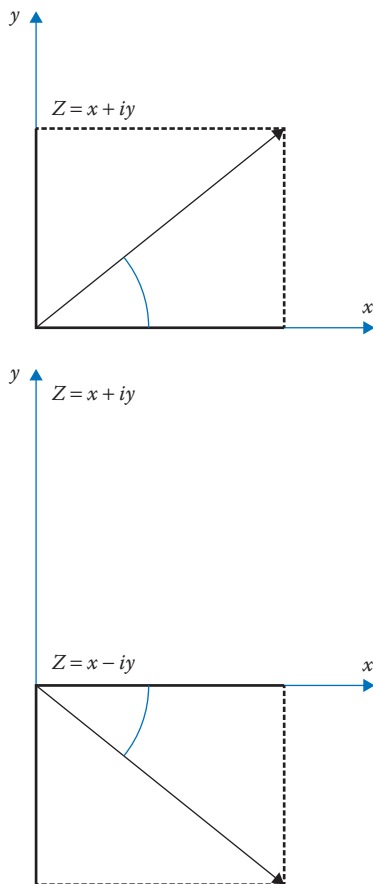


FIGURE 2.27
Complex number in the vectorial representation.

$$\int s(r) e^{i(k \cdot r)} dV = S(K)$$

FIGURE 2.28
Complex function $S(K)$.

In order to remove the dependence of this quantity from the spatial coordinates, we can operate an integration summing in this way all contributions from each voxel in the volume of interest V , and we can define a new entity, the distribution $S(\mathbf{K})$ with the direct dependence from the \mathbf{k} vector alone and that has the property to be a complex function of a real variable (Figure 2.28).

In this way, we shift the functional dependence from the r coordinates to \mathbf{k} vector. The new function $S(\mathbf{K})$ has the important property to be complex and to be related to the time evolution of the *coordinates* of k . Information in $S(k)$ is related to all the coordinates of the field of interest FOV; integration has the function to sum all the components from all the coordinates of the space. This will introduce an important characteristic of the k -space images: each pixel of the images will have energetic information from the spins of all the voxel of interest VOI!

Now, according to the standard NMR theory, and using the arguments previously introduced, we can do some other considerations:

1. The use of gradients means to change the frequency and the phase of the spins and magnetization in the voxels.
2. Generally speaking, gradients are time-dependent.
3. The k -space is specifically related to the frequency and phase of spins and macroscopic magnetization.

From all these considerations, we can say that protons contained into a volume $dx dy dz$ give an NMR signal:

$$\int q(r) e^{2\pi i k(t) r} dV = Q(K) \quad (2.15)$$

Using the term-to-term identification method, we can see that formally $S(k) = Q(K)$. The time evolution of the vector \mathbf{K} is related to the way to change the energy relation between the spatial label and the magnetic field. These physical entities are related to the way to combine RF pulses and gradient values, which means to manage a *trajectory* defined in the complex k -space and depending on the gradients and pulses applied.

We have seen that using RF pulses and gradients, we can move along any desired k -space path. In this path, we build up a record of the $Q(K(t))$ or $S(K(t))$ values for a subset of the *visited* k -space points. *Visited* means *measured*. These are the signals revealed by the coils. This signal contains, as a real function of the r real coordinates,

information about the spatial labels of the signal, but, as a complex function of variable k , that is also a time-dependent function; this information is hidden in the $K(t)$ and in the image. So, by means of the RF and gradient pulses, you can select the k -space points to select and sampling the NMR signal! The trajectory in the k -space is related to the way the proper pulses and gradient sequence are managed for the image contrast of interest!

But what kind of image do we record in this way? Is it the one shown in Figure 2.29?

This is not an image that can be used for the representation, but it is the real representation of the signals measured by the scanner. This kind of image is sent by the *reconstructor* PC of the scanner to provide the representation for tissue and organ imaging. k -space images give a real representation of the signals acquired. Before treating how these images are used to realize the imaging of the inner organs, we have to make other important observations about the k -space. The function $Q(K(t))$ is complex. This is in accordance with the fact that the actual NMR signal has a phase, and it is completely detected by two signals acquisition along axes; these signals have a 90° phase difference and they are detected using the coils in *quadrature detection* mode, with orthogonal RF reference signals. The two channels, often denoted as u and v , provide two time-dependent output signals $u(t)$ and $v(t)$, which behave as the Cartesian components of a complex signal $S(t) = u(t) + iv(t)$. Again, a complex representation of the NMR signal gives us the possibility of getting all the information from the scanning of the magnetization vector also in the complex space of interest. This is the point: our information, the information in MRI, regards, at the same time, both the energy and the position of the *emitter*! We need complex numbers to treat this kind of information! But they cannot be related to the usual space images of the Imaging.

So, what has happened? The introduction of this formalism has several consequences, and the descriptions

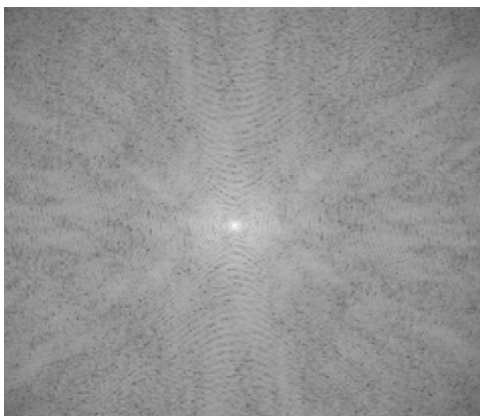


FIGURE 2.29.
 k -space representation of the image in MRI.

of some of which are beyond the scope of this chapter. However, there is an important point to consider: with the introduction of the complex number formalism, it is easier to discuss about the frequency and phase of a vector, and tissues magnetization is a vector, and not only about the module or intensity. The phase and frequency are two really important parameters in the MRI because they are related to different physical states of protons in different positions in the matter that can be revealed to exploit information to use in the imaging contrast. Different x , y , and z coordinates mean different k_x , k_y , and k_z energy point in the k -space.

With this complex vector transporting all the different energetic state of the spins in different positions, we can accurately differentiate the states of tissues magnetization in order to produce MRI signals dependence related to the intrinsic tissue parameters by means of the extrinsic parameters to settle up on the scanner: our contrast of image. Each energetic state of each tissue in different location, because of the great amount of intrinsic parameters in the MRI, can be labeled in different ways with these parameters, in order to distinguish among them and among different pathological states. But this sensibility and specificity of the imaging technique are related to the possibility of calibrating electronically pulses and gradient as the best we need. This is the power of the MRI. The possibility of increasing the sensibility and the specificity of the exams improving the technology of RF and gradients pulses! It is important to understand that in some situation it is better to have powerful gradients and RF systems instead of a high MR static field. Using the information stored by the timing and powering sections of the scanner during the production and control of the RF and gradients signals, we can map the k -space as requested by our exam: slice thickness, interslice gap, and tissues to excite or to saturate in order to change the magnetization contribution to the signal recorded. We can choose all these parameters by selecting the way to sample the k -space; then, the reconstruction will be all, and we need not convert the physiological image as shown in Figure 2.29.

Spatial localization for the slice selection and the y -axis position are encoded by the difference of the Larmor frequency induced by the z gradient and the y gradient; the second axis in the x - y plane can be encoded using the differences in the phases activated by a short and fast gradient pulse applied along the x -axis and related to the different position of the protons along the x -axis. A little dephasing is applied but it expires as the gradient pulse is switched off. After this controlled dephasing, spins move back in a coherent way, but with a different phase. In order to map all the position along x -axis the pulse gradient must be applied several times at different intensity, while the frequency encoding is obtained with a single longer gradient. So for each frequency gradient switched-on for a particular x position

there are a sequence of faster and much more intense gradient along the y -axis.

In this way, the encoding for a single y position represents a sort of *offset* for the frequency encoding along the x -axis. The frequency can be the same but with different starting phase. The combined use of these two gradients allows us to elaborate a strategy of k -space covering that we can call *trajectory* in the k -space. We have to point out that k -space is a lattice, a reticular disposition of points along the x - and y -axes, and this is due to the discrete nature of the coordinates in the MRI space partitioned in pixel and voxel, due to the sampling process of the NMR signals and to the digitalization of the RF pulses. Motion on this lattice to cover points of the k -space is controlled by gradients and RF pulses application.

The other important property of the $Q(K(t))$ mentioned before is that, as represented in Figure 2.29, the image of this function in the plane usually appears extremely variable and without connection to the image of the organs and tissues in the body: it is difficult to relate the images in the k -space with the real images, but there are some important properties of these images: we can demonstrate *experimentally* that, since we always image spatially bounded objects, the area of the k -space where $Q(K(t))$ reaches important values is limited to a central region of the k -space image and it is related to all the structures and tissue of the real image. At large distances from the origin, $Q(K(t))$ becomes smaller than the experimental noise and it has no sense to continue mapping values along the spectral coordinates. With these concepts in mind, we can do another important consideration about the pathway to use in the covering of the k -space: it is possible to demonstrate that $S(-k) = S^*(k)$, with the star denoting complex conjugation operation on the complex number. This means that there is a inner symmetry in the k -space, related to the nature

of the quantity $S(k)$ or, in our case, $Q(k)$. Therefore, we could chart $Q(k)$ only in a suitable part of the k -space.

As mathematicians will have noticed, we have not yet introduced mathematically the important tools defined by the Fourier transform. All discussions introduced by the complexation of the k -space are related to this strategy of theoretical treatment of the argument. I'm really interested to the diffusion of the importance to do calculation in \mathbb{C} instead of \mathbb{R} , but we will use the tool within the ImageJ software and for this reason we have to illustrate the properties of FFT, the algorithm to calculate the Fourier transform.

We can illustrate these steps in *imaging way*. Using the open source software ImageJ freely available from the Web, we can easily correlate dicom medical images with their k -space. The mathematical operation to do this is the Fourier transform. We will not discuss about the Operator Fourier Transform. We can avoid this using the concept of complexation of the space, much easier; using ImageJ we can charge a slice from an MRI structural study and we can move from the image to the related k -space and vice versa.

Using the area selection tool, we can capture portions of the k -space to delete or to replicate in other parts of the image, operating geometrical operations like reflection or axis inversion.

From the initial image of a brain slice, we can open the corresponding K -image space and select a square inner part to delete the external region of the k -space (Figure 2.30).

Which is the effect on the image? Visual comparison of the two images seems to reveal no differences, and only a mathematical subtraction of the second image from the first one can be evidence of a slight change exhibited in the following comparison and only in some details of the image, as reported before. So we can say

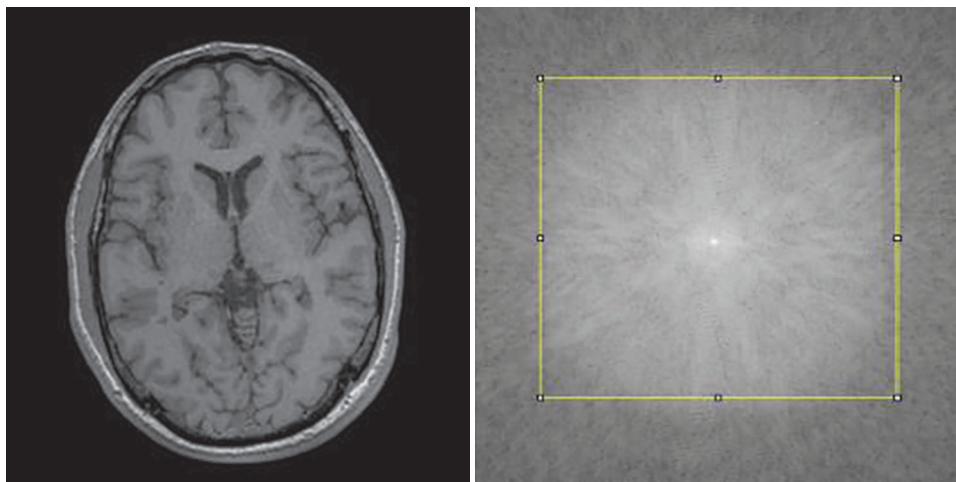


FIGURE 2.30
MRI image and the k -space representation.

that external part of the k -space is related to *details* of the image with low importance (Figure 2.31).

Selecting a smaller square we have these effects with a more significant effect of alteration. Other geometric property can be exhibited with this k -space operation we can remove the lower half part of the k -space and substitute it with a reflected upper part (Figures 2.32 and 2.33).

The effects of this operation on the image are shown in Figure 2.34.

One of the most important properties of the \mathbb{C} space is the ability to make integral calculation easy. In the \mathbb{C} space the mathematical tricks used to calculate the integrals are frequently transformed into a proper choice of the *integration path*. The functions of complex variables exhibit unbelievable simplification properties along particular paths. Using the \mathbb{C} space properties and the c -number properties is easy to demonstrate that some important mathematics operators are *well-defined*

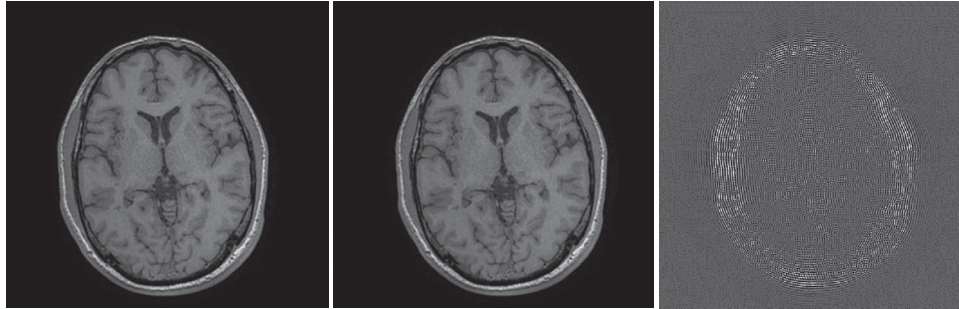


FIGURE 2.31
Effects of the elimination of the external part of the k -space in the image.

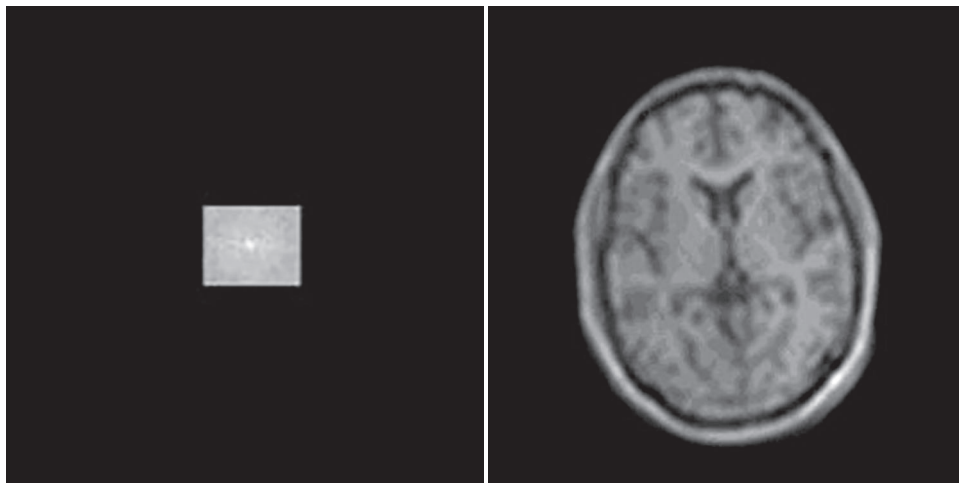


FIGURE 2.32
Image related to a smaller centered part of the k -space in Figure 2.30.

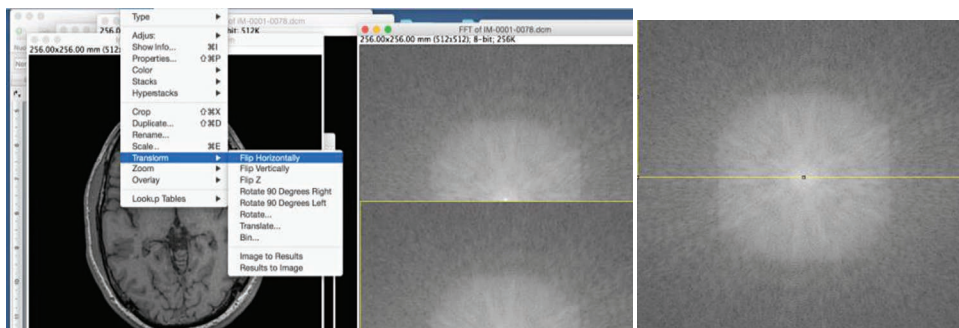


FIGURE 2.33
Manipulation of the k -space image: removal of the lower half with the mirror relative to the axis passing through the origin.

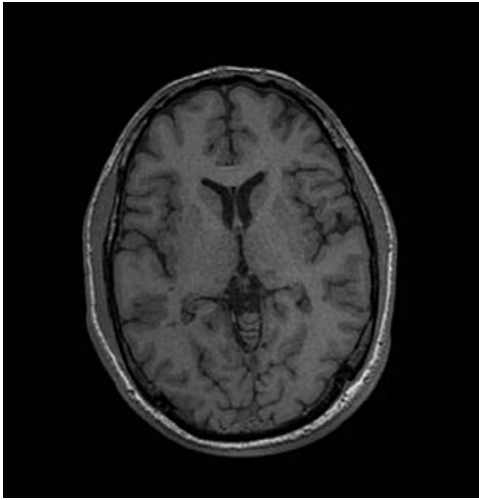


FIGURE 2.34
Geometric operations of parts of k -space duplication make the same starting image.

with the exponential representation of the complexity of the operator. Path and rotation are exhaustively explained in \mathbb{C} space and the physical applications are better defined. This is the same situation for the MRI physics. As shown in Figures 2.32 and 2.33 and previous images the properties of the k -space can be used to describe some properties of the related images acquired. Also, using the interpretation of the K-vector introduced in the beginning of the paragraph as an energy vector, we can map the different energy values as different particulars of the tissues to describe MRI. We need complex numbers because in this way it is natural to introduce the phase parameter for the spins or magnetization vector. Phase became an important extrinsic parameter to control the image contrast in MRI. The combined choice of pulses and gradients is the path definition in the k -space to select part of the echoes signals to excite and acquire. This is important to understand. It is a key concept in MRI. We can select the elements of the k -space to better *construct* the image's characteristics we want to acquire. Energy selection in the k -space contains the spatial selection in the usual space but it is not only a spatial selection. This is the reason because the k -space has no direct representation of the image. The k -space contains the spatial selection but it is not only a spatial selection, there is also the association with the energy selected and also with the tissues selected. In other words, in the k -space we have all the instruments to properly select the contrast to visualize. Some other details to better understand the k -space.

We can magnify the structure of the raw image of the k -space related to an image of the brain: we can note that, obviously, also the k -space is *quantized* and has a pixel structure like the image representing the real inner

head structures. Obviously, because there is a sampling and quantization process related to the acquisition of the MRI signals. But the pixel of k -space is not related to a single pixel of the real space image.

In Figure 2.35, you can see the central portion of k -space image of the slice reported in Figure 2.37 acquired with the use of ImageJ software.

We can select a squared area of 3×3 pixels around the center and then after the clearing of the image around the selected square we can reconstruct the image (Figures 2.36 and 2.37).

In the visual comparison between the starting image and the elaborated one it is clear that the small portion of central k -space has information about the entire pixels of the *spatial* image. This is due to the fact that in our formula for the $S(k)$ or, in our case, $Q(k)$, we have integrated the signal along the spatial coordinates $dx dy dz$ of the V volume of interest.

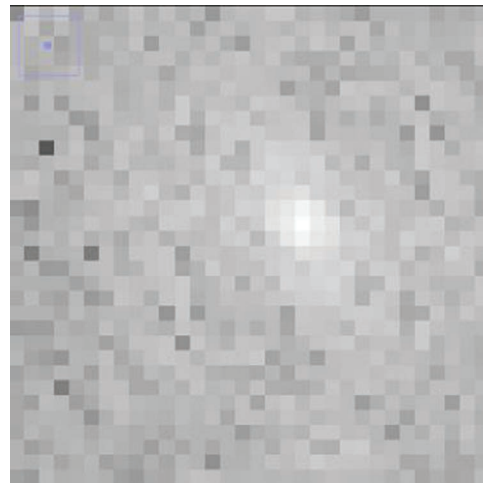


FIGURE 2.35
Pixel structure of the k -space image.

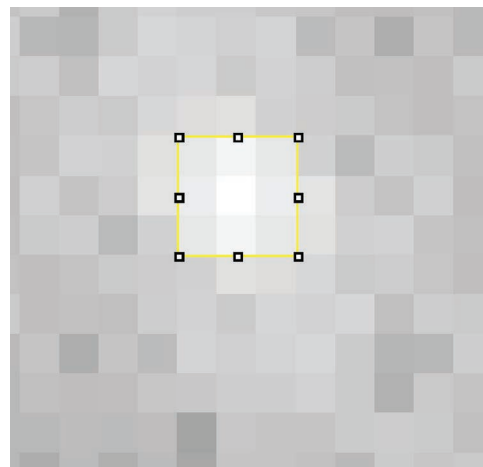


FIGURE 2.36
Pixel structure of the k -space image with higher magnification.

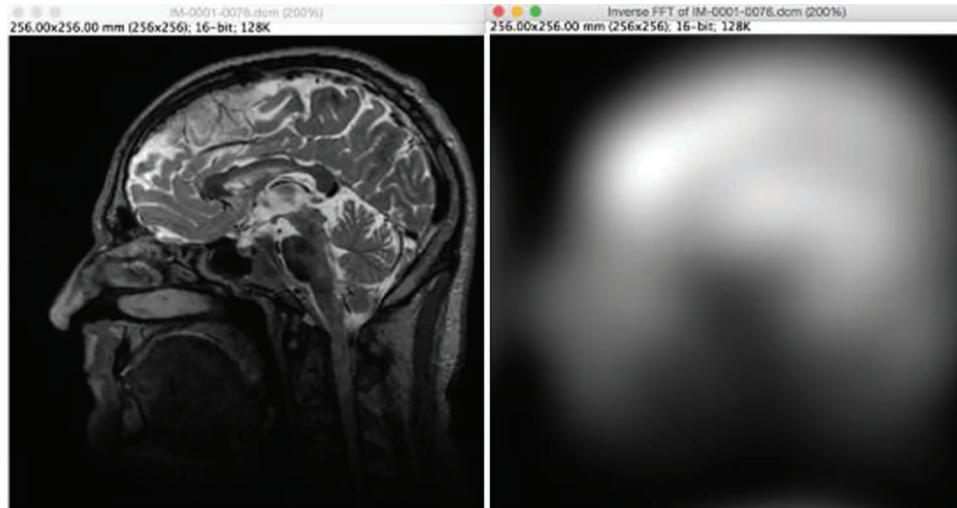


FIGURE 2.37
Details from a small portion of the k -space related to all the pixels in the real space.

Increasing the dimension of the square around the center, we can increment the detailed definition of all the *spatial* images. Selection of the k -space is shown in Figure 2.38.

Again, we have a greater amount of information and details for all the spatial pixels of the image. Let me show you some more interesting examples of the k -space properties. Let us select the portion of k -space around the center as shown in Figure 2.39.

The reconstructed image from Figure 2.39 is shown in Figure 2.40 with the selection (Figure 2.41) and the reconstructed image from Figure 2.41 is shown in Figure 2.42.

The geometry of the details is related to the paths of k -space covered: so a good strategy of k -space covering

can give to the researcher the possibility to acquire images faster and in order to increase as better as possible the SNR. External portion of the k -space can be related only to noise of image and it is a good strategy to acquire only in smaller part centered to the origin of the k -space.

At the end of this chapter and with all these instruments, we can resume an operative definition for the term *sequences*: in MRI, a sequence is a preselected set of defined RF and gradient pulses; some of these pulses can be repeated several times during the acquisition process defined as *scan*. The time interval between pulses, the amplitude and shape of the gradient waveforms, are used to manipulate spins and, at the macroscopic level, the net magnetization. After the first decay

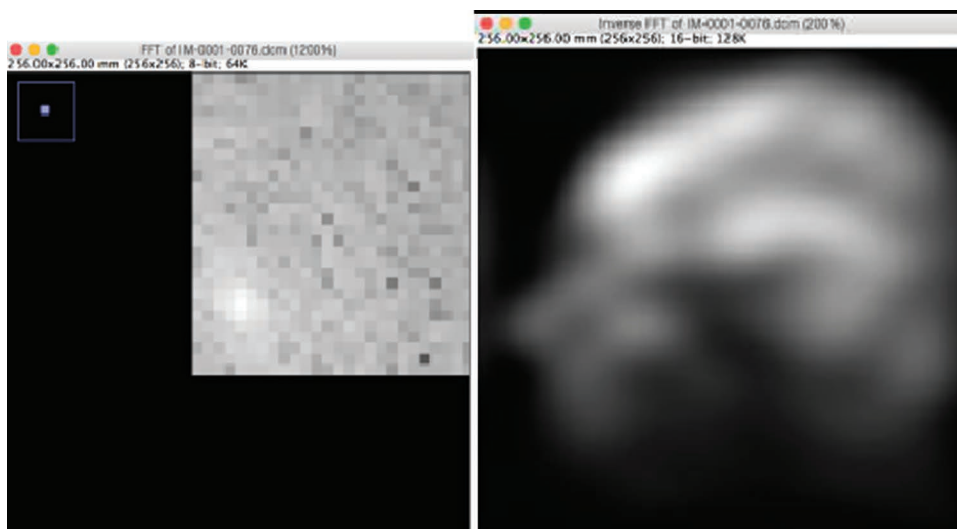


FIGURE 2.38
Portion of the k -space and related image.

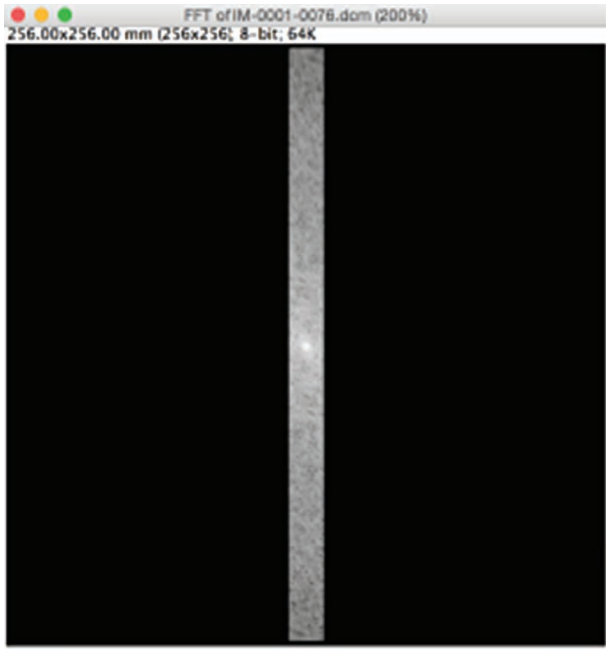


FIGURE 2.39
Horizontal slice of the k -space related to all the pixels in the real space.

of magnetization spins, defined FID, the manipulation of spins with RF pulses or frequency and phase gradients can generate a sort of echo of the FID signal: this mechanism use the dephasing–rephasing technique to produce new signal as echoes of the first one. By operating a control over the NMR signal reception and sampling, it is possible to affect the characteristics of the MR images in order to produce the proper contrast between the tissues of interest. Pulse sequences are generated by computer programs that control all the hardware

elements of the electronic chain in the scanner for the MRI process. By means of different pulse sequences, the radiologist can image the same tissue in various ways, and combinations of sequences using different parameters can reveal important diagnostic information about all the tissue. Magnetic resonance is dynamic and flexible; this technology allows radiologists to tailor the imaging study to the anatomic part of interest, to the functions operated by these parts, and to the disease process being studied. In this chapter, I have omitted the discussion of many topics of interest for a complete k -space description of many MRI techniques. The discussion of such topics assumes aspects beyond an introductory exposition.

Further, many important aspects of k -space were just barely mentioned, avoiding a proper mathematics description. I have tried to highlight the importance of k -space workspace with its versatility, which makes MRI so attractive to physicists and mathematicians, engineers, and obviously physicians.

2.5 Sequences and Contrast Control in the Imaging for MR

Gradients and pulses technology represent the most important and recent technical developments in the diagnostic imaging in MRI: gradients and pulses combinations realize the possibility to excite and detect, particularly selective modalities, signals to and from protons in the living matter due to a great amount of parameters that can be used to control these two phases of the images construction process in MRI: excitation

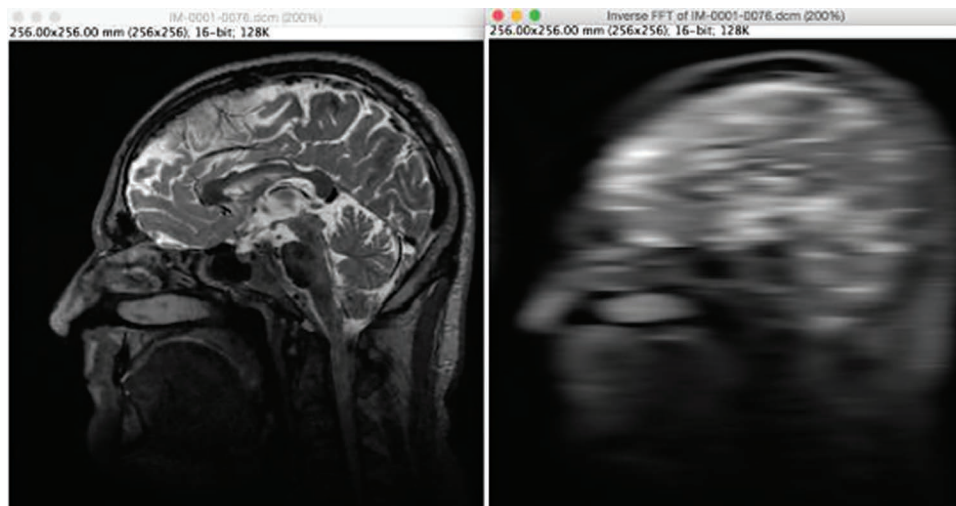


FIGURE 2.40
Comparison between the starting image and the reconstructed image for the portion of k -space in Figure 2.39.



FIGURE 2.41
Vertical slice of the k -space.

and acquisition. In order to properly illustrate the timing and technical characteristics of the sequences, several kinds of diagrams are used in the literature, where it is easy to represent graphically the effects of pulses and gradient waveforms on the magnetization. We will use the graph with four lines (Figure 2.43).

By combining shape, timing, intensity for the RF, and gradient pulses in this diagram, it is possible to explain the actions expressed on the spins and magnetization vectors; in other words, we can represent the most



FIGURE 2.43
Representation lines for gradients and RF pulses timing in the sequence.

important properties of the sequences reading the data coming from the k -space. We will use subscripts x to denote the readout (or frequency) directions and the y to denote phase-encoded directions. In order to understand the behavior of the spins under the sequence solicitation we have to discuss the values of the relaxation parameters for the different tissues. Typical values for the relaxation constants are given in Table 2.1.

Paramagnetic contrast media, like the gadolinium, are also used to locally reduce the constants T_1 and T_2 , as tissues with particular pathological state, as *fresh lesions* or *recent lesion* in multiple sclerosis, capture these media. In the clinical practice, proton MRI is used for the diagnosis: the most important signals in these conditions are due to the protons of the bulk water, defined as free, which is not linked and constrained to other molecules. Another important source of *proton signals* are the protons of the water linked to lipidic molecules with a structural geometry of droplets, a typical structure of the body fat. The semiliquid physical state of the lipidic droplets generates a strong spin-lattice interaction with a short relaxation time. Furthermore, fat can be related to some pathological

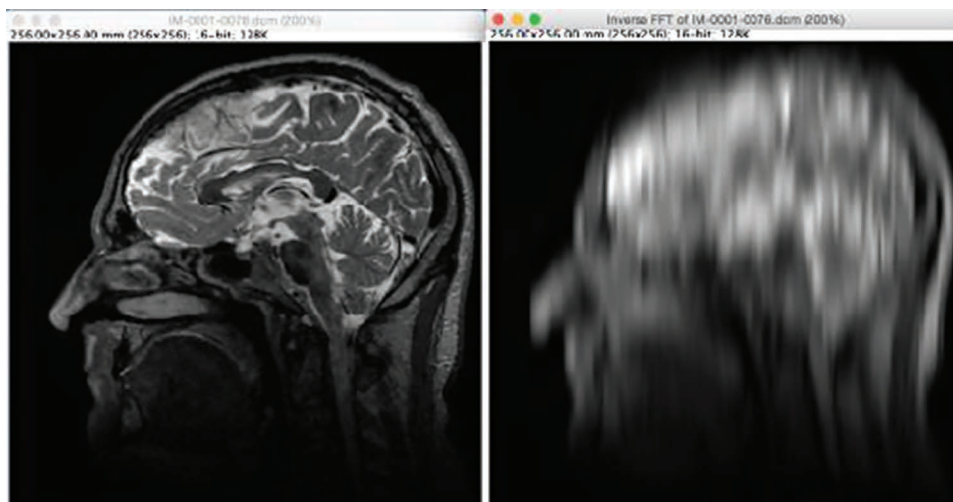


FIGURE 2.42
Comparison between the starting image and the reconstructed image for the portion of k -space in Figure 2.41.

TABLE 2.1
Relaxation Parameters of Some Tissues

	T_1 (ms)	T_2 (ms)
Water	3000	3000
Gray matter	810	100
White matter	680	90
Liver	420	45
Fat	240	85
CSF	800	110

conditions like the ones related to some kind of tumors, and in this case it is important to map differently this lipidic molecules by the natural lipids in order to build-up images with contrast power to differentiate, if possible, physiological fat by pathological one.

To try to solve this contrast problem usually the different component of the M vector are selectively excited with preparation pulses and dedicated sequences. Typical pulse sequence timing diagram uses the temporal lines to present the RF pulses, the three gradients applied, slice-phase frequency, and sometimes a fifth line to represent the signal recorded (see Figure 2.26).

Using this representation, it is possible to classify the sequences in different ways; from an historical point of view, the presentation of the classification based on the readout signal is interesting: sampling directly the FID signal or sampling a single echo of the FID signal or multiple echoes created with different strategies. The echo can be created from an FID with the use of a procedure of spin dephasing and rephasing using RF pulses or gradients waveform. Signal shapes are different: the FID has the typical damped sinusoid shape with T_2 temporal constant behavior. The echo signal shape has an increasing amplitude sinusoid with a dumping after the maximum amplitude. This shape is due to the fact that the recording of the signal usually begins when the spin is still in rephasing and proceed until dephasing again for the thermal agitation (Figure 2.44).

Techniques used for the echo creation are mainly differentiable about the pulse used: it is possible to create an echo with the use of a P180I RF pulse inverting the decreasing M plan of rotation (Figure 2.45).

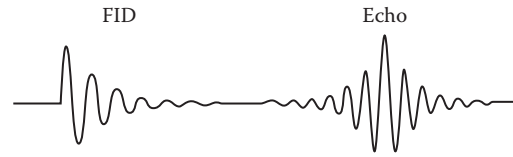


FIGURE 2.44
FID and echo signal shapes in MRI.

It is possible to create a single or multiple echoes using the phase gradient applied several times in combination with the slice and frequency selector gradients. The FID sampling sequence is not used in MRI and we will not discuss about them. We will start describing the spin-echo (SE) sequence and the gradient-echo (GE) sequences.

Usually, in the description of the properties and peculiarities of the sequences we discuss about the T_e , T_R , and the FA, three parameters settable by the computer control. PC allows us to control the amount and the typology of the collected signal; by changing T_R , T_e , and FA, it is possible to characterize the timing in the sequences of pulses and rising and falling of gradients according to the requirements to read the signal of interest among the signals emitted by the prepared magnetization.

The echo time represents the time elapsing between the application of RF excitation pulse and the peak of the signal induced in the coil. It is usually measured in milliseconds. According to the T_e values, it is possible to control the amount of T_2 relaxation.

Another important extrinsic parameter is the repetition time or (T_R) is the time from the application of an excitation pulse to the application of the next pulse. If we leave all tissues to relax completely, we can recover the total amount of magnetization (long T_R); for T_R shorter than T_1 's parameter of the tissues, a lower amount of magnetization will be recovered. T_R determines how much longitudinal magnetization recovers between each pulse. It is measured in milliseconds (Figure 2.46).

Another parameter can be used for the same reasons: the FA. It can be used to define the angle of excitation for a field echo-pulse sequence. It is the angle at which the net magnetization is rotated or tipped relative to the main

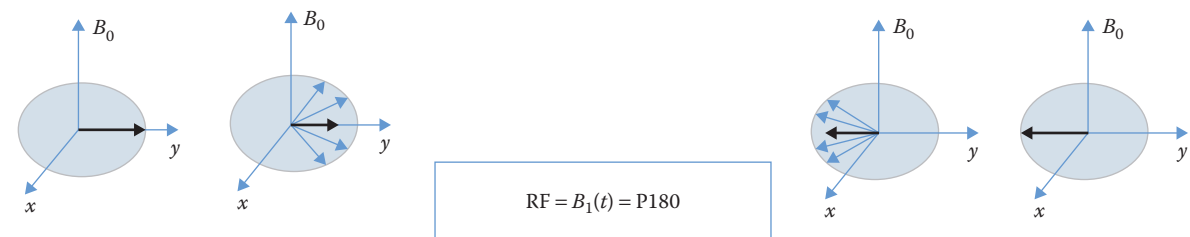


FIGURE 2.45
Echo from inversion.

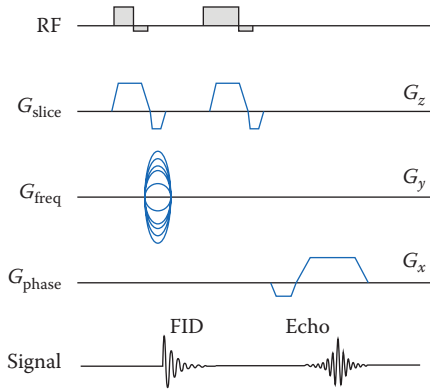


FIGURE 2.46
 T_e and T_R representation.

magnetic field direction by applying an RF excitation pulse at the Larmor frequency. It is also referred to as the *tip angle*, *nutating angle*, or the *angle of nutation*.

The RF pulse power (which is proportional to the square of the pulse amplitude) is calibrated to the number of spins that are tilted. FAs between 0° and 90° are typically used in gradient-echo sequences, 90° and a series of 180° pulses in SE sequences, and an initial 180° pulse followed by a 90° and a 180° pulse in inversion recovery (IR) sequences (Figure 2.47).

These are the most important extrinsic or technical parameters used in the MRI set up. Using these parameters, we can now describe the properties of the most diffused family of sequences and the innovations introduced.

2.5.1 SE Sequences

The SE sequence has been the first type of sequences produced for the spectroscopic use and then has been adapted for use in imaging. The schema of this kind of sequences is based on the use of a 90° initial pulse to flip the magnetization in the x - y plane and then a 180° pulse to invert the rotation plane of the dephasing spins for the refocusing process. The 180° pulse is transmitted

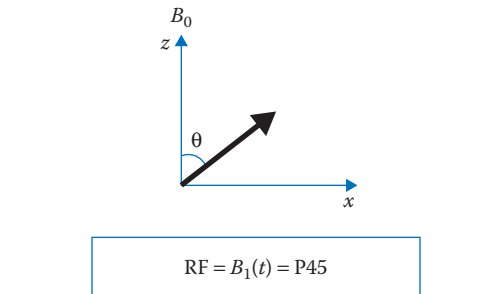


FIGURE 2.47
FA representation.

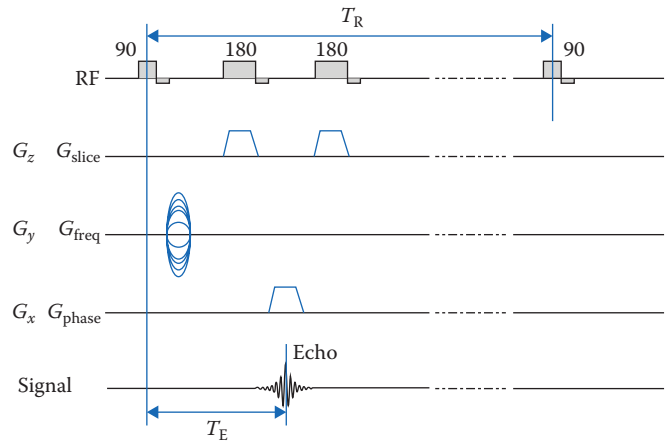


FIGURE 2.48
Spin-echo diagram.

exactly at the halftime between the excitation pulse and the echo maximum signal, this time is defined $T_e/2$ (Figure 2.48).

Let us see the features of this kind of sequences. After the first pulse, spins are aligned in the x - y plane and the FID signal produced during the recovery of the longitudinal magnetization is:

$$S = k\rho(1 - e^{-T_R/T_1})$$

In order to read the echo signal, we must apply the P180 pulse because the readable signal decay is only given by spin-spin relaxation. But, the application of the P180 pulse inverts the dephasing process (inverting, at the same time, x and y directions) and the echo is generated. The S signal becomes

$$S = k\rho(1 - e^{(-T_R/T_1)})e^{(-T_e/T_2)}$$

The use of the refocusing P180 pulse means that all the signal losses due to the B_0 inhomogeneity, to the susceptibility, and water/fat dephasing are recovered and neglected. Therefore, by means of the SE sequences it is possible to generate images with a weighting in the signal of the T_1 , T_2 , and PD components. Among the different advantages of this sequence, we can mention a high value of the SNR, a high spatial resolution and a low sensibility to different kind of artifacts like the inhomogeneity artifacts because of the refocusing P180 pulse.

It is clear from previous equation the MRI signal properties achieved with a proper manipulation of the T_R and T_e parameters in the sequences allow us a powerful multi parameter contrast mechanism in MRI.

By using a short repetition time and a short echo time, it is possible to approximate the signal with the T_1 -weighted term; for a longer T_R compared to a short T_e , the T_2 -weighted term is predominating. By considering finally in both terms of T_R long and T_e

long, we can achieve a weighting of the PD component in the equation.

So, the SE sequences can be used to produce a contrast control on the T_1 , T_2 , and PD values of tissues, it is possible to achieve for a single tissue a three-value label.

We have to consider some important disadvantages in the SE sequences: first, this family of sequences using a couple of pulses, the second one lasting twice as much as the former. In addition, there is a great amount of energy released into the tissues with a consequent increase in the specific absorption rate of RF power (SAR). The SAR is defined as the RF power absorbed per unit of mass of a tissue; it is measured in watt per kilogram (W/kg) and it describes the effects of heating of the patient's tissue. The organizations for the health quality assurance fixed precise limit to the SAR during the MRI examination in order to prevent tissues damages.

Another important point to consider about the SE sequences is the fact that for large FOV, the acquisition time is really long and this is particularly evident for the T_2 and DP sequences. Early attempts to reduce these negative effects in the SE sequences were undertaken using techniques to reduce the number of the k -space points to sample for the image production. The k -space has particular properties that can be used to reduce the energy release by RF pulses in SE sequences. As previously reported, k -space data is made up of complex values representing the M_x and M_y components of magnetization. The complex data in the right half of k -space is the complex conjugate of the data in the left half of k -space. Similarly, the data in the top half of k -space is the complex conjugates of the data in the bottom half of k -space.

Before we have to give some definition, the number of excitations (NEX) defines how many times each line of k -space data is acquired during the scan. The multiple acquisitions of the k -space lines is a technique adopted to increase the SNR by taking an average of the signals acquired and approximately SNR increase as the square root of the NEXs.

Now, the fractional NEX imaging technique takes advantage by the complex conjugate relationship between the top and bottom parts of k -space; these are symmetric and it is possible to reduce the number of phase-encoding steps, that is, the number of y gradients switching on. But due to the fact that fewer data points are collected in fractional NEX imaging, the SNR becomes poorer as NEX is decreased. So, it is faster but with a reduced SNR.

In *Half-NEX* imaging, phase-encoding steps +8 through -128 of +128 to -128 are recorded. Steps -128 through 0 are generated from the complex conjugate relationship between the halves of k -space. Phase-encoding steps -8 through 0 are recorded to assure the center of k -space is at 0 and there is a smooth transition between

the halves. Fractional NEX imaging sequences use NEX values between $Nex = 1$ and $Nex = 1/2$. The advantage of fractional NEX imaging is that an image can be recorded faster than with $Nex = 1$ but with the same contrast between the tissues as in the $Nex = 1$ case.

Another technique adopted to obtain a reduction in time acquisition and SAR is to reduce the FA, instead of the classic P90 pulse is used a shorter pulse; this reduce the time of acquisition and the energy released to tissue but still we also have a reduction in SNR, especially for the T_2 -weighted sequences.

Another important technological solution to the SE problems was achieved by suppressing the second pulse in the sequence: the echo signal can be generated by the use of the gradients instead of RF pulses, with an important reduction in the acquisition time and energy released; this solution has generated a new family of sequences, the so-called gradient-echo sequences.

2.5.2 GE Sequences

The gradient-echo family of sequences has been studied expressly for the imaging purposes. In fact, they use the system gradients to operate on the spins as well as for the space labeling. The gradient-echo sequence consists of a series of excitation pulses, all P90 pulses, each separated by a time interval defined *repetition time* T_R ; acquisition of data starting after a time interval defined T_e time. There is no P180 pulse and this results in a reduction of the T_R . In this kind of sequences, the sampling of the signal is carried out using a gradient starting with a FID dephasing along the x -axis and then protons are rephased by means of the inverted lobe of this gradient. The control contrast in the image can be obtained changing both T_R and T_e sequence parameters (Figure 2.49).

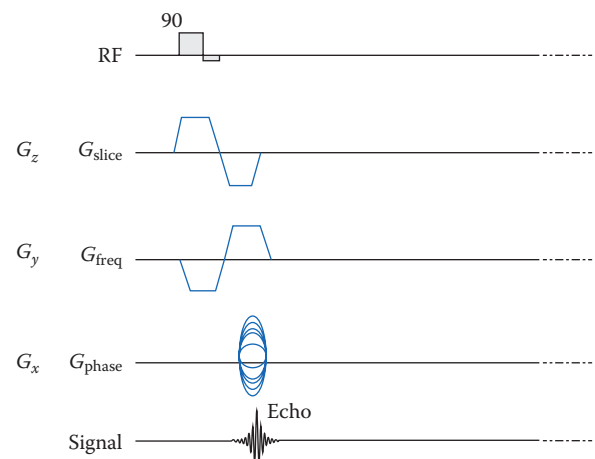


FIGURE 2.49 Representation for a typical gradient-echo sequence.

Also, the FA is used to produce a better T_1 weighting in the case of T_1 long tissues contrast, in order to avoid a long busy time of electronic for long TRs. But with this kind of sequences, the most important parameter is the T_e : there is a great amount of sequences used with the schema of the GE, namely the FLASH and FISP sequences, the FAST, and the SPGR sequences. The FLASH sequence is a GE fast sequence, producing signals of echo at low FAs; FISP sequence is a modification, with the exception that the spoiler pulse is eliminated. In this way, any transverse magnetization still present at the time of the next RF pulse is incorporated into the steady state. Using a small FA selection, a little amount of longitudinal magnetization is lost and the image contrast results quite independent of T_1 . Using a combination of very short T_e (T_R [10:50] ms) and a range of FAs in $[30^\circ:45^\circ)$, it is possible to reduce the T_2^* effects, so that the images become PD weighted. Increasing the FA, the contrast becomes increasingly dependent on T_1 and T_2^* : in this *region of work*, FISP exhibits very different contrast in comparison to FLASH sequences. FISP and FLASH can be used for orthopedic imaging, 3D MPR, cardiology, and angiography.

Generally speaking, gradient-echo sequences are used to control the image contrast weighting images in T_1 and T_2^* ; particularly, a T_2^* decay occurs between the dephasing and rephasing gradients and generates image contrast. In order to obtain good values for the SNR usually short T_e are used in this kind of sequences.

These sequences are generally sensible to B_0 inhomogeneity, magnetic susceptibility, and water-fat incoherence unrecoverable, especially using T_R shorter than 200–150 ms; for these T_R there is a residual magnetization along the x -axis for water and fat (see Table 2.1) disturbing the signal. In fact, for the T_R shorter than these ranges, the contrast became a function of the ratio T_2/T_1 and tissue differentiation it is undetermined in T_1 and T_2 . To resolve this problem and to be able to use T_R shorter than 150 ms, introduction of a series of preparative pulses or gradient waveform is considered. The use of preparation RF pulses has generated the family of the IR sequence, which we will describe in the follow. The use of different gradient shapes along the z , x , and y directions has generated several releases of the gradient-echo sequences: flow compensation sequences, rewind sequences, diffusion sequences, spoiled sequences, and bipolar lobes sequences, particularly interesting for the use in the phase contrast PC MRA.

A general advantage for the gradient-echo sequences is fast imaging sequence because they can use shorter T_R and T_e than SE; furthermore, by using a low FA, it is possible to deposit less energy than SE, with an important decrease in SAR. But there is an important disadvantage in these families of sequence: the great difficulty in generating good T_2 -weighted images.

As mentioned before there are many types of sequences based on the gradient-echo diagram:

- The so-called conventional gradient-echo sequence, like the gradient recalled acquisition in the steady state: It is possible to generate T_1 weighting, with larger FA value, and T_2^* weighting images, with longer T_e .
- The spoiled gradient-echo SPGR: Spoiling destroys accumulated transverse coherence and maximizes T_1 contrast.
- Contrast-enhanced gradient-echo steady-state free precession: Those are sequences with poor SNR, and, for this reason, they are rarely used; but these sequence can generate heavily T_2^* -weighted images.

The idea of the magnetization preparation in order to control the contrast in the MRI has an interesting result in the production of sequences defined as IR sequence. This family of sequence is similar to the SE and pickup the idea to prepare tissues to the requested contrast. By using a proper initial pulse, it is possible to neglect the unwanted signals and to highlight the contrast between the other tissues. Those are the family of the IR sequences.

2.5.3 IR Sequences

IR can be considered as a variant of an SE sequence as it begins with an inverting pulse, P180I, and then the usual single 90° excitation pulse is applied, after a time defined TI time of inversion, followed, as in SE, by the usual refocusing P180 pulse. In this way, the contrast mostly depends on the magnitude of the longitudinal magnetization, as in SE sequence, defined this time by the proper choice of the delay time TI time of inversion.

In this sequence, the time between the middle of initial (inverting) 180° RF pulse and middle of the subsequent exciting 90° pulse to detect the amount of longitudinal magnetization defines the extrinsic parameter TI.

There is the possibility to calibrate the inversion pulse P180I in order to suppress a particular tissue signal: during the inversion process, all the spins are altered by the pulse, and magnetization is the macroscopic expression of the local spin magnetic momentum. But by using gradients to differentiate frequency and phase of nuclear spins, it is possible to calibrate the P180I for a specific tissue by reducing and centering the pulse band of frequency. So, frequency, phase, and duration of the pulse P180I can be calibrated in a different manner, so that a particular tissue is suppressed or a particular contrast is enhanced.

Using broadband inversion pulses and TI selection, signal from voxel excited with this sequence of pulses and repetition time T_R is

$$S = k\rho(1 - 2e^{(-TI/T_1)} + e^{(-T_R/T_1)})$$

So, the important property of IR sequences is related to the choice of TI: if a TI is chosen such that the longitudinal magnetization of a tissue is null, the latter cannot emit a signal because the tissue will not have a transverse magnetization component because it will have no longitudinal magnetization to excite with the following P90 pulse of the IR sequence. The IR technique thus allows the signal of a given tissue to be suppressed by selecting a TI adapted to the T_1 of this tissue. Two different sequences are particularly used in TI: short-tau IR (STIR) also called short T_1 IR is the elective fat suppression technique with an inversion time $TI = T_1 \ln 2$ where the signal of fat is zero. This equates to approximately 140 ms at 1.5 T. Tissues with different T_1 values can be distinguished by use of this technique. But most tissues recover more slowly than fat, and so STIR images have intrinsically lower SNR. Particular care has to be taken during the interpretation of contrast between tissues because of the incomplete relaxation of the water signal of tissues when the image is acquired. IR imaging allows homogeneous and global fat suppression, and it can be used with low-field-strength magnets for large volume of interest. However, this technique is not specific for fat, and the signal intensities of the tissue with a long T_1 and the tissue with a short T_1 may be difficult to interpret.

Another IR-like technique used for the attenuation of unwanted signals is the fluid-attenuated IR (FLAIR) used to suppress water. This technique has a long TI to remove the effects of fluid from the images. For fluid suppression, the inversion time (long TI) is set to the zero-crossing point of fluid, resulting in signal erasing. Using conventional T_2 contrast some lesion in the parenchyma can be fuzzed by bright fluid signals; lesions result more visible, with a better contrast, using the FLAIR, which is an important technique for the differentiation of brain and spine lesions.

Another important use of the *inversion* techniques is for cardiac MRI: in this case, the sequence is used to null the signal from normal myocardium during delayed enhanced imaging. The normal myocardium will be dark in contrast to the enhanced abnormal myocardium. The appropriate TI at which the normal myocardium is dark occurs about 330 ms after the RF pulse, but varies from person to person. To determine the appropriate TI for an individual, a TI scout series is obtained where each image in the series has a progressively larger TI. Alternatively, a newer automated sequence known as *phase-sensitive IR* can be used, which does not require a

TI scout. IR pulses that are used to null the signal from a desired tissue allow us to accentuate surrounding pathology.

2.6 Sequence Engineering as a Strategy for Developing Innovative Diagnostic Applications

MRI is in constant development in several fields of the medical diagnosis. It is impossible to report all advancements in the several disciplines of medicine. We can report just a few examples for the modern brain functional and angiography, and we will discuss about the peculiarities of these sequences.

2.6.1 Functional MRI Sequences

2.6.1.1 Echo-Planar Imaging (Functional MRI)

Fast imaging in brain function studies is required in many field of diagnosis research; as in the case of functional connectivity brain imaging, we want to be able to follow the oscillation of the time series of the T_2^* contrast related to the tasks operated by the patients or to the default mode network of the resting state activity. The lines of k -space can be collected in a variety of different view orders to be fast; important application are achieved through echo-planar trajectories, employing an oscillating spatial selection gradient in the x direction and a unipolar gradient in the y direction. The speed of acquisition is greater than other techniques and this allows us the possibility to catch a *photo* of the brain functionalities related to the local contrast T_2^* in order to capture the functionality of the several brain areas. Using the BOLD mechanism to reveal the neuronal population activated in some areas of the brain generate a local T_2^* contrast related to the differential hemoglobin/deoxyhemoglobin ratio alteration related to hyperactivation of the neurons. The neurovascular coupling enables researchers to follow the neuron activity by means of an indirect mechanism of the BOLD effect.

Innovative sequence for the functional brain imaging is the EPI; EPI is really fast and it is possible to relate the oscillation of the brain T_2^* signal to the variation of the neurons activity. The technique records an entire image in a T_R period. To understand the EPI mechanism, the concept of k -space as previously discussed is of great help. The k -space is equivalent to the space defined by the frequency- and phase-encoding directions. Conventional imaging sequences record one line of k -space for each phase-encoding step. Since one

phase-encoding step occurs for each T_R seconds, the time required to produce an image is determined by the product of T_R and the number of phase-encoding steps. EPI measures all lines of k -space in a single T_R period (single shot).

Basically, the EPI schema can be based on both SE and GE mechanism, while the GE schema gradients can be used for the readout of the signal.

In this schema, we use the inversion of the y gradient to produce a single line of dephased echoes; inversion in the lobe gradient allows the reading of the single x -lines of dephased spins moving in opposite direction in the k -space (Figure 2.50).

The inversion of the k_x reading direction is determined by the gradient lobe value; alternating polarity of a series of readout gradient lobes allows us to sample each line of the k -space very fast. From the technical point of view, EPI sequence can use a double mechanism of phase-encoding waveforms: with constant gradient G_y , and with the *blip* gradients (Figure 2.51).

In this way, the diagram of the EPI is represented in Figures 2.52 and 2.53.



FIGURE 2.50
Bipolar symmetric gradient shape.

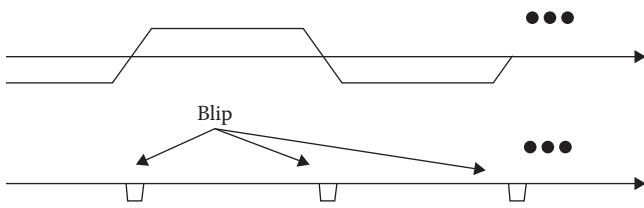


FIGURE 2.51
Continues and blip gradient shape.

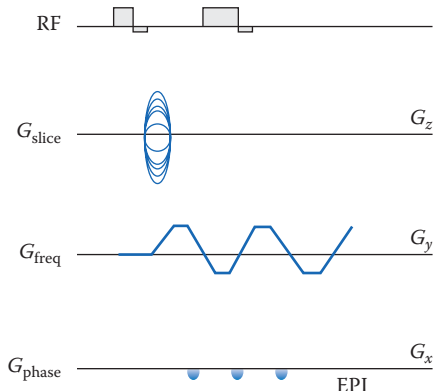


FIGURE 2.52
EPI diagram.

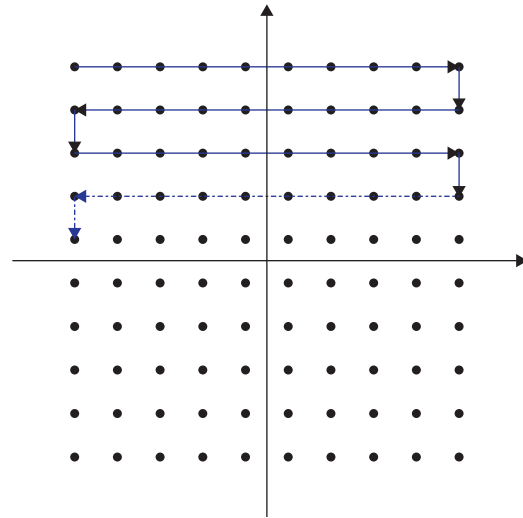


FIGURE 2.53
Oscillation of the gradients in the k -space covering.

The acquisition time of a single slice can be of the order of tens mS. In this way, it is possible to acquire a complete 3D volume of the brain within a single T_R . The EPI sequence can be realized with both SE and gradient-echo schemes. By observing the timing diagram for an EPI sequence in the SE format, we can do some consideration. There is a 90° slice selective RF pulse, which is applied in conjunction with a slice-selection gradient. There is an initial phase-encoding gradient pulse and an initial frequency-encoding gradient pulse to position the spins at the corner of k -space. Next, there is a 180° pulse. Since the echo-planar sequence is typically a single slice sequence, the 180° pulse need not be a slice selective pulse. The phase- and frequency-encoding directions are next cycled so as to traverse k -space. This is equivalent to putting 128 or 256 phase- and frequency-encoding gradients in the usual period when the echo is recorded. If we zoom into this region of the timing diagram, it will be clearer. You can see that there is a phase-encoding gradient, followed by a frequency-encoding gradient, during which time a signal is recorded. Next, there is another phase-encoding gradient followed by the reverse polarity frequency-encoding gradient during which time a signal is recorded. Looking at the k -space trajectory map at the same time as we are zoomed into the phase- and frequency-encoding gradient area, we can see how the gradients trace out k -space. The rate at which k -space is traversed is so rapid that it is possible, depending on the image matrix, to obtain 15–30 images per second.

2.6.2 Magnetic Resonance Angiography

MRA is a powerful technique used to visualize alterations inside blood vessels, with particular interest in the

arteries and veins; MRA is appreciated as alternative to the techniques like X-rays in computed tomography angiography and fluoroscopy. MRA to image blood vessels is less invasive compared to other techniques and no dose of ionizing radiation is released to the patients. MRA techniques can generate images of arteries and veins with the spatial resolution to reveal and evaluate the presence of stenosis, occlusions, aneurysms, and other abnormalities present in the lumen of the vessels.

Generally speaking, improvements in technology have produced a great amount of MRA techniques; they can be classified into two general families: *flow-dependent* methods and *flow-independent* methods. The most diffused techniques based on the *flow effects* in MRA are the phase-contrast MRA (PC-MRA) and the TOF-MRA.

MRA can be operated using techniques of contrast enhancement using pharmacological solutions with paramagnetic agents or using the effects of inherent contrast agents; the most frequently applied MRA exams involve the use of intravenous contrast agents, particularly those containing gadolinium to shorten the T_1 of blood to values usually shorter than the T_1 of all other tissues (see Table 2.1). Sequences weighed with a short T_R produce bright images of the blood. MRA is frequently used to evaluate the arteries of the neck and brain, the thoracic and abdominal aorta, the renal arteries, and the leg vascular system, and for this reason, it is an important application of the MRI.

2.6.3 Flow-Dependent Angiography

A class of methods for MRA is based on blood flowing in the vascular system. Those methods are referred to as *flow-dependent MRA*. They take advantage of the fact that the blood within vessels is flowing and it represents a paramagnetic agent moving along pathways of the vascular system; in this way, it is possible to distinguish these vessels from other static tissue and imaging of the vasculature can be produced. Flow-dependent MRA can be divided into different categories: there is phase-contrast MRA (PC-MRA) techniques, which utilizes phase differences to distinguish blood from static tissue, and TOF-MRA techniques; the spins that are moving for the blood circulation experience fewer excitation pulses than static tissue. Both these techniques do not use contrast agents and are suitable for investigation of the intracranial circulatory system alteration.

2.6.3.1 Phase-Contrast

The use of bipolar and symmetric gradient allows the creation of images of blood flow; in this way, it is possible to encode the velocity of moving blood with

the phase of the NMR signal. The application of a bipolar gradient occurs between the excitation pulse and the readout of the signal. Two symmetric lobes of equal area form a bipolar gradient. By definition, the total area of a bipolar symmetric gradient G is null. The bipolar gradient can be applied along any axis or combination of axes, depending on the direction along which flow is to be measured (e.g., x). The phase accumulated during the application of the gradient is 0 for stationary spins: this phase does not vary during the application of the bipolar gradient. On the contrary, for spins moving with a constant velocity v_x , along the direction of the applied bipolar gradient, the accumulated phase is proportional to both v_x and the first moment of the bipolar gradient; in this way, it is possible to provide an estimation of v_x . Note that to measure phase variation of interest, the MRI signal is manipulated by bipolar gradients (varying magnetic fields) that are preset to a maximum expected flow velocity. An image acquisition that is reverse of the bipolar gradient is then acquired and the difference of the two images is calculated. Static tissues such as muscle or bone will subtract out; however, moving tissues such as blood will acquire a different phase since it moves constantly through the gradient, thus also giving its speed of the flow. Because of the possibility to acquire only images of the blood flow in just one direction at a time with the phase-contrast technique, we need three separate image acquisitions in all directions to give a complete image of flow. This is a slow technique but it is still used because, in addition to imaging flowing blood, it is possible to perform quantitative measurements of blood flow that are useful for the diagnostic process.

2.6.3.2 Time-of-Flight

By using the gradient-echo technique, it is also possible to realize the imaging of vessels.

The source of diverse flow effects is the difference between the unsaturated and pre-saturated spins, and it is possible to create a bright image of the vessel without the invasive use of contrast media. The TOF technique uses a short echo time T_e and flow compensation to make the blood flowing in the vessels much brighter than stationary tissue. As the flowing blood enters the area being imaged, it has seen a limited NEX pulses so it is not saturated; this gives it a much higher signal than the saturated stationary tissue. Due to the fact that this method is strictly dependent by the flowing blood, areas with slow flow (such as large aneurysms) or blood flow in the plane of the image may not be well visualized. This technique is most commonly used in the head and neck districts, and it can give detailed and high-resolution images.

2.6.4 Contrast-Enhanced Angiography

Injection of MRI contrast agents is currently the most common method of performing MRA due to high resolution images of the vascular system that can be achieved. The contrast medium is injected into a vein, and images are acquired both in precontrast and during the first pass of the agent through the arteries. By subtracting these two acquisitions in the postprocessing stage, an image is obtained, which in principle only shows blood vessels, and not the surrounding tissue (digital subtraction angiography—DSA). Providing a correct timing of the pulses in the sequence may result in good-quality images. Timing is important due to the short “half-life” of the most used contrast agents. An alternative is to use contrast agents that do not leave the vascular system within a few minutes, but can remain in the circulation up to an hour (this kind of contrast agents are called *blood-pool agent*: the higher the molecular weight, the higher is the relaxivities of the media). With a longer time of contrast enhancement available for image acquisition, higher resolution imaging is achievable. Recent developments in MRA technology have made it possible to create high-quality contrast-enhanced MRA images without the digital subtraction of a noncontrast-enhanced mask image. This approach has been shown to improve diagnostic quality, because it prevents motion subtraction artifacts, as well as increases image background noise, both of which are direct results of the image subtraction. An important condition for this approach is to have excellent body fat suppression over large image areas, which is possible by using Dixon acquisition methods. Traditional MRA suppresses signals originating from body fat during the actual image acquisition, which is a method that is sensitive to the inhomogeneities of the magnetic fields, with the consequence of insufficient fat signal suppression. Dixon proposed a method to better distinguish and separate image signals created by fat or water; in this method, the difference in magnetic resonance frequencies between fat- and water-bound protons can be used for the separation of water and fat signals; these differences are related to the chemical shift effect. Difference in Larmor frequency generated by the shield on the B_0 by the two different molecular environments (fat and water) is important for the tissues discrimination (Figure 2.54).

The pioneering work of Dixon, published in 1984, presented this imaging technique based on the use of the phase differences to calculate water and fat components in the *post-processing* stage. Dixon’s method relies on the acquisition of the images in the condition with fat and water *in phase*, and then in *phase opposition*. These images are then added together to get *water-only* images, and subtracted to get *fat-only* images. Therefore, this

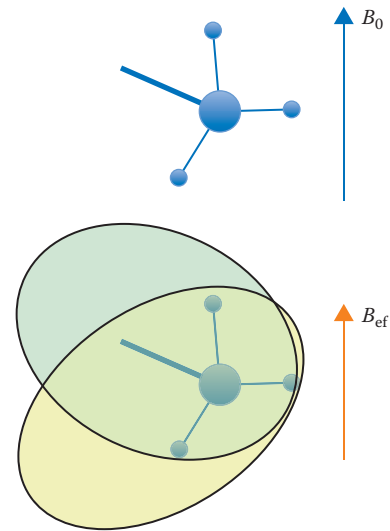


FIGURE 2.54

Chemical shift effects: schematic representation of the shielding action of the different fields induced by the molecule structure.

sequence type can deliver up to four contrast images in just one measurement: in phase, opposed phase, water, and fat images.

Originally, the technique proposed by Dixon was based on the so-called two-point sequence, with the acquisition of two images at different T_e ; however, Dixon-based fat suppression method can be very effective in regions of human body characterized by high magnetic susceptibility, where other techniques fail in the production of images without artifacts. Both the insensitivity to magnetic field inhomogeneity and the possibility of direct image-based water and fat quantification have currently generated high interest in the researches for improvements to the basic method. So, the combination of Dixon methods with gradient-echo sequences allows, for example, the liver imaging with four image types in one breath hold. But, both GE and SE sequences can be mixed with the Dixon mechanism. Using the combination of the Dixon methods with SE sequences, it is possible to achieve an excellent fat suppression with high-resolution imaging. Both SE and GE families have the fast version with the multi-echo acquisition at different phase-encoding gradient values. They have a different commercial identification as FSE and TSE. Fast SE (FSE) imaging and turbo SE (TSE) imaging are different commercial implementations of the RF refocusing echoes technique described in the pioneer work of Hennig et al. in 1986. Practically, the FSE–TSE pulse sequence insert, in a conventional SE sequence, a series of P180 refocusing pulse to generate a train of echoes; however, unlike the usual multi-echo sequence that collects all echoes in a train with the same phase encoding, in the FSE–TSE technique, the phase-encoding

gradient is changed at each echo of the train. In this way, by changing the phase-encoding gradient between each echo, it is possible to acquire several k -space lines in a single repetition time T_R .

With this technique and using the *water-only images*, the body fat can be neglected with high efficiency, so there is no need of images for subtraction in the post-processing, and it is possible to achieve high-quality MR image for angiography. These are just some examples of possible applications: technology makes available a great amount of solutions for the imaging problem.

2.7 Conclusion

The *sequence* theme in MRI is continuously in evolution due to the technological improvement of the electronic technology of the *gradients* and *radiofrequency* pulses. Being faster and more powerful, gradients are able to explore innovative solutions for the proper k -space *measuring* for the MRI of multiparametric contrast, and RF is becoming highly selective and fast, to manipulate as better as possible all the magnetization states. All the companies are investing in R&D in this field. In this way, with the collaboration of expert physicians it is possible to test and realize new diagnostic sequences with the capability to get a greater amount of information with a shorter time of exam reducing the exam stress for the patients. Angiography and brain functional MRI are only two of the possible examples of the successful application of MRI technology. The functional connectivity in MRI leads to important understanding of network activity for the brain functions, and this kind of measurement derives from a stable and fast technology to follow the oscillations in the MRI signal. The discussions in this chapter can only be an introduction to the methods of sequence description and design. This chapter was realized with the idea to give the basic knowledge for interpretation of a sequence and to operate in the scanner control to optimize the improvements effects on the image. It is not exhaustive of the argument, but it is only to give a basic knowledge. There is a great amount of

materials published for a deep discussion of the topics; some important papers and books on the arguments are reported in the bibliography at the end of this chapter. I hope I was able to give you the importance of the appropriate formalism to use based on the complex functions: Mathematics is important for better exploitation of the innovation in MRI and the reader can find many books and also a number of web sites of help for this exploration. This is only the first step.

Bibliography

- Brown T.R., Kincaid B.M., Ugurbil K., NMR chemical shift imaging in three dimension, *Proc. Natl. Acad. Sci. USA* 79, 3523–3526 (1982).
- Carr James C., Carroll Timothy J., Editors, *Magnetic Resonance Angiography: Principles and Applications*, Springer, New York (2011).
- Hennig J., Nauerth A., Friedburg H., RARE imaging: A fast imaging method for clinical MR, *Magn. Reson. Med.* 3, 823–833 (1986).
- Holodny Andrei I., *Clinical fMRI and Diffusion Tomography: Paradigm Selection, Neurological Assessment, and Case-Based Analysis*, Springer, New York (January 2015).
- Ljunggren S., A simple graphical representation of Fourier-based imaging methods, *J. Magn. Reson.* 54, 338–343 (1983).
- Poldrack R.A., Mumford J.A., Nichols T.E., *Handbook of Functional MRI Data Analysis*, Cambridge University Press, New York (2011).
- Prof. StamSykora web page, *K-space formulation of MRI*, <http://www.ebyte.it/library/educards/mri/K-SpaceMRI.html>.
- Twieg D.B., The k -trajectory formulation of the NMR imaging process with applications in analysis and synthesis of imaging methods, *Med. Phys.* 10, 610–621 (1983); Building on earlier work in the field of optics, *Proc. Soc. Photo-Opt. Instrum. Eng.* 347, 354 (1982).
- Wang Y., *Principles of Magnetic Resonance Imaging*. CreateSpace Independent Publishing, USA.
- Weadock W., Chenevert T., Emerging concepts in MR angiography, *Magn. Reson. Imaging Clin. N. Am.* 17, doi: 10.1016/j.mric.2009.02.005 (Saunders 2009).

This page intentionally left blank

3

Contrast Agents for Magnetic Resonance Imaging

Henrik S. Thomsen

CONTENTS

3.1	Contrast Media.....	61
3.2	Gadolinium-Based Contrast Media	62
3.2.1	Chemistry	62
3.2.2	Stability.....	63
3.2.3	Transmetallation	65
3.2.4	Osmolality.....	66
3.2.5	Viscosity	66
3.2.6	Pharmacokinetics.....	66
3.2.6.1	Extracellular Agents	66
3.2.6.2	Organ-Specific Agents (Protein Binders).....	67
3.3	Adverse Reactions.....	67
3.3.1	Acute Nonrenal Adverse Reactions	67
3.3.2	Acute Renal Adverse Reactions	69
3.3.3	Late Adverse Reactions.....	69
3.3.4	Very Late Adverse Reactions.....	70
3.4	Miscellaneous.....	70
3.4.1	Contrast Media Extravasation.....	70
3.4.2	Interaction	70
3.4.3	Pregnancy and Lactation.....	71
3.5	Contrast Media Administration	71
3.5.1	Routes of Administration	71
3.5.2	Dose	71
3.6	Other Contrast Media	71
3.6.1	Manganese-Based Contrast Media	71
3.6.2	Iron-Based Contrast Media	71
3.6.3	Water.....	72
	References.....	72

FOCUS POINT

Generally, gadolinium-based contrast media for magnetic resonance imaging (MRI) are safe in the amount approved by the medicines agencies. However, significant adverse reactions may occur. Particularly, identifying patients at risk prior to administration of contrast agent can lead to a risk reduction. In case of a significant adverse reaction to a patient, it is very important to be ready for a possible instant treatment. In many countries, neither manganese-based nor iron-based contrast media are commercially accessible for the time being.

3.1 Contrast Media

All commercially accessible MRI contrast media at present are based on the atom gadolinium. Gadolinium is

1. Part of the lanthanide group in the periodic table.
2. The atom that provides the highest relaxivity per atom.
3. Toxic for the body even in small doses.

Before using gadolinium diagnostically in human beings, the atom has to be detoxified, which is done by

binding it to a chelate (De Häen 2001). Administration of contrast media is used in one-third of the MRI examinations because unenhanced MRI is providing additional information regarding the soft tissue compared to computed tomography (CT), even if this examination is performed with iodine-based contrast media. MRI most often is used in relation to brain imaging and chest imaging, including breast and abdomen (e.g., liver, bowel, kidney, and prostate). In the past, contrast media were mandatory to perform MR angiography, but this is no longer the case.

Iron-based and manganese-based contrast agents have also been available previously. However, these are no longer obtainable with the exception of a few countries (perhaps none at the time of printing). All the contrast agents were organ-specific: hepatocytes, macrophages, bowel lumen, and lymph nodes.

3.2 Gadolinium-Based Contrast Media

MRI contrast agents are diagnostic pharmaceutical compounds. They primarily contain *paramagnetic ions* (e.g., gadolinium and manganese) affecting the MR signal properties of the surrounding tissue. Paramagnetic agents are positive enhancers that reduce the T_1 and T_2 relaxation times and increase tissue signal intensity on T_1 -weighed MR images and have just about no effect on T_2 -weighed images. *Superparamagnetic ions* (e.g., iron-based agents) have a signal-enhancing effect

on T_1 -weighed images at low concentrations; however, they have a negative effect on the tissue signal in higher concentrations, which is seen on the T_2/T_2^* -weighed images. Conversely, it has nearly no effect on T_1 -weighed images (Thomsen et al. 2016).

In the 1980s, copper (Cu^{2+}), manganese (Mn^{2+}), and gadolinium (Gd^{3+}) were contemplated for use as paramagnetic ions for MRI (De Häen 2001). However, gadolinium (atomic number 64 and atomic weight of 157) proved to be the most powerful and unfortunately also the most toxic of the ions with its seven unpaired electrons. Today, gadolinium is the active constituent in all commercially available MR contrast media due to its high magnetic moment and a relatively slow electronic relaxation time (Table 3.1).

3.2.1 Chemistry

Gadolinium administration cannot be undertaken as a simple inorganic solution, such as chlorides and sulfates, since the simple salts of gadolinium hydrolyze instantaneously, forming insoluble oxides and hydroxides at pH 7, which are retained in macrophage organs such as liver and bone for a very long period of time (Thomsen et al. 2016). In regard to mice, their LD_{50} values for injected raw gadolinium ions are approximately 0.1 to 0.3 mmol/kg, similar to the standard human dose of a current gadolinium-based contrast media. If gadolinium is to be used in a contrast medium, it requires that is bound firmly and stably to a carrier molecule, which can solubilize it and furthermore prevent hydrolysis. Yet, it must still allow for catalysis of water proton

TABLE 3.1

Gadolinium-Based Agents: Brand Names and Characteristics

Name	Brand Name	Organ Specific	Extra-Cellular	Chelate	Ionicity	Hepatobiliary Excretion	Protein-Binding	Risk of NSF ^a
Gadodiamide	Omniscan	No	Yes	Linear	Nonionic	No	No	High
Gadoversetamide	Optimark	No	Yes	Linear	Nonionic	No	No	High
Gadopentetate dimeglumine	Magnevist	No	Yes	Linear	Ionic	No	No	High
Gadobenate dimeglumine	Multihance	Yes (Liver)	Mainly	Linear	Ionic	Yes (1%–4%)	Yes (4%)	Intermediate
Gadoxetate disodium	Primovist, Eovist	Yes (Liver)	No	Linear	Ionic	Yes (42%–51%)	Yes (10%)	Intermediate
Gadofosveset trisodium	Vasovist, Ablavar	Yes (Blood)	No	Linear	Ionic	Yes (5%)	Yes (90%)	Intermediate
Gadobutrol	Gadovist, Gadavist	No	Yes	Macrocyclic	Nonionic	No	No	Low
Gadoteridol	Prohance	No	Yes	Macrocyclic	Nonionic	No	No	Low
Gadoterate meglumine	Dotarem, Magnescope	No	Yes	Macrocyclic	Ionic	No	No	Low

^a According to the classification provided by the European Medicines Agency.

relaxation and excrete rapidly, thus carrying the heavy metal ion out of the body.

Since the 1950s, certain polycarboxylic acids (e.g., diethylene tetraaminepenta-acetate [DTPA]) have been recognized as a great coordinator of metal ions (Dawson et al. 1999). Gadolinium(III) is a 3+ charged ion with nominally nine sites at which another chemical can bind it. When using the DTPA ligand, eight out of the nine sites are occupied by three N and five O⁻ in the carboxyl groups. The additional ninth gadolinium site is used for a fast exchange of water molecules between the *inner sphere* (bonded directly to gadolinium) and the bulk (nonbonded) water (Morcos 2007). This feature is a necessity in regard to strong water proton relaxation. With the exception of protein binders, all the commercial gadolinium chelates achieve a similar effect on the proton relaxation and visibility in MRIs (Figures 3.1 and 3.2).

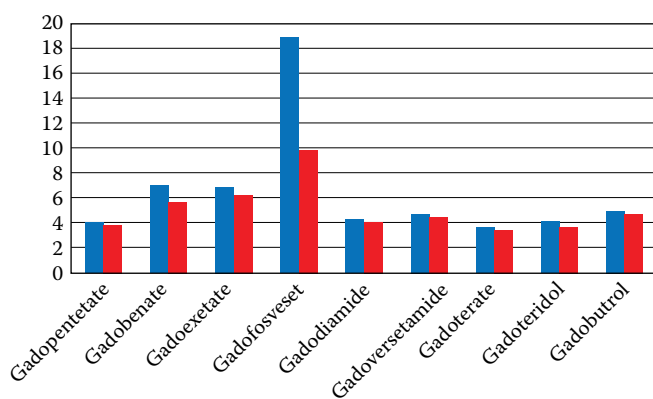


FIGURE 3.1

r_1 -Relaxivity in plasma of the nine commercially available gadolinium-based contrast media at 1.5 (blue) and 3.0 (red) T (mM⁻¹s⁻¹).

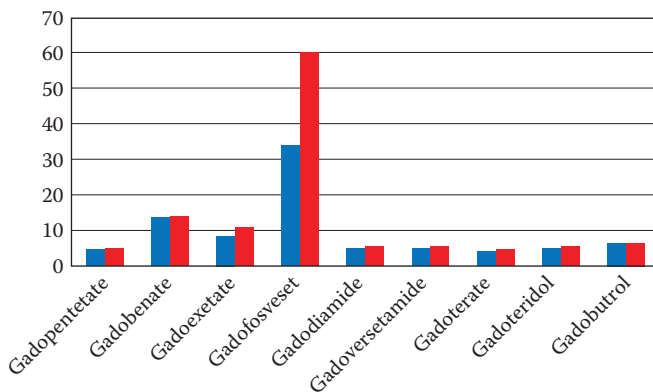


FIGURE 3.2

r_2 -Relaxivity in plasma of the nine commercially available gadolinium-based contrast media at 1.5 (blue) and 3.0 (red) T (mM⁻¹s⁻¹).

In regard to gadolinium-based contrast media, the choice of ligand structure influences the chemical and biological stability of the compound as well as the colligative properties of its formulations (Thomsen et al. 1999, 2016). These in turn then influence tolerance, pharmacokinetics, clinical uses, and contraindications. Two fundamental structural types are used (Figures 3.3 and 3.4):

1. Linear seven-ring structures derived from DTPA
2. Macrocyclic eight-ring structures derived from dodecane tetra-acetic acid (DOTA)

The fundamental difference in these structures is that the chain of nitrogen and carbon atoms that constitute the backbone of the chelating agent is open on both ends in linear agents and closed into a single loop in macrocycles.

3.2.2 Stability

There are significant differences in the liability to release free gadolinium ions between the various agents (Morcos 2014b). The instability of gadolinium-based contrast agents is an important factor in the pathogenesis of the serious complication of nephrogenic systemic fibrosis (NSF). Coordination sites of gadolinium represent the number of atoms or ligands directly bonded to the metal center such as Gd³⁺. The bonding between the metal center (Gd³⁺) and the ligands is through valent bonds in which shared electron pairs are donated to the metal ion by the ligand. In an ionic linear molecule such as Gd-DTPA, Gd³⁺ is coordinated with five carboxyl groups and three amino nitrogen atoms. The three negatively charged carboxyl groups neutralize the three positive charges of the Gd ion, and the remaining two carboxyl groups are neutralized by two meglumine cations. In a nonionic linear molecule such as gadodiamide or gadoversetamide, the number of carboxyl groups is reduced to three because each of the other two carboxyl groups has been replaced by a nonionic methyl amide. Although both amide carbonyl atoms are directly coordinated to Gd³⁺, the binding is weaker compared to that with carboxyl groups. This weakens the grip of the nonionic chelate on the Gd³⁺ and decreases the stability of the complex.

The other feature influencing the binding between the Gd³⁺ and the chelate is whether the configuration of the molecule is cyclic or linear. The macrocyclic molecule offers better protection and binding of Gd³⁺ because it is a preorganized rigid ring of almost optimal size to cage the Gd ion. In contrast, the linear structure, which is a flexible open chain, provides weaker protection of the gadolinium ion.